INS, GPS, and Photogrammetry Integration for Vector Gravimetry Estimation

by

Fathi Y. Dwaik
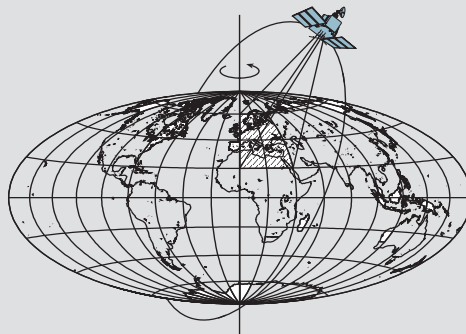
INS, GPS, AND PHOTOGRAMMETRY INTEGRATION
FOR VECTOR GRAVIMETRY ESTIMATION

DISSERTATION

Presented in Partial Fulfillment of the Requirement for
the Degree Doctor of Philosophy in the Graduate
School of The Ohio State University

BY

Fathi Y. Dwaik, M.S.

*****

The Ohio State University
1998

ABSTRACT

Vector gravimetry using Inertial Navigation System (INS) in semi-kinematic mode has been successfully applied. The integration of INS with other sensors, Global Positioning System (GPS) or Gradiometer, for instance, has been under investigation for many years. This dissertation examines the effect of photogrammetric derived orientation on the INS sensor's calibration and estimation of the gravity vector. The capability of such integration in estimating the INS biases and drifts is studied. The underlying principle, mathematical models, and error sources are presented and analyzed. The estimation process utilizes the measurements of the Litton LN-100 inertial system, Trimble 4000 SSI GPS dual frequency receiver, and metric frame camera. An optimal filtering technique is used to integrate both GPS and INS on the level of raw measurement for both systems. Introducing accurate and independent orientation parameters, e.g., the photogrammetric source in this study, is demonstrated to enable calibration of inertial gyros and bounding of their drift errors. This leads to improvement in the horizontal components of the gravity vector estimation. The estimability and improvement of the deflection of the vertical components are tested using flight test data over Oakland, California, and a set of photogrammetric images simulated along the flight trajectory.

The error statistics of the orientation measurement are modeled on the basis of the variance-covariance matrix of a photogrammetric bundle adjustment of all photos. With just a few ground control points at the beginning of the trajectory, the orientation measurement errors along the trajectory are correlated significantly from epoch to epoch, thus reducing the information content of the external orientation estimates.

The horizontal gravity component estimation is tested with respect to its sensitivity to the variance of the orientation measurement errors, to its auto-correlation in time, to the cross-correlation between angles, and to the amount of available ground control. Although photogrammetric measurements, if uncorrelated, control orientation errors as well as better than achievable with aircraft maneuvers, the inherent correlation with a very limited amount of ground control provides only a small improvement. On the basis of the simulation parameters, the gravity estimation error was reduced from 20 mgal (GPS/INS only) to about 9 mgal (best uncorrelated control) versus 17 mgal (correlated control).

ACKNOWLEDGMENTS

TABLE OF CONTENTS

CHAPTER 1

INTRODUCTION

1.1 Background

The invention of the Global Positioning System (GPS) had a direct impact on many scientific, military, industrial, commercial, and recreational applications. The countless applications and substantial performance of GPS, inertial systems, and their integration with other sensors are far beyond the intention of the original designers of either system. The Inertial Navigation System (INS) utilizes the inertial properties of its sensors to solve for the position, velocity, and orientation of the vehicle. Three orthogonal gyroscopes maintain spatial orientation of the system, and three orthogonal accelerometers measure specific forces being the difference between kinematic and gravitational accelerations. Therefore, gravitational information is necessary to obtain navigation. The time integration of acceleration yields velocity, and the second time integration yields position. Besides the high data rate, the INS navigation parameters are very precise in the short term. However, INS sensors (accelerometers and gyroscopes) are characterized with systematic error growth in the long term, primarily due to the drift error of the gyros. The GPS, on the other hand, is characterized by its consistent and accurate navigation, over long periods of time. The integration of INS and GPS has the advantage of uniform accuracy of GPS and short-term stability of INS. This integration has been under investigation for many years, e.g., Wong and Schwarz (1983), Vallot et al. (1991), Sohne et al. (1994), and Liu et al. (1997).

For attitude estimation, again, the basic limitation of the high-precision inertial system is the drift rate that grows without bounds. The drift, depending on the system, ranges between 10°-0.001°/hr. The orientation parameters extracted from a multiple GPS antenna system could be used as an external aid to the INS, e.g., Cramer and Schade (1995). As the GPS orientation parameters, however, are less accurate (3-5 arc-minutes rms as reported by El-Mowafy and Schwarz (1994) using multiple GPS antenna mounted on a van, and about 5 arc-minutes rms with using wing flexure model as reported by Sun (1994), this synergism technique can be applied to increase the reliability of the orientation parameters and where some accuracy can be sacrificed. On the other hand, the photogrammetric bundle adjustment solution to the exterior orientation parameters is a standard successful and accurate process that takes advantage of ground control and the geometrical strength of overlapping images.

The importance of gravity on navigational accuracy was appreciated many years ago. With the great advancement of INS manufacturing, it has always been realized that the unknown gravitational acceleration is one of the limiting factors for achieving accurate positions. An external navigational and/or gravitational source of information with sufficient accuracy could be used to calibrate part of the INS biases and drifts, which in return, leads to more accurate positions. It is important to notice that it could be necessary to calibrate the INS sensors for imperfections and/or the different environments they operate in. Integrating GPS and INS for navigation applications solves key problems of each of the navigation systems; to mention a few, it helps to detect and

fix GPS cycle slips; in addition, a higher rate of INS data acquisition helps in filling the gaps between GPS data epochs; furthermore, the limited access of GPS signals in cities, forests, and mountains may be supplemented with INS; and finally, GPS can be used to bound the unavoidable drift of the INS sensors. As the hardware of both sensors was not designed primarily for integration, many of the integrated system resulted in partial exploitation of the synergistic potential of both GPS and INS.

Although most of the work done in integrating GPS and INS was for obtaining accurate positions, this research examines the effect of accurate photogrammetric orientation in separating INS errors and estimating the gravity *vector*. It is also noticeable that a major part of the existing research on moving-base gravity determination concerns scalar gravimetry by using onboard gravimeter (Brozena and Peters, 1994; Wei and Schwarz, 1998) or accelerometers of an inertial system. Scalar gravimetry is used to describe the dominant vertical component of gravity anomaly vector. Here, the estimation of the total *vector* of gravity is considered with primary emphasis on the horizontal components.

The gravity disturbance vector, δg, is the difference between gravity vector at point P on the Earth surface and the normal gravity vector at the same point. The difference in direction between the two vectors is approximately the deflection of the vertical (DOV). The DOV has two components: north-south (N-S) component (ξ), and east-west (E-W) component (η). The deflection components can be obtained by comparing the astronomic coordinates (Φ, Λ) and geodetic coordinates (φ, λ) as shown in equations (1.1). As such, this method is called astrogeodetic determination. Detailed definitions of astronomic and geodetic coordinates and more on their relationships can be found in Heiskanen and Moritz (1967).

$$
\begin{aligned}
\xi &= \Phi - \varphi \\
\eta &= (\Lambda - \lambda)\cos\varphi
\end{aligned}
\tag{1.1}
$$

The gravimetric determination of the deflections, on the other hand, is shown in equations (1.2) using spherical approximation. These equations are called the formulas of Vening Meinesz, and as one clearly sees, they require global coverage of gravity data (at least in theory).

$$
\xi = \frac{1}{4\pi G}\iint_\sigma \Delta g \frac{dS}{d\psi}\cos\alpha \, d\sigma
$$

$$
\tag{1.2}
$$

$$
\eta = \frac{1}{4\pi G}\iint_\sigma \Delta g \frac{dS}{d\psi}\sin\alpha \, d\sigma
$$

Δg is the gravity anomaly, being the difference between actual gravity and normal gravity, respectively, at geoidal point P and ellipsoidal point Q, where Q is obtained by projecting P onto the ellipsoid by means of the ellipsoidal normal (Moritz, 1980). *G* is an

average value of gravity; α is the azimuth between the computation and integration points; and $S(\psi)$ is Stokes' function. More details can also be found in Heiskanen and Moritz (1967).

It is considered by the scientific and industrial communities that airborne gravimetry is the most efficient tool to map the regional gravity field in inaccessible areas around the globe. Satellite gravimetry was also considered by the scientific community to determine the long wavelength signal of the gravity field. Prior to GPS, the inability to determine the kinematic accelerations in airborne missions made airborne gravimetry impractical. With the complete GPS constellation and the advancement and capability of kinematic GPS/INS technology, airborne gravimetry missions are proving to be very promising.

1.2 Problem of GPS/INS Vector Gravimetry

Recovering the gravity parameters from inertial systems with position updates goes back to the early 1970's when Rose and Nash (1972) showed the ability of the system to measure directly the deflection of the verticals. The deflection of the vertical, as mentioned earlier, refers to the deviation between the direction of the gravity vector, or plumb line, and the ellipsoidal normal (Moritz, 1980). The availability of more accurate inertial systems, high precision GPS positioning updates, and superior software and estimation performance have all enriched and revitalized the field of GPS/INS airborne gravimetry.

The so-called ZUPT (Zero Velocity Updates) scheme was used with success in recovering the gravity parameters (Huddle, 1988). However, this technique had an obvious drawback for airborne gravimetry. Based on simulations, Wei and Schwarz (1994) showed that very low noise characteristics INS (0.0001 $^{\circ}$/hr gyro drift, 1 mgal (10^{-5} m/s^2) for accelerometer bias uncertainty, and 1 ppm for the accelerometer scale factor), could yield 0.5 arc-seconds estimated error in the deflections of the vertical and 0.5 mgal in the gravity anomaly, provided an averaging period of GPS-derived accelerations between 1 to 2 minutes.

Accurate gravity related parameters (e.g., geoid, gravity anomaly, and deflections) at pre-defined locations were also used in what is called gravitational update (see Eissfeller, 1989). Based on simulation, this study reported 0.2-0.4 arc-seconds estimated error in the deflections of the vertical.

To achieve a few arc-seconds' accuracy in inertial platform stabilization, to better estimate gravity parameters, Zhang et al. (1995) investigated whether GPS velocity updates are capable of achieving this level of accuracy. Five arc-seconds were reported under the conditions of Selective Availability (SA) elimination and accelerometer biases not exceeding 20 mgal.

A thorough investigation and research in the field of airborne gravimetry concluded that gyro errors are of paramount importance and can only be bounded by external attitude updates, e.g., Jekeli (1994), Huddle (1978), and Mangold (1995). Based

on simulation analysis of GPS/INS airborne vector gravimetry, Wei and Schwarz (1994) reached the conclusion that GPS positioning updates to the INS measurements reduce the effect of attitude errors caused by initial misalignment and gyro drift uncertainties. However, isolating gravity signal (i.e., deflection of the vertical) from initial misalignment and gyro drift errors cannot be solved effectively. Stellar observations improve the accuracy of inertial navigation systems and help in recovering the deflections of the vertical. Accurate estimates of the deflections using stellar INS at different altitudes help in gravity data collection and research, especially over oceans and polar areas (Northrop Corporation, 1985). These instruments can precisely point at pre-selected stars using telescopes. Star trackers are expensive instruments, however, and used mainly for long-range missiles and reconnaissance planes. Attitude update could also be achieved from multiple GPS antennas. As mentioned in the previous section, the accuracy of the GPS derived attitude parameters is not sufficient to control the INS drift error.

Prior to the use of INS for gravity estimation, a modified gravimeter, LaCoste and Romderg or Bell gravimeters, were used for airborne gravimetry. As reported by Wei and Schwarz (1996), the insufficient platform stabilization is the major problem for a further improvement of these gravimeters. As quality types of INS have been released from military, and as the cost effectiveness of airborne gravity data acquisition system has been realized, a specially designed INS for gravity missions that stabilizes an independent high-precision vertical accelerometer was used in recent years; see Salychev (1995). The questions, however, remain: what are the most efficient and accurate techniques and models to be used and what type of external source of information can be introduced to extract the weak gravity signal, from a relatively large system noise?

In an attempt to make use of the accurate aircraft acceleration derived from GPS carrier phase measurements, Hammada (1996) searched the extraction of the gravity signal by differencing the time series of GPS derived acceleration and the time series inertial acceleration. Different filtering techniques have been investigated to estimate the vector of gravity disturbance δg; one natural choice was to apply a low-pass filter to reduce the measurement noise. As the system errors also contain noise in the low-frequency band, the δg signal cannot be completely separated, and consequently, a high resolution of δg cannot be achieved. Unlike frequency domain filtering, the state space domain Kalman filtering techniques are based on statistical assumptions for both δg and system errors, see Knickmeyer (1990), Gleason (1992), Jekeli (1994), and Eissfeller (1996). The success of this technique largely depends on the closeness of these statistical models to the unknown real models. A more deterministic approach, called wave estimation, was also applied to estimate δg, Salychev (1995). This technique uses deterministic models for δg in between time intervals, called estimation cycles. The validity of this piece-wise modeling and the selection of the estimation cycle are crucial for this technique to work properly (Wang, 1998).

From the preceding discussion, one can conclude that gyro drift is one of the most critical hindrances in GPS/INS airborne vector gravimetry, especially the long

wavelength part of the deflection components. A one arcsecond error in the system's platform level (i.e., gyro error) produces about 5 mgal error in the horizontal gravitation estimation. More on numerical estimates based on INS derived error equations are provided towards the end of Chapter 3.5. Therefore, the orientation accuracy is essential for accurate estimation of the horizontal components of the gravity vector. Mounting a camera along GPS/INS for mapping could also provide independent orientation parameters to correct the INS alignment error and therefore, extract gravity information along the flight trajectory. In contrast to the use of these sensors for positioning and mapping applications, the photogrammetric orientation parameters can be used to bound the gyro error that grows with time. The bundle block adjustment uses conjugate point measurements along a sequence of images to solve for the attitude angles in accordance with the best reconstruction of the light rays between image space and object space at the time of exposures.

1.3 Dissertation Outline

The overall objective of this research is to analyze the underlying principles of post-processing INS, GPS, and photogrammetry integration for vector gravimetry estimation. The photogrammetric information is used as an external aid to the INS to control and estimate orientation drifts and biases. The horizontal gravity component estimation is studied with respect to its sensitivity to the correlation of the orientation measurement errors and to the amount of available ground control points. The estimability and improvement of the deflection of the vertical components are tested using a flight test over Oakland, California and a set of photogrammetric images simulated along the flight trajectory. Factors affecting system accuracy will be investigated and system noise will be stochastically modeled.

Chapter 2 serves as introduction to the systems being integrated in this research. The observation types of each system, error sources, and potential accuracy are discussed. The fundamental principle behind each system is briefly discussed. For inertial navigation system, navigation equations, mechanization, and initialization process are also elaborated upon to grasp better understanding of the system and to ensure completeness of this study. The mathematical model and estimation process of photogrammetric exterior orientation parameters using bundle block adjustment is outlined. From the strip of simulated images, correlation analysis and achievable accuracies of the orientation parameters are established. In Chapter 3, the underlying principle of inertial gravity determination is presented. The INS error model is also derived with the emphasis on the estimability of its parameters. Both GPS and photogrammetry sources of updates and their respected accuracy are also presented. Furthermore, photogrammetric contribution to gravity vector determination is outlined. Toward the end of Chapter 3, model selection for kinematic vector gravity estimation is discussed. In Chapter 4, the stochastic error models used in this study are presented with emphasis on the importance of proper modeling for optimality of estimation. The underlying principle of integrating both data streams of GPS and INS is also discussed. Photogrammetric integration with GPS/INS is outlined for both integration schemes, namely, loose and tight integration. The loose integration scheme is the one selected for further investigation in this study. The results and analyses of airborne GPS/INS and

GPS/INS/Photogrammetry integration for vector gravimetry are presented in Chapter 5. The capability of such integration in estimating, in particular, the orientation parameters and the horizontal components of gravity vector is illustrated. This is done with numerical tests using a combination of actual and simulated data. Chapter 6 summarizes the conclusions and recommends future investigations.

CHAPTER 2

NAVIGATION SYSTEMS

2.1 Global Positioning System
2.1.1 Overview

The NAVSTAR Global Positioning System (GPS) is an all-weather, space-based navigation system controlled and operated by the United States Department of Defense (DoD) to satisfy military forces' requirements of accurate positioning, navigation, and time transfer using a common reference system, anywhere on or near the Earth on a continuous basis (Hofmann-Wellenhof et al, 1992). A secondary GPS goal was to provide an unencrypted signal of degraded accuracy to civilian users. As the system developed, civil usage expanded rapidly, and the number of civilian users now greatly exceeds the number of military users. The timing, velocity, and positioning information provided by GPS is being used for a growing number of new, innovative applications that could not have been foreseen by the original system designers (NRC, 1995).

The GPS has been used for surveying and geodetic applications as well as many other civilian use of the GPS system. Some potential applications of GPS are: accurate routes and safe landings for commercial airlines, collision avoidance for trains, emergency deployments, photogrammetric triangulation, highly accurate geodetic surveys and sea level determination, occultation of atmosphere, and numerous Geographical Information System (GIS) applications.

The heart of GPS is using highly accurate atomic clocks to generate a stable frequency of 10.23 MHz. The hydrogen maser has been chosen by the last set of GPS satellites, as it offers a significant improvement over cesium and rubidium clocks. The hydrogen maser clock has a stability of 10^{-14}-10^{-15} over one day. The DoD has the capability of degrading the satellite signal through Selective Availability (SA) and Anti Spoofing (AS). SA intentionally introduces variations in the time of the satellite clocks or provides incorrect orbital parameters. AS, on the other hand, encrypts the Precision (P) code to generate the Y code instead.

The navigation signal transmitted from GPS satellites consists of two frequencies: L1 = 1575.42 MHz, and L2 = 1227.6 MHz. L1 signal is modulated with both the P and the Course Acquisition (C/A) codes. The L2 signal, on the other hand, is modulated with P code only. Both L1 and L2 are modulated with the navigation message. Following Milliken and Zoller (1980), the functions of the codes are twofold: First, identification of the space vehicle, as code patterns are unique to each GPS satellite, and are matched with like codes generated in the user receiver. Second, the measurement of the navigation signal transit time by aligning the received code to match the receiver's generated code. The C/A code has a chip rate of 1.023 MHz and repeats itself every millisecond. The P code, on the other hand, has chip rate of 10.23 MHz and repeats itself once every 267 days, but resets every seven days.

GPS receivers consist of two main segments: signal reception and signal processing. Single frequency receivers process only L1 signal, while dual frequency receivers process both L1 and L2 signals. The receiver's oscillator is the most important part, discriminating among the satellite signals and generating replica of these signals. It is relatively easy to lock onto the C/A code and generate its replica since it repeats itself every millisecond. In the case of P code, which has a complete cycle of 267 days, it would take a long time to search and generate a replica of the code. The Hand Over Word (HOW), as part of the navigation message, makes the time within the seven days available for the receiver to generate replica of the P code. One significant feature of the GPS receiver is the number of satellites that can be tracked simultaneously.

Two different techniques are used to perform the GPS observation processes inside the receiver: *The code correlation technique* uses the signal replica generated by the receiver's oscillator to correlate it with the satellite signal. The time shift Δt for optimal correlation between the two signals corresponds to the travel time of the signal from the satellite to the receiver. *The codeless technique* squares the incoming signal to remove modulations. This technique is independent from the code, and therefore, the navigation message is not available. In addition, the noise will be squared. The GPS carrier phase measurement process uses demodulated satellite signal. The observable (carrier beat phase, or carrier phase for short) is generated by aligning the satellite carrier phase with the reference phase signal generated by the receiver's oscillator.

2.1.2 GPS Positioning Principle

System operation requires that at least four satellites be visible and in good geometry. The transmitted message contains ephemeris parameters that enable the user to calculate the position of each satellite at the transmission time of the signal. If the GPS receiver clock is set precisely to GPS time, then measuring the distance to three GPS satellites simultaneously would determine the three-dimensional position of the receiver by simple resection process. The GPS receiver, however, uses an inexpensive clock, which has an offset from the GPS time. This problem is overcome by observing an additional satellite range to solve or to eliminate the receiver clock bias.

2.1.3 GPS Coordinate Systems

Coordinate systems are usually difficult to define correctly and accurately. The complex details of coordinate system definition and realization are beyond the scope of this study. The reader is referred to "*Earth Rotation: Theory and Observation,*" by Moritz and Mueller (1987) for more information. Two kinds of coordinate systems are in use: Celestial (space fixed) to describe satellite motion and Terrestrial (Earth fixed) to obtain position on the ground. The variations of the earth's rotation parameters: precession, nutation, and polar motion must be considered for the transition between both systems.

GPS uses an Earth fixed global reference frame called World Geodetic System WGS-84 as a reference. Associated with WGS-84 is a geocentric equipotential ellipsoid of revolution, defined by four parameters as shown in Table 2.1 below. The parameters of the WGS-84 ellipsoid are identical to those for the Geodetic Reference System 1980

(GRS-80) ellipsoid with one minor exception. The coefficient form used for the second degree zonal is that of the WGS-84 Earth Gravitational Model rather than the notation used with GRS-80, (DMA, 1987). From the four defining parameters, other parameters like flattening and equatorial gravity, for instance, can be unambiguously derived.

Parameter	Description
a = 6378137 m	Semi-major axis of the ellipsoid
GM = 3986005.10^8 $m^3.s^{-2}$	Earth's gravitational constant
ω_e = 7292115.10^{-11} $rad.s^{-1}$	Earth's Angular velocity
$C_{2,0}$ = $-484.16685 \times 10^{-6}$	Normalized Zonal coefficient of second degree

Table 2.1: Four parameters defining the Geodetic Reference System 1984 (GRS-84) ellipsoid

The third axis of the coordinate system coincides with the mean axis of Earth's rotation. The first axis is associated with the mean Greenwich meridian at the equator. The second axis completes the right-handed coordinate system. The geodetic coordinates can be transformed to Earth Centered Earth Fixed (ECEF) Cartesian coordinate system as follows:

$$\begin{bmatrix} x \\ y \\ z \end{bmatrix}_{ECEF} = \begin{bmatrix} (N+h)\cos\varphi\cos\lambda \\ (N+h)\cos\varphi\sin\lambda \\ [N(1-e^2)+h]\sin\varphi \end{bmatrix} \tag{2.1}$$

where: φ, λ, and h are the geodetic latitude, longitude, and height. N is the radius of curvature in the prime vertical, and e is the ellipsoidal eccentricity.

2.1.4 GPS Observables

There are three fundamental GPS observations: *The code pseudorange* is the distance between the satellite and the receiver as measured by the transit time, scaled by the speed of light. The pseudorange observable differs from the true geometric distance since both clocks of the satellite and the receiver are not synchronized. The general equation for the pseudorange between satellite (k) and receiver (i) is written as:

$$R_i^k = \rho_i^k + d_{i\ (ion)}^k + d_{i\ (trop)}^k + d_{i\ (m)}^k + c\Delta_R + \varepsilon_i^k \tag{2.2}$$

where:

R_i^k : Pseudorange corrected for satellite clock bias.

ρ_i^k : Geometric distance between satellite and receiver.

$d_{i(ion)}^k, d_{i(trop)}^k$: Delays imparted by the ionosphere and troposphere respectively.

c : Speed of light.

$d_{i(m)}^k$: Pseudorange multipath error.

Δ_R : Receiver's clock bias.

ε_i^k : Random noise.

Other error terms could be added to the above equation for more accurate modeling. For example, the signal delay between the signal generation and transmitting antenna of the satellite, and the signal delay between the receiving antenna and the signal correlator of the receiver.

Phase pseudorange is a measure of the difference between the phase of the satellite signal and the receiver's replica signal. The initial number of the full cycles between the satellite and the receiver, called integer ambiguity, is unknown. The basic equation of the phase measurement is given by the following:

$$\lambda \Phi_i^k = \rho_i^k + \lambda N_i^k - d_{i\ (ion)}^k + d_{i\ (trop)}^k + \delta_{i\ (m)}^k + c\Delta_R + c\Delta^S + \varepsilon_i^k \qquad (2.3)$$

where:

λ : Carrier wavelength.

Φ_i^k : Carrier phase observation.

N_i^k : Carrier phase integer ambiguity.

$\delta_{i(m)}^k$: Carrier phase multipath error.

Δ^S : Satellite's clock bias.

Similar to the code pseudorange, the total travel time could be divided to account for the signal delay inside both the satellite and the receiver. The existence of electrons in the ionosphere affects the propagation of the GPS signal. In contrast to the ionospheric delay of the code pseudorange, carrier phase signal is advanced by the same amount.

The Doppler measurement is a measure of the carrier phase rate. The equation for the observed Doppler scaled to the range rate takes the following form:

$$D_i^k = \lambda \dot{\Phi}_i^k = \dot{\rho}_i^k - \dot{d}_{i\ (ion)}^k + \dot{d}_{i\ (trop)}^k + \dot{\delta}_{i\ (m)}^k + c\dot{\Delta}_i^k + \dot{\varepsilon}_i^k \qquad (2.4)$$

where the dot indicates derivative with respect to time. Δ_i^k is the time derivative of the combined clock bias. Using the GPS principle explained earlier, the instantaneous velocity of the receiver could be estimated when Doppler measurements are observed from at least four satellites simultaneously.

2.1.5   GPS Error Sources

Besides measurement noise, GPS observables are affected by other error sources:
1. *Satellite and receiver clock biases*. The systematic bias of the satellite clock is modeled and transmitted as part of the navigational message. The receiver clock bias, the

difference between the GPS time and the receiver clock time, can be estimated together with the receiver's position or velocity. Using an appropriate linear combination of GPS observables, called Differential GPS (DGPS), both satellite and receiver clock biases can be eliminated. This is discussed later in more detail.

2. *Orbital Errors*. The broadcast orbital parameters are not perfect and therefore, produce incorrect satellite location. The expected contribution of this error as reported by Bowen (1986) might reach about 2 m for 24 hours prediction. The International GPS Service for Geodynamics (IGS) consists of a relatively dense global tracking network and analysis centers. The IGS centers produce a two weeks delayed reliable GPS orbital information with decimeter level of accuracy. For more information on the IGS services, the reader is referred to the IGS website at http://igscb.jpl.nasa.gov. The analysis of this study uses the broadcast orbits.

3. *Multipath*. As its name indicates, multipath is the arrival of the satellite signal at the receiver from multiple paths. The primary cause for multipath is the reflecting surfaces in the receiver's neighborhood. The multipath effect is frequency dependent; therefore, both code pseudorange and carrier phase are affected differently. Several techniques can be used to decrease or eliminate multipath effect; for instance, one method is to use a concentric GPS antenna that takes advantage of the GPS right-handed circular-polarized signal (Scherrer, 1985). Digital filtering is another method of reducing the effect of multipath (Bletzaker, 1985). A third method is taking ionospheric-free code ranges and carrier phases, and forming corresponding differences; all previously mentioned effects except for multipath cancel out. The residuals, apart from the noise level, thus, reflect the multipath effect (Hofmann-Wellenhof et al, 1992).

4. *Ionospheric Error*. The ionosphere is the atmospheric layer extending for about 50 km to 1000 km above the Earth's surface. The free electrons in this region delay GPS code pseudorange and advance carrier phase pseudorange. The Total Electron Content (TEC), along the GPS signal path, determines the effect of the ionosphere. The TEC depends on an 11-year cycle of sunspot activity, seasonal variations, elevation and azimuth of the satellite, and location of the receiver. Ionospheric effect can range from 0.15 m to 50 m.

Several methods can be used to eliminate or reduce the ionospheric effect. The most efficient is to use a linear combination of both GPS frequencies. For more details, see (Hofmann-Wellenhof et al, 1992). Another method for reducing ionospheric effect is to use broadcast ionospheric parameters, as part of the navigational message. These parameters model the effect of the ionosphere on the GPS signal. This study uses the Double Difference (DD) observation model, described in subsequent section, with DD ionospheric effect as part of the estimation process.

5. *Tropospheric Error*. Unlike the ionosphere, tropospheric effect is frequency independent. Therefore, the elimination of tropospheric effect using dual frequency receivers is not possible. The tropospheric layer extends to 50 km. The propagation delay of GPS signals through the troposphere depends on atmospheric conditions and the satellite elevation angle. The troposphere can be divided into dry air and wet air. The dry

part contributes about 90% of the total effect, and it can be accurately modeled to about 2-5% using surface measurements such as pressure and temperature (Leick, 1990). It is, however, more difficult to model the remaining 10% of the wet atmosphere due to variations of the water vapor in time and space. Nevertheless, models have been derived to estimate this effect (e.g., Modified Hopfied Model by Goad and Goodman, 1974). The lower the elevation angle of the incoming GPS signal, the more it is adversely affected because it must travel a longer path through the troposphere (Brunner and Welsch, 1993). Therefore, GPS observations from satellites with elevation angles below 15 degrees (mask angle) are avoided. The tropospheric error ranges between 2 m delay in the zenith to about 25 m at 5 degrees elevation angle. Using DD observation eliminates the tropospheric effect for short baselines. For long baselines, however, the DD tropospheric could be modeled as part of estimation process.

6. *Antenna Phase Center Offset*. The physical center of GPS antenna does not usually coincide with the phase center of the measurement. The offset can be divided into two parts: (1) A constant offset that can easily be taken into account by performing laboratory tests. (2) The variation offset, however, depends on the elevation, azimuth, intensity, and type of the GPS signal. This systematic variation is difficult to model because it differs from one receiver to another. Nevertheless, models for antenna offsets were proposed based on the azimuth and elevation of the satellite signal (Schupler et al, 1991).

7. *Relativistic Error*. The fundamental frequency of the satellite clocks is 10.23 MHz. This frequency is influenced by both special relativity, due to the difference of satellite velocity, relative to receiver velocity, and general relativity, due to the difference in the gravitational potential of the satellite's position, relative to receiver position. The prevailing portion of the relativistic effect is computed based on circular orbits. This effect is found to be equivalent to an increase in time of 38.3 μsec per day. Therefore, the fundamental frequency is adjusted by the amount of 0.00455 Hz to transmit at 10.229999995 MHz. The effect of eccentricity on the relativistic effect is about 48.8 nsec, and can be computed from simple mathematical models. This correction is usually applied in the receiver. In DGPS, where relative positions are computed, relativistic effects cancel out. For more details, the reader is referred to Ashby (1987).

2.1.6 Relative Positioning and Linear Combination of Observables

Many techniques have been used to enhance GPS capability and accuracy. Linear combinations of GPS measurements are often used to eliminate or reduce common errors. In this study, the DD linear combination (equation 2.5) of phase measurement is used, where two GPS satellites and two GPS receivers (base and rover) are involved. The base receiver is stationary at a known location and the relative position of the rover with respect to the base is to be determined. This process is called Differential GPS (DGPS).

$$\lambda_s \Phi_{ij,s}^{kl} = \rho_{ij}^{kl} + \lambda_s N_{ij}^{kl} - d_{ij,s\,(ion)}^{kl} + d_{ij\,(trop)}^{kl} + \delta_{ij\,(m)}^{kl} + \varepsilon_{ij}^{kl} \tag{2.5}$$

where:

$*_{ij}^{kl} = (*_i^k - *_j^k) - (*_i^l - *_j^l)$ alludes to the DD operator for terms in the above equation. The definition of the terms can be found in equation (2.3)

s : L_1 or L_2.

The quality of the GPS DD carrier phase observables depends on the baseline length between the base and rover receivers. As separation between the two receivers increases, a more reliable ambiguity resolution technique is needed. The DD ionospheric and tropospheric effects could also have a significant effect, and therefore, must be properly modeled.

2.2 Inertial Navigation System
2.2.1 Introduction

The Inertial Navigation System (INS) provides position and velocity of a moving platform using sensors that react to Newton's laws of motion. These sensors are called Inertial Measurement Units (IMU's), and are divided into two types: (1) gyroscopes, or gyros for short, and (2) accelerometers. Gyros sense angular rate while accelerometers sense linear acceleration. The subsequent sections introduce the fundamentals of the INS including mechanization, navigation and error equations, and INS initialization. INS error estimation is discussed later in Chapter 4.

2.2.2 Principle of Inertial Navigation

Navigation means determining position and velocity, with respect to a reference frame, usually in real time. The INS utilizes the inertial properties of its sensors (gyros and accelerometers) to solve for the navigation parameters given the proper initialization. In contrast to GPS, INS is self-contained and does not depend on external signals.

Gyros, as sensitive devices measuring angular rate, maintain the reference frame by providing changes in spatial direction. Thus, three orthogonal one-degree-of-freedom gyros are needed to maintain a three-dimensional frame. The accelerometer measures specific force, being the difference between kinematic and gravitational acceleration. Therefore, knowledge of the gravitational field is necessary for inertial navigation. Again, depending on the number of degrees of freedom associated with vehicle motion, a corresponding number of accelerometers is needed to be properly aligned. The time integration of "inertial" acceleration yields velocity, and the second time integration yields position. Figure 2.1 illustrates the inertial principle and computations for the strapdown mechanization. More on INS mechanization and the definition of different symbols appearing in Figure 2.1 comes later in this chapter.

Body-mounted Accelerometers → f^b → C^i_b → f^i → ◯ → $\iint ( )d\tau dt$ → r^i → Navigation Computation → φ, λ, h

Body-mounted Gyroscopes → ω^b_{ib} → Transformation Computation

Gravity Computation G^i

Initial Conditions

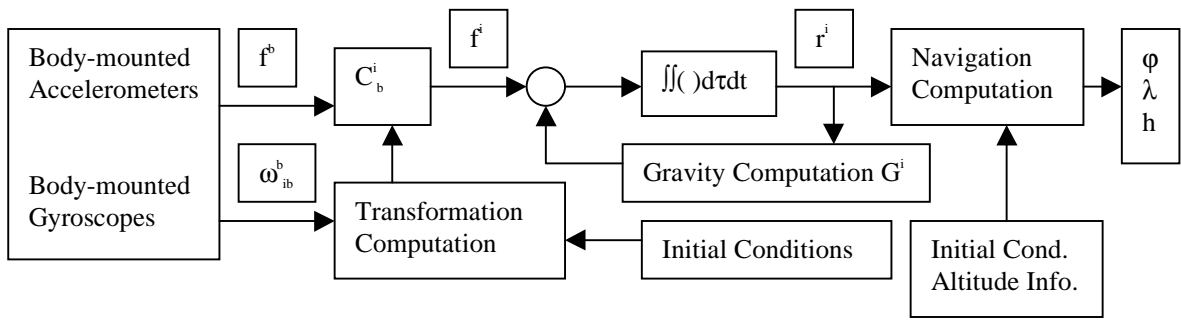Initial Cond. Altitude Info.

Figure 2.1: Inertial computation of strapdown system.

2.2.3 Coordinate Frames

Inertial navigation requires the user to define and to consider several coordinate frames, namely, the inertial frame, the Earth frame, the local level frame, the platform frame, the body frame, and the wander azimuth frame. As the term "coordinate system" refers to the physical theories and their approximations that are used to define the coordinate axes, the term "coordinate frame" refers to the accessible realization of the system through a set of points whose coordinates are monitored periodically. The inertial system is defined as one in which Newton's laws of motion hold. The Newtonian definition of inertial frame is one without rotation or acceleration. In the vicinity of the solar system, true inertial system cannot be realized because of the gravitational field. For that, Newton's laws must be modified to account for gravitation. The right-handed frame that is attached to the Earth's center and is in free-fall and not rotating, is called pseudo-inertial frame, or i-frame. Its orientation is fixed to quasars that have not shown any evidence of relative rotation (Jekeli, 1996).

The Earth-centered, Earth-fixed frame, or e-frame has its origin located at the center of mass of the Earth, and its axes are fixed to the Earth. The third axis of this right-handed coordinate frame is aligned with the mean axis of rotation. The first axis corresponds to the mean zero-longitude at the mean equator. The local level, also called the navigational frame, or n-frame, has its origin at the system's location, and its axes are aligned with north, east, and down directions. The down axis is aligned with the ellipsoidal normal. The body frame, or b-frame, is a right-handed Cartesian coordinate frame in which the measurements of the sensors are made. As the INS has a number of sensors mounted on a platform, the platform coordinate frame, or p-frame, is needed as a transition between the b-frame and n-frame. Finally, the wander azimuth frame, or w-frame, has its second axis not slaved to the north direction, otherwise, it is the same as n-frame. This frame was found useful at high latitudes, to avoid large rotations about the third axis, which are necessary to maintain the north direction. Working with the above coordinate frames, the transformation from one frame to another is unavoidable in the world of inertial navigation.

2.2.4 Inertial Measurement Units

The Inertial Measurement Units (IMU's) are of two types, gyros and accelerometers. The accelerometer's principle of operation is based on a proof mass that is suspended in a pendulous manner. Gyro operation principle, on the other hand, is based on measuring the reaction of a spinning proof mass. The modern gyro, however, utilizes the property of light propagation in a closed cavity of a rotating frame. This section describes the IMU's and their potential sources of errors.

2.2.4.1 Accelerometers

An accelerometer senses specific force (acceleration due to applied forces). It does not directly sense gravitational acceleration, but it senses the reaction imparted against this acceleration. Therefore, the accelerometer measurement cannot distinguish between reactions due to gravitation and applied actions. As depicted in the figure below, the modern accelerometer's degree of freedom is rotational, where the hinges along the second axis permit rotation about it. Acceleration in the direction perpendicular to the rotation axis will cause the proof mass to rotate about the second axis. The rotation is sensed by a signal generator at one end that creates a corresponding torque at the other end to null out the rotation. The first axis is called input axis; the second axis is called output axis; the third axis is called pendulous reference axis.
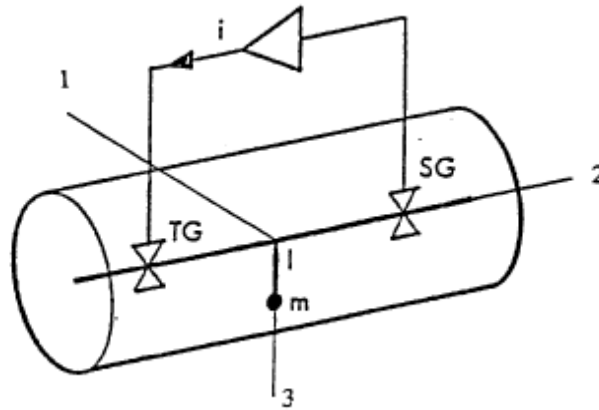
Figure 2.2: Torque rebalance pendulous accelerometer

The errors contaminating the accelerometer measurement include bias term, scale factor error, misalignment between the reference axis and the case axis, and random noise. The bias term could be caused by unmodeled effect. The scale factor consists of three parts: constant, linear, and quadratic scale to the input accelerations. Calibration, and careful design and mechanization, as well as error modeling and estimation are performed to minimize the effect of the errors.

2.2.4.2 Gyroscopes

Gyros are divided into two major groups: mechanical gyros and optical gyros. Newton's second law of rotational motion forms the basic principle of operation of the

mechanical gyros; if no torque is applied, the angular momentum is preserved. A single-degree-of-freedom gyro is depicted in the figure below.

The spinning proof mass (rotor) is supported by a gimbal that allows rotation about the output axis. The other two axes are the input axis and the spin axis. The rotation is sensed by a signal generator at one end of the gimbal, which creates a corresponding torque on the other end in a process called rebalance loop.

Several error sources that affect mechanical gyro measurement include scale factor error, drift term, misalignment between rotor and gimbal axes, acceleration dependent drift, squared-acceleration dependent drift, and random noise. Laboratory calibration can determine errors associated with individual gyros. Compensation can be applied for environmental factors such as temperature and real-time or post-mission estimation techniques are used to compute modeled drifts and biases.

The optical gyro's principle of operation is based on the Sagnac effect. The Sagnac effect relates to the propagation property of light inside a closed cavity in a rotating frame. Being massless, light acting as the sensor element of the gyro should not be affected by the dynamics of the environment in which the gyro finds itself; it is thus the natural alternative to the mechanical gyro in the unstable deployment of the strapdown mechanization (Jekeli, 1996). More on INS mechanization comes later in subsequent section.
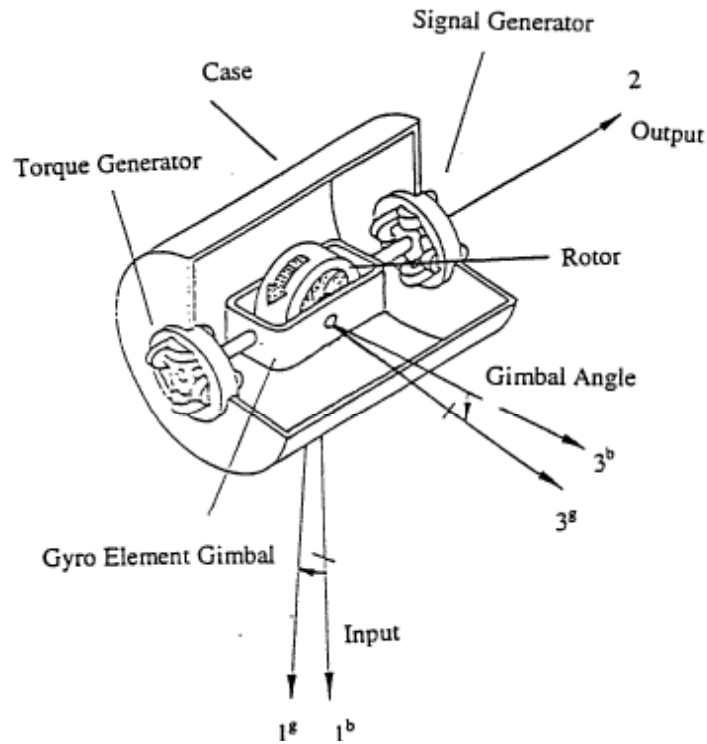
Figure 2.3: Single-degree-of-freedom gyroscope.

The Ring Laser Gyro (RLG) consists of a closed light beam path in a resonant cavity as shown in Figure 2.3. Two light beams traveling in opposite directions are used
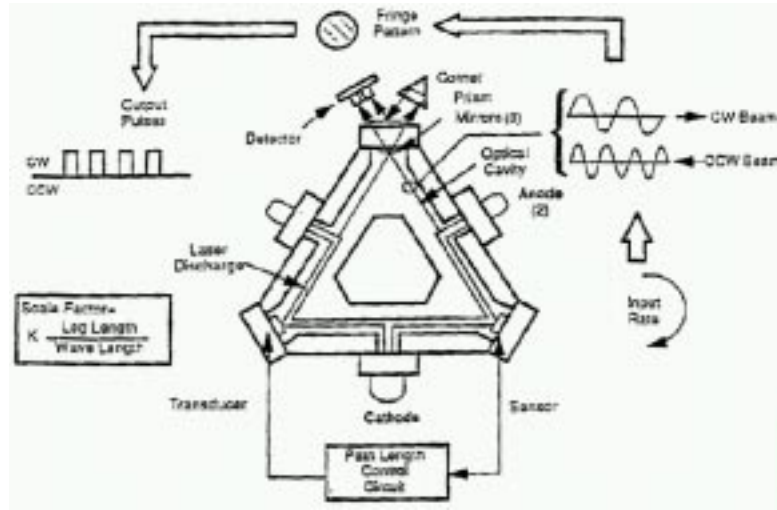
Figure 2.4: Schematic of ring laser gyro (Honeywell H-423 design)

to create a fringe pattern corresponding to the angular rate. As the number of wavelengths N inside the resonant cavity remains constant, the apparent change in length ΔL of the resonant cavity implies change in the wavelength.

$$L = N\lambda \qquad (2.6)$$

$$\Delta L = N\Delta\lambda \qquad (2.7)$$

One significant problem of RLG is the inability to sense small rotations. This problem is called frequency lock-in problem. To overcome this problem, an alternating bias (dithering) is imposed about the gyros' sensitive axis. As the bias changes its direction, RLG has a quick pass over the lock-in region where it cannot sense the actual rotation. The resulting error can be statistically modeled as random walk (see Chapter 4).

A new technique has been implemented on the Litton's zero-lock RLG (LN100). It uses two pairs of light beams. The oppositely imposed bias on each pair results in error cancellation, while doubling the input signal. The Fiber Optical Gyro (FOG) uses new technology to detect angular rates by measuring the phase difference of two light beams traveling through a coil of optic fiber. This technology has been implemented in Litton's LN-200 inertial navigator. The FOG is less accurate than RLG, however, it is more reliable.

The error model of optical gyros contains three main types of errors: scale factor error, drift error, and random noise. The drift error consists of constant bias, temperature and temperature gradient bias, magnetic field dependent bias, and misalignment and time

dependent bias. Several sources of errors can be calibrated and compensated in the output data. Other errors can be statistically modeled and estimated in real time or post-mission.

2.2.5   Mechanization

The INS mechanization refers to how its sensors are mounted, with respect to the body and inertial frames. Two main groups of mechanization are used, namely, stabilized platform and strapdown formation. Stabilized platforms are further divided into space-stabilized and local-level stabilized inertial systems.

2.2.5.1 Stabilized Platforms

The space-stabilized inertial navigator consists of three gyros and three accelerometers. The three untorqued gyros are mounted on a gimbaled platform. These gimbals are commanded to maintain the orientation of the gyros in an inertial frame using servo motors, thus, isolating the platform from vehicle motion. The accelerometers are mounted on the space-stabilized platform to measure specific forces as the difference between inertial acceleration and gravitational acceleration.

The more popular local-level stabilized inertial navigator has its gyros torqued proportional to the vehicle's angular velocity to maintain local level (east, north, and down) coordinate frame. As the vertical channel is not as stable as the horizontal ones, many applications require only horizontal navigation parameters where two perpendicular accelerometers, parallel to the platform, sense horizontal accelerations. The commanded gyros follow the local horizon introducing natural resonant behavior resulting in bounded bias with amplitude equal to the initial orientation error and period of 84.4 minutes "Schuler period." The commanded angular rate is given by:

$$\omega_t = \begin{pmatrix} (\dot{\lambda} + \omega_e)\cos\phi \\ -\dot{\phi} \\ -(\dot{\lambda} + \omega_e)\sin\phi \end{pmatrix} \tag{2.8}$$

where $\dot{\phi}$ and $\dot{\lambda}$ are the latitude and longitude rates, ω_e is the rotation rate of the Earth. These values are related to Earth-referenced velocity that can be obtained from integrating the accelerations.

2.2.5.2 Strapdown Mechanization

In the strapdown mechanization, the INS is physically bolted (or may be with vibration isolators) to the vehicle. The strapdown system has the advantage of being smaller, more reliable, and less expensive. The best stabilized platform system is more accurate than the best strapdown system. Nevertheless, strapdown INS advantages outweigh the difference in accuracy for many applications. In strapdown mechanization, the sensed acceleration must be transformed from the b-frame to the n-frame by computing the necessary transformation matrix. In addition to extra computation requirements for strapdown systems, the inertial sensors are subjected to the entire vehicle dynamic environment. The performance of inertial sensors under such conditions

is expected to be lower than stabilized systems where the inertial sensors are isolated from the vehicle dynamics. If other navigation sensors such as GPS are considered to aid strapdown INS, the performance difference with gimbaled systems become less.

2.2.6 Navigation Equations

Newton's second law of motion, modified for gravitational field, forms the fundamental equation from which the navigation equations are derived.

$$f^i = \ddot{r}^i - \bar{g}^i \tag{2.9}$$

where:

$\ddot{r}^i$: Second time derivative of the position vector.

$\bar{g}^i$: Vector of gravitational acceleration.

f^i : Specific force. Superscript i denotes the vectors are expressed in the i-frame.

As specific force measurements are given in the sensor b-frame, and the gravitational vector in the e-frame, the following orthogonal transformation matrices are used to transform these vectors to the i-frame.

$$f^i = C_b^i f^b \tag{2.10}$$

$$\bar{g}^i = C_e^i \bar{g}^e \tag{2.11}$$

The time derivative of the transformation matrix C_b^i is related to the angular velocity ω_{ib}^b, from the b-frame to the i-frame coordinated in the b-frame, through the following differential equation:

$$\dot{C}_b^i = C_b^i \Omega_{ib}^b \tag{2.12}$$

where Ω_{ib}^b is skew symmetric matrix of angular velocities ω_{ib}^b.

Equation (2.12), together with equation (2.9), which can be transformed into six first-order differential equations by introducing three new variables, form the navigation equations of INS in the i-frame:

$$\begin{pmatrix} \dot{C}_b^i \\ \dot{r}^i \\ \dot{v}^i \end{pmatrix} = \begin{pmatrix} C_b^i \Omega_{ib}^b \\ v^i \\ C_b^i f^b + C_e^i \bar{g}^e \end{pmatrix} \tag{2.13}$$

where v^i is the velocity vector in the i-frame. Note that the system's solution describes the dynamic motion by position, velocity, and attitude parameters. The measured quantities are the specific force vector and the angular velocity vector. The gravitational vector, however, is approximated or assumed to be known.

As it is more convenient to express the navigation parameters in the e-frame, equation (2.13) can be written as follows:

$$
\begin{pmatrix} \dot{C}_b^e \\ \dot{r}^e \\ \dot{v}^e \end{pmatrix} = \begin{pmatrix} C_b^e (\Omega_{ei}^b + \Omega_{ib}^b) \\ v^e \\ C_b^e f^b - 2\Omega_{ie}^e v^e + g^e \end{pmatrix}
\tag{2.14}
$$

where the gravity vector g^e is given by:

$$
g^e = \overline{g}^e - \Omega_{ie}^e \Omega_{ie}^e r^e
\tag{2.15}
$$

Modeling the navigational equations in the n-frame is called Earth's referenced formulation; the velocity components are given along the local directions (NED), and the position is given in terms of latitude, longitude, and height. These equations have the following form:

$$
\begin{pmatrix} \dot{C}_b^n \\ \dot{r}^n \\ \dot{v}^n \end{pmatrix} = \begin{pmatrix} C_b^n (\Omega_{ib}^b - \Omega_{in}^b) \\ D^{-1} v^n \\ C_b^n f^b - (2\Omega_{ie}^n + \Omega_{en}^n) v^n + g^n \end{pmatrix}
\tag{2.16}
$$

where the matrix D converts horizontal velocity components from linear to angular form, and inverts the vertical component:

$$
D = \begin{pmatrix} R+h & 0 & 0 \\ 0 & (R+h)\cos\phi & 0 \\ 0 & 0 & -1 \end{pmatrix}
\tag{2.17}
$$

So far, navigation equations formed as differential equations relating navigation parameters to INS measurements are shown in different coordinate frames. In the following, the differential equations showing the effect of sensors errors on navigation parameters will be discussed through perturbation technique in the next chapter. However, a simplified form, where zero Earth-referenced velocity is assumed, and gravity gradient terms are neglected, is shown in the next section on the INS initialization process.

2.2.7 INS Initialization

The process of finding the initial angular relationship between the instrument body frame and the navigation frame is called initial INS alignment. This process also involves the determination of sensor biases that have stochastic models associated with them. The importance of this process can be realized by knowing the direct impact of its results on error behavior and navigational accuracy. Initial alignment can be achieved by

using external optical devices. To avoid external dependencies, an alternative approach of a self-contained type of initial alignment known as acceleration-coupled gyrocompassing (Jekeli, 1996) is used to align the gimbaled platform type of INS. This approach utilizes raw INS data to generate feedback signals to level the gyros and perform azimuth alignment. For strapdown systems, similar self-alignment gyrocompassing process could be achieved analytically since the gyros cannot be rotated without rotating the entire vehicle. A two-stage scheme is used to achieve the INS alignment process. The first is the "coarse" or analytical alignment, which utilizes sensor output as well as the gravity vector and station coordinates. The coarse alignment stage is used to obtain fast initial estimation of the transformation matrix between the two frames. The second stage is "fine" or corrective alignment. At this stage, the initial approximations are refined using Kalman filtering technique to estimate initial misalignment and calibration parameters by utilizing stationary sensor output. As fine alignment uses first-order error estimation, coarse alignment results must be close for the system to converge. The null velocity of a stationary system could be used as an external measurement update to the Kalman filter. Unfortunately, not all biases and drifts can be estimated by using the raw velocity output of the INS. In addition, and as will be shown later, initial azimuth misalignment is more difficult to determine than other biases and orientation errors. The initial alignment process could be extended as the vehicle or aircraft carries out few maneuvers to excite the inertial sensors, the gyros in particular. The direct impact of this process will be shown as part of this study's results. More details, including the mathematical model of INS error states will be considered in the next chapter.

2.3 Photogrammetry
2.3.1 Introduction
Photogrammetry is not a navigation system like GPS or INS . The main use of photogrammetry is to produce topographic maps from photographs (Kraus, 1992). Modern digitizing instruments yield what is called a Digital Terrain Model (DTM) that provides valuable information for land use and other utilization. This information can be stored, processed, and analyzed in various ways for many Geographical Information System (GIS) applications. Another important use of photogrammetry is to densify networks of ground points for further surveyor boundary determination (cadastral survey). Furthermore, close-range photogrammetry (1–100 m) has found many applications, from medical experiments to automobile accidents.

2.3.2 Photogrammetric Orientation
The orientation of a photograph is divided into interior and exterior orientation. Interior orientation defines the geometry of the bundle of light rays emerging from the perspective center to the points in the object space. The perspective center coordinates, x_p, y_p, and c, in the image coordinate system, together with the geometric distortion characteristics of the lens system, define the interior orientation of a photograph. The image coordinates of the principal point x_p and y_p are the foot drop of the perspective center into the image plane. c is the calibrated focal length. Exterior orientation parameters define the position and attitude angles of a photograph, with respect to an

object coordinate system. The position is defined by the object space coordinates of the perspective center. The attitude, on the other hand, is defined by three rotation angles commonly known as omega (ω), the primary rotation about the first axis, phi (φ), the secondary rotation about the second axis, and kappa (κ), the tertiary rotation about the third axis. The three photogrammetric rotation angles are equivalent to roll, pitch, and heading known to the GPS and INS users. The photogrammetric exterior orientations, as explained above, could be achieved by what is called relative orientation and absolute orientation processes. The relative orientation between two overlapping photographs corresponds to coorientation between the photographs in some arbitrary space at the time of exposure. The absolute orientation, on the other hand, transforms the relatively oriented photographs into ground coordinate system by using auxiliary sensors or ground control points. In this study, the photogrammetric simulation process uses minimal ground control points in the first pair of photographs to establish the absolute orientation. Once the absolute orientation is established, relative orientation, through pass points, can be used to connect the rest of photographs to the ground coordinate system.

2.3.3 Photogrammetric Modeling

The mathematical model that relates image coordinates to object coordinates is the collinearity transformation. Geometrically, this model states that image point, perspective center, and object point must lie on a straight line. The model equations can be written as follows:

$$x = x_p - c\frac{r_{11}(X - X_0) + r_{21}(Y - Y_0) + r_{31}(Z - Z_0)}{r_{13}(X - X_0) + r_{23}(Y - Y_0) + r_{33}(Z - Z_0)}$$

$$\text{(2.18)}$$

$$y = y_p - c\frac{r_{12}(X - X_0) + r_{22}(Y - Y_0) + r_{32}(Z - Z_0)}{r_{13}(X - X_0) + r_{23}(Y - Y_0) + r_{33}(Z - Z_0)}$$

where x and y are the image coordinate measurement. The interior orientation parameters, x_p, y_p, and c, are usually known from the manufacturers for metric cameras. X_0, Y_0, Z_0 are the perspective center coordinates in the ground coordinate frame. These coordinates, together with the three rotation angles that relate the image coordinate frame with the ground coordinate frame, are called the exterior orientation parameters. X, Y, Z are the tie or pass point coordinates in the ground coordinate frame. The pass points are common points appear in two or more photographs and used to connect individual photographs in the flight direction. Tie points, on the other hand, are common points between adjacent strips. The direction cosine (transformation) matrix, r_{ij} contains the three orientation angles. The matrix r_{ij} is obtained from successive multiplication of three elementary rotation matrices. After each rotation, the image frame axes have a new orientation with respect to object coordinate axes. Therefore, the transformation matrix depends on the hierarchy of the three rotations. The transformation matrix is given with more details in Appendix D. It is worth mentioning that other mathematical models that relate image and object coordinates do exist (e.g., projective

transformation and direct linear transformation). However, the most fundamental in analytical photogrammetry is the collinearity transformation model.

The above collinearity model represents the observation equations where each measured point in the image gives two observation equations. The collinearity model could be used to solve different photogrammetric problems. However, before equation (2.18) can be used in the adjustment computation, it must be reduced to a linear form and a measurement random noise is also added to the mathematical model. Assuming known interior orientation parameters and using least squares adjustment notation and solution, the linearized form of the collinearity equations can be written as follows:

$$y = A_1 \xi_1 + A_2 \xi_2 + e \qquad\qquad e \sim (0, \sigma_0^2 P^{-1}) \tag{2.19}$$

where:

$y_{(nx1)}$: Observation vector, contains the measured minus computed image coordinates; n is the number of observations.

$A_{1(nxm1)}$: Coefficient matrix of ξ_1 parameters. It contains partial derivatives of the observation equation with respect to the unknown exterior orientation parameters (m_1 equals six times the number of photographs).

$\xi_{1(m1x1)}$: Corrections to the six exterior orientation parameters.

$A_{2(nxm2)}$: Coefficient matrix of ξ_2 parameters; m2 is the number of unknown ground coordinates.

$\xi_{2(m2x1)}$: Corrections to tie and pass point coordinates.

$e_{(nx1)}$: Random error vector of measurements.

$P_{(nxn)}$: weight matrix of the observations.

σ_0^2 : Variance of unit weight.

Let $\quad N_{ij} = A_i^T P A_j, \qquad c_i = A_i^T P y$,

The normal equations can be written as follows:

$$\begin{pmatrix} N_{11} & N_{12} \\ N_{21} & N_{22} \end{pmatrix} \begin{pmatrix} \hat{\xi}_1 \\ \hat{\xi}_2 \end{pmatrix} = \begin{pmatrix} c_1 \\ c_2 \end{pmatrix} \tag{2.20}$$

More on normal equations and normal matrix are detailed in Appendix E. Solving for $\hat{\xi}_1$ parameters only gives the following reduced normal equations:

$$(N_{11} - N_{12} N_{22}^{-1} N_{21}) \hat{\xi}_1 = c_1 - N_{12} N_{22}^{-1} c_2 \tag{2.21}$$

or,

$$\hat{\xi}_1 = (N - N_{12} N_{22}^{-1} N_{21})^{-1} (c_1 - N_{12} N_{22}^{-1} c_2) \tag{2.22}$$

Once the exterior parameters are available, the coordinates of the tie and pass points can be determined by:

$$\hat{\xi}_2 = N_{22}^{-1} c_2 - N_{22}^{-1} N_{21} \hat{\xi}_1 \tag{2.23}$$

The estimated variance covariance matrix of the adjusted exterior orientation parameters is given by:

$$\hat{D}\left\{\hat{\xi}_1\right\} = \hat{\sigma}_0^2 (N_{11} - N_{12} N_{22}^{-1} N_{21})^{-1} \tag{2.24}$$

$$\hat{\sigma}_0^2 = \frac{\tilde{e}^T P \tilde{e}}{n - m_1 - m_2} \tag{2.25}$$

$$\tilde{e} = y - A_1 \hat{\xi}_1 - A_2 \hat{\xi}_2 \tag{2.26}$$

with $(n-m_1-m_2)$ degrees of freedom.

The photogrammetric solution to the exterior orientation parameters and the coordinates of the pass points is strengthened by the fact that pass points add geometrical connection to the individual photographs. Terrestrial observations and constraints could also be used to enhance the photogrammetric solution. However, exploring this direction is beyond the scope of this study. The simulated set of photographs used in this study has about 15 pass points in each photograph. The number of pass points depends on the density of the simulated pass points on the ground and the orientation of the photograph at the time of exposure. More details on the simulation process come later in Chapter 5.

2.3.4 Photogrammetric Aerotriangulation and Ground Control

Although this research does not delve into the photogrammetric aerotriangulation, this process is directly related as the photogrammetric derived orientation parameters are used together with GPS/INS to extract gravity information. The following briefly describes the aerotriangulation process and sheds some light on a few important operational requirements.

The use of GPS technology in conjunction with the collection of aerial photography has the advantage of performing accurate flight navigation and reducing the amount of ground control points acquired by traditional surveying. The real-time kinematic GPS positioning allows continuous trajectory determination of the aircraft. This information can be used to control the flight path and exposure stations as close to a preplanned position as possible. Besides the savings in time and effort, photogrammetric aerotriangulation has the potential to utilize other remote sensing devices for control densification and real-time mapping applications. Operational requirements, however, are crucial to the success of the flight mission. These general requirements include, but are not limited to, the following:

mounting GPS antenna: It should be mounted in a place where obstruction to the GPS signal is minimum. Unfortunately, cycle-slips do occur in practice as a result of aircraft turning, change in GPS satellite constellation, or weakening of the GPS signal. Using recent developments of advanced filtering techniques and sophisticated software in conjunction with other sensors or navigation system (e.g., INS), the integer ambiguities could be resolved almost in real-time.

Receiver-camera connection: The camera exposure time must be registered on the GPS receiver's time scale. This can be accomplished by the GPS receiver signaling to the camera at exposure times. To ensure the time synchronization between GPS data and camera data for this work, the simulated images were collected simultaneously at every 10th GPS epoch along the flight trajectory. More about the process of simulation comes later in Chapter 5.

Antenna-camera offset: The GPS receiver stores the position information of the GPS antenna at exposure time. The required position, however, is the position of the exposure station. This offset can be estimated using close-range photogrammetry and the attitude angles of the aircraft during the flight mission. The offset corrections do not require accurate attitude angles and may be simplified to constants in many cases, especially if the GPS antenna is mounted directly above the camera (Ackermann, 1992). The horizontal offset for one degree tilt and one meter vertical offset is about 1.7 cm. During the process of photo simulation, and without losing generality, it is assumed that the GPS antenna and the camera are close enough that the spatial distance could be neglected or can be preserved through conventional surveying. In this study, it is important to notice that the GPS-derived position was not used as an external observation in the photogrammetric solution to extract the orientation parameters. Only minimum ground control points were used.

INS-camera offset: Adding INS to the photogrammetric triangulation sensors requires the computation of the spatial offsets between the camera and the INS. Both the camera perspective center and the INS body coordinate center are physically accessed locations. Similar to the antenna-camera offset, close range photogrammetry or conventional survey could be used to determine the INS-camera separation. In contrast to the antenna location where it has to be mounted on the top of the aircraft, the INS could be placed very close to the camera position. The maximum spatial offset for the flight test used in this study was about 0.34 m in the y-direction. In the case of large spatial INS-camera separation, the orientation offset could be indirectly determined through post mission estimation. The photogrammetric solution determines the orientation between the image coordinates frame (camera frame, see Appendix D) and the object coordinate frame, C_c^o. The INS, on the other hand, provides the rotations between the INS body frame and the navigation frame, C_b^n (see Appendix D). The INS-camera orientation offset, C_c^b, is determined by converting the object coordinates into navigation frame as shown in equation (2.27).

$$C_c^b = C_n^b C_o^n C_c^o \qquad (2.27)$$

All transformation matrices are assumed orthogonal, so their inverses equal their transposes. This study considers the object frame to be the navigation frame, i.e., $C_o^n = I$. For more details on INS-camera separation, see Skaloud, et al. (1994). The relationship between the orientation parameters of the INS (pitch, roll, and heading) and the orientation angles derived from photogrammetric solution (omega, phi, and kappa) is derived in Appendix D.

Ground control consists of a set of identifiable points on the ground with coordinates referred to a specified datum. These points are necessary to establish the position and orientation of photo images in space relative to the ground at the time of exposure. One of the objectives of this study is to investigate photogrammetric aerotriangulation for orientation accuracy with minimal cost of establishing a ground control network, especially, in the areas of rugged or inaccessible terrain where gravimetric survey is needed. Errors in the control points cannot be detected when minimum ground control points are used, however. The location and spacing of the ground control points are affected by accessibility, required accuracy, size and shape of the region to be photographed, and by the method of aerotriangulation to be utilized (Slama, et al 1994).

In the set of images simulated for this research, three ground control points are established in the first pair of photographs for every set of twenty-five photographs. The total number of photographs along the flight path is 150 photographs. More on the simulation process and ground points used will come later in subsequent section.

2.3.5 Bundle Adjustment

The bundle adjustment software is an analytical tool for computing the orientation of the images, the interior orientation parameters, and the coordinates of the points from photogrammetric measurements. Basically, a bundle is created by each camera exposure. The perspective center and the points in the image define this bundle in a local image coordinate system. The bundle solution tries to shift and rotate these bundles of light-rays so that they fit to some given control points (Novak, 1991). Bundle adjustment is based on the collinearity transformation model.

The BSC solution is known as a bundle block adjustment. It has the advantage of using the most accurate model that relates image coordinates with their ground counterparts. Besides, this technique has the flexibility to incorporate different data sources, impose constraints, and solve for additional parameters. With a nonlinear relationship between the observations and the unknowns, approximations to the unknowns and iterations for convergent solution are necessary.

2.3.6 Correlation Analysis and Achievable Accuracies of the Exterior Orientation Parameters

The purpose of this section is to investigate the achievable accuracy for the exterior orientation parameters, taking into account a minimal use of ground control points. In addition, the correlation among the orientation angles as obtained from the photogrammetric bundle adjustment process will be exploited and analyzed.

The assumption of a random and uncorrelated process is usually assumed in the absence of better assessment. With the standard sixty-percent overlap, flight altitude of 1800 m, and medium image scale of 12000, a strip of twenty-five photographs was simulated. Normal angle frame camera with focal length of 152 mm is assumed. The aircraft's velocity of 100 m/s is also assumed. An exposure time interval of 10 seconds

would satisfy the sixty-percent overlap. The simulation process involves generation of Digital Elevation Model (DEM) and creation of image frames. The DEM is generated by a simple polynomial with about 70 m difference in elevation between the highest and the lowest simulated points. Based on the collinearity principle, the DEM points were projected back to the image coordinate frames. The image coordinates are deliberately contaminated with random noise to substitute for observational error. The standard deviation of the random noise is ± 3 μm ($1\mu m = 10^{-3}$ mm). Figure 2.5 shows the planimetric location of the perspective centers of the simulated photographs, the pass points, and the ground control points.

The photogrammetric orientations, as explained in Chapter 2.3.2, could be achieved by setting up three ground control points in the first pair of photographs to establish the absolute orientation. Relative orientation, thereafter, could be established through the pass points. The accuracy of the ground control is assumed to be ± 1 cm. More details on relative and absolute orientation processes can be found in Moffitt and Mikhail (1980).

In contrast to having ground control points distributed along the flight path, and to avoid the costly process of establishing those controls, especially in inaccessible areas, this simulation uses ground control points only in the first pair of photographs. As one might expects, the longer the flight without additional ground control points, the more deterioration of the accuracy of the points measured in the strip.

The bundle block adjustment program was used to analyze the precision and correlation of the orientation parameters. Figure 2.6 shows the standard deviation values for the orientation parameters. The increase in the standard deviation is clearly shown as the strip becomes larger and larger. The most precise parameter is the heading as it is controlled by the accuracy of the horizontal points measured in the strip. The accuracy of measuring vertical points in the photogrammetric mapping process is usually lower than for the horizontal points.
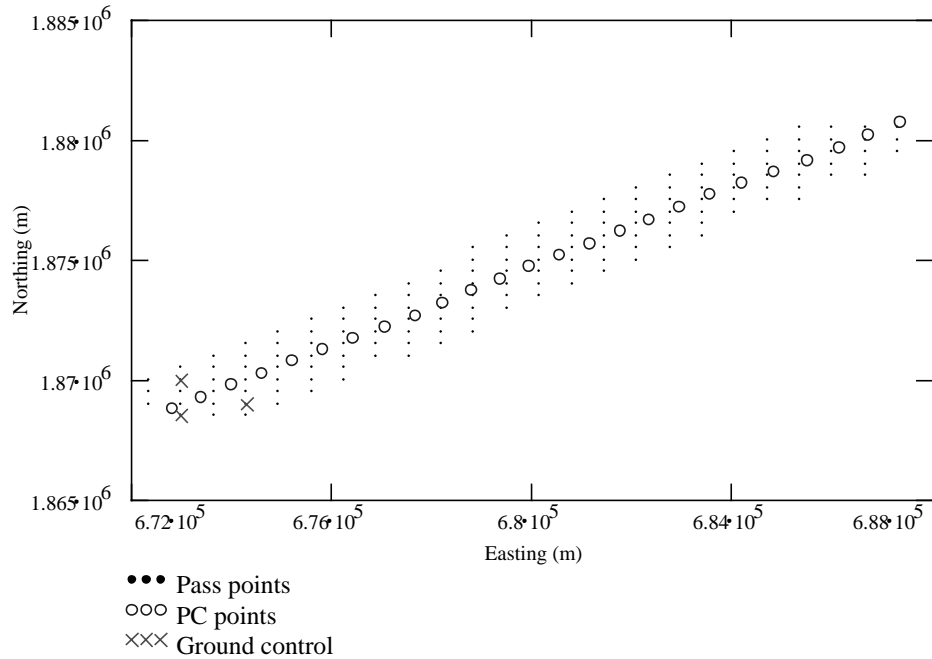
Figure 2.5: Perspective Centers (PC), pass points and horizontal ground control coordinates of the simulated photo strip.
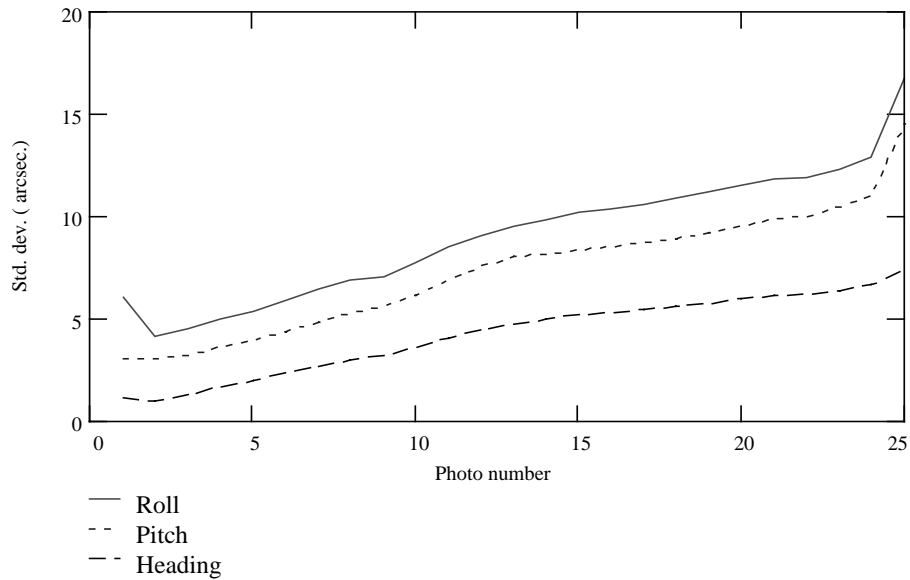
Figure 2.6: Standard deviation of the roll, pitch, and heading.

To assess the correlation of the orientation angles between epochs, the autocorrelation was computed from the full variance-covariance matrix provided by the bundle solution. The autocorrelation function for one epoch lag for the roll angle, for instance, is computed by averaging all cross correlation values of neighboring roll angles in the variance covariance matrix. Figure 2.7 shows the autocorrelation function for the

28

roll and pitch angles and their approximated exponential representation. The exponential curves approximate the correlation between a specific orientation angle and itself as time progresses. Figure 2.8 shows the corresponding values for the heading angle. The exponential representation of the autocorrelation function, as shown by equation (2.28), could be transferred into Gauss-Markov modeling in the Kalman filter estimation process. More discussion on correlation and state vector augmentation comes later in Chapter 4.

$$C_v(\tau) = \sigma_{0\,v}^2 e^{-\beta_v |\tau|} \tag{2.28}$$

The correlation time, β^{-1}, is a measure to the degree of correlation. The larger the value of β, the faster the correlation drops to zero. The inverse of β corresponds to the lag where the autocorrelation drops to 0.37 of its value at zero-lag (variance). For the three orientation angles, the inverse of β corresponds to values between 12 - 14 lag epochs.

It is important to notice that models, such as (2.28), used in this study are based on the assumption that the above statistical correlation is invariant with time (stationary process, see Chapter 4 for more on statistical modeling), even though Figure 2.6 shows that the variances increase with time. Also, the cross correlations between angles are neglected, even though they do exist. Figure 2.9 shows the cross-correlation function between the roll and pitch angels, for example.
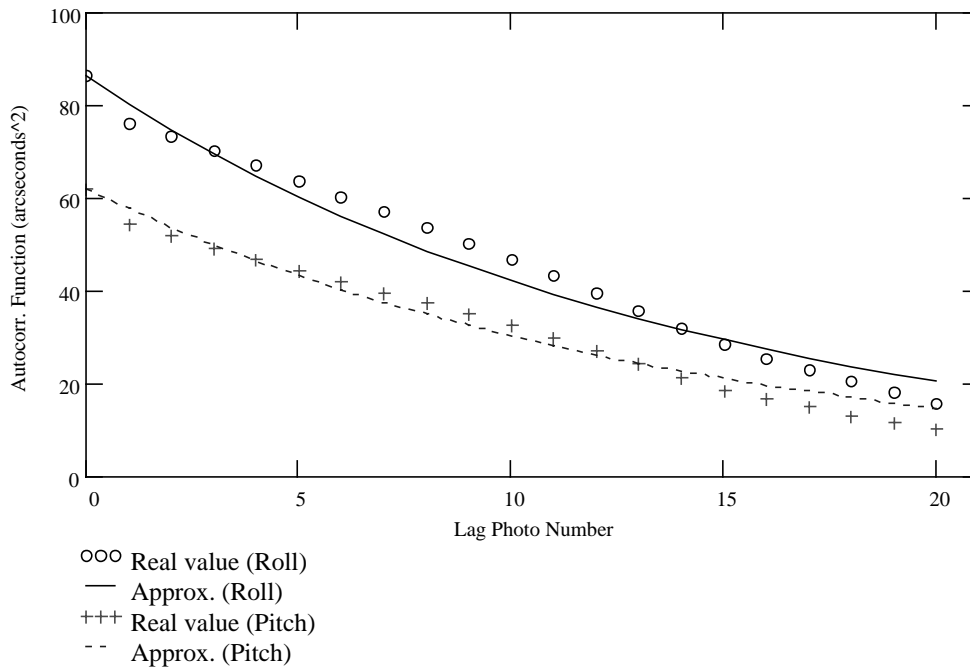

Figure 2.7: Autocorrelation function and its exponential approximation for both roll and pitch angles.
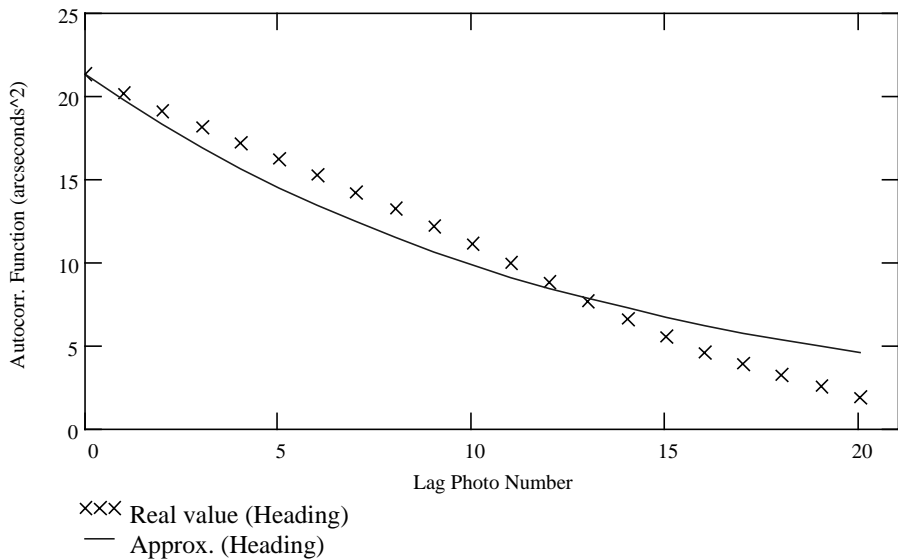
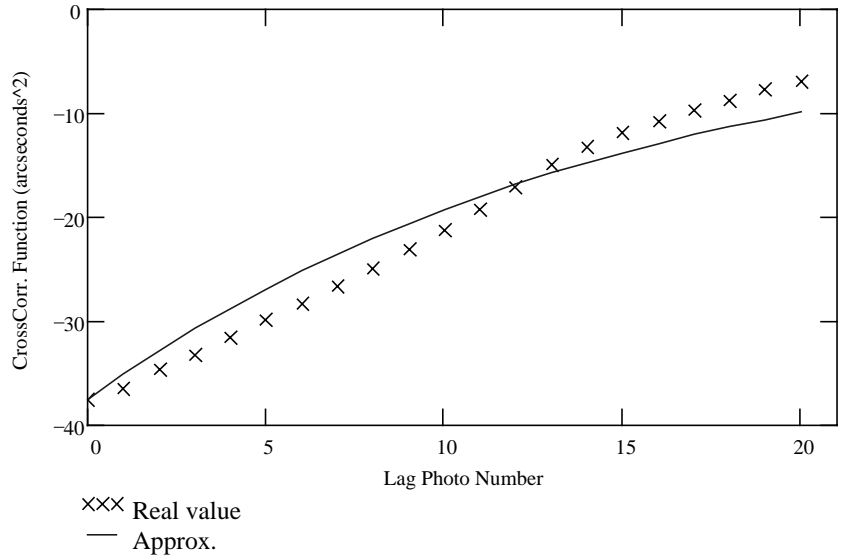Figure 2.8: Autocorrelation function and its exponential approximation for the heading.

Figure 2.9: Cross-correlation function and its exponential approximation between the roll and pitch angles.

CHAPTER 3

VECTOR GRAVIMETRY FROM INTEGRATION OF
INS, GPS, AND PHOTOGRAMMETRY

3.1   Introduction

The high accuracy positions (few centimeters) provided by DGPS makes this technology attractive to many civilian and military applications. The availability of GPS positions depends on a continual contact between enough GPS satellites and receivers and the success of the hardware processing the transmitted signals. Unfortunately, the continuity of GPS positions might be disturbed especially when data collection occurs near city buildings, under a bridge, inside a tunnel, or with hardware failure. The INS is mostly integrated with GPS to overcome these problems. In the field of airborne gravimetry, both systems of GPS and INS provide navigation information based on different principles. While GPS provides positions based on geometric measurements, INS gives positions and orientation based on inertial measurements of its sensors. These principles can be clearly shown in the following equation,

$$\ddot{r}^i = f^i + \overline{g}^i \qquad\qquad (3.1)$$

Where r is the position vector obtained from GPS, f is the specific force sensed by the INS accelerometers, and $\overline{g}$ is the gravitational acceleration. The above equation represents Newton's second law on motion in an inertial (non-rotating) frame on or near the Earth's surface.

Using GPS/INS for vector gravity determination means the ability to extract the gravitational acceleration in equation (3.1) from two types of measurements. First is the specific force measured by the INS accelerometers. Second, the second time derivative of position obtained from GPS.

As will be shown later in this chapter, vector gravimetry estimation from GPS/INS requires, in addition to accurate positions, precise attitude information. The gyro drifts represent one of the most critical sources of errors that prevent deflections of the vertical estimation. The inertial determination of the gravity vector depends on competence to separate the sensors' biases from the anomalous gravity field. One traditional method that helps achieve this separation is the zero-velocity update (ZUPT), where the vehicle is brought to a stop every few minutes during the survey mission.

The ZUPT approach, in many cases, might not be an option, especially for airborne applications. GPS, on the other hand, demonstrates abilities to provide accurate navigation parameters, and is considered as a complementary system to the INS for navigation. In this chapter, the underlying principle of integrating both data streams from INS and GPS for gravity determination is discussed. The INS error model is derived with emphasis on the estimability of its parameters. GPS observations and their required

accuracy for gravity estimation are elaborated. Finally, photogrammetric update sources will be investigated.

3.2   Principle of Inertial Gravity Determination

Inertial gravity vector recovery has been investigated in the past for terrestrial survey missions, but mostly on moving base at sea using some external aid to update the inertial system position and velocity. The inertial system error sources could be one of three major categories (Huddle, 1978); accelerometer related, gyroscope related, or environment related errors. In addition, the natural random noise will be present in the inertial system output. Depending on the application, some error terms could be more significant. The orientation error caused by initial misalignment and gyro drifts is critical to the inertial vector gravity determination. The following describes the GPS/INS model as applied to the field of vector gravimetry and briefly shows the associated error model. More on INS error modeling comes later in subsequent section.

The principle of inertial vector gravimetry is based on Newton's second law of motion modified for the presence of gravitational acceleration. From the last row of equation (2.16), and by decomposing the gravity vector into normal gravity and the gravity disturbance vector, the following equation can be reached:

$$\delta g^n = \dot{v}^n - \mathrm{C}_b^n f^b + (2\Omega_{ie}^n + \Omega_{en}^n)v^n - \gamma^n \tag{3.2}$$

The gravity disturbance vector δg is expressed in terms of the acquired quantities, f^b from the INS, and v and $\dot{v}$ from GPS. The transformation matrix C_b^n from the b–frame to the n-frame is obtained from the INS angular rate measurements. Both normal gravity and Coriolis accelerations (third term on the right-hand side) are computed from GPS position and velocity.

Linear perturbation to the given gravity disturbance in equation (3.2) gives the following:

$$\Delta\delta g^n = \delta f^n + \delta\dot{v}^n + (2\Omega_{ie}^n + \Omega_{en}^n)\delta v^n - \delta(\Omega_{ie}^n + \Omega_{in}^n)v^n - \overline{\Gamma}^n\delta p^n \tag{3.3}$$

$$\delta f^n = C_b^n\delta f^b + f^n \times \psi^n \tag{3.4}$$

where $\Delta\delta g^n$ is the error in the gravity disturbance δg^n, δf^n is the error in the sensed accelerations expressed in the n-frame; the raw measurements, however, are sensed in the accelerometer body frame. Equation (3.4) is based on the law of Coriolis; more on the law of Coriolis can be found in Britting (1971). Specific force vector sensed by accelerometers and orientation misalignments in the n-frame are represented by f^n and ψ^n, respectively. $\overline{\Gamma}^n = \partial g^n / \partial p^n$ is the tensor of gravity gradients; δp^n is the differential position vector along the n-frame axes and defined by equation (3.10). Equations (3.3) and (3.4) imply that errors in the GPS and INS measurements have direct effect on the determination of the vector of gravity disturbance.

The GPS contribution to the estimation errors enters in the terms δv^n and $\delta \dot{v}^n$, which are associated with numerical differentiation of position measurements, as well as the observation errors in position. Assuming decimeter level of accuracy for position, and few centimeters per second for velocity, the error terms generated by the last four terms of equation (3.3) are overshadowed by the first two terms, and therefore, can be neglected.

$$\Delta \delta g^n = f^n \times \psi^n - C_b^n \delta f^n + \delta \ddot{v}^n \tag{3.5}$$

These errors include orientation errors, accelerometer bias, and errors in derived vehicle acceleration. The difficulty of GPS/INS gravity vector estimation is evident in equation (3.5); it is again demonstrated more explicitly in the next section.

It turns out, as mentioned through the course of this study, that for the state-of-the-art inertial systems, the most serious error source for deflections of the vertical recovery is the orientation drift. This fact is illustrated in the above error model (see Equation 3.5) where the orientation errors are scaled by the sensed specific force vector. Even though it is not implemented in this study, it is important to know that in the field of kinematic vector gravimetry, in addition to the position and velocity updates to the inertial system, gravitational information at specified stations along the survey traverse could also be used for inertial drifts assessments (Huddle, 1978).

3.3   INS Error Model

The navigation equations in the n-frame are given by equation (2.16), repeated here for convenience,

$$\begin{pmatrix} \dot{C}_b^n \\ \dot{r}^n \\ \dot{v}^n \end{pmatrix} = \begin{pmatrix} C_b^n (\Omega_{ib}^b - \Omega_{in}^b) \\ D^{-1} v^n \\ C_b^n f^b - (2\Omega_{ie}^n + \Omega_{en}^n) v^n + g^n \end{pmatrix} \tag{3.6}$$

The above system of nonlinear differential equations describes the physical process of navigation. As the INS sensors are imperfect, the solution to the navigation parameters is erroneous. Therefore, error modeling and analysis are important to estimate these errors.

Linear perturbation to the above dynamic equations gives the differential change of the parameters from their true values. The linearized form is given by the following (Jekeli, 1996):

$$\dot{\psi}^n = -\omega_{in}^n \times \psi^n - C_b^n \delta\omega_{ib}^b + \delta\omega_{in}^n \tag{3.7}$$

$$\frac{\text{d}}{\text{dt}}\delta v^n = -\delta(\varOmega_{in}^n + \varOmega_{ei}^n)v^n - (\varOmega_{in}^n + \varOmega_{ie}^n)\delta v^n + \delta f^n + \bar{\varGamma}^n \delta p^n + \delta g^n \tag{3.8}$$

$$\frac{d}{dt}\begin{pmatrix} \delta\phi \\ \delta\lambda \\ \delta h \end{pmatrix} = \begin{pmatrix} \delta\dot{\phi} \\ \delta\dot{\lambda} \\ \delta\dot{h} \end{pmatrix} \tag{3.9}$$

where:

$$\delta p^n = \begin{pmatrix} (M+h)\delta\phi \\ (N+h)\cos\phi\,\delta\lambda \\ -\delta h \end{pmatrix} \tag{3.10}$$

M and N are the radii of curvatures in the meridian and in the prime vertical, respectively. $\bar{\varGamma}^n$ is the gravity gradient matrix; δf^n is the error in the sensed accelerations in the n-frame. Knowing that the accelerometers sense specific forces in the b-frame and the transformations from b-frame to n-frame have associated errors, δf^n must include the effect of these errors (cf. (3.4)). Combining the above equations, one can obtain a general error model that can be written in the following form (Jekeli, 1996):

$$\frac{\text{d}}{\text{dt}}\varepsilon^n = F^n\varepsilon^n + G^n u \tag{3.11}$$

where:

$$\varepsilon^n = \begin{pmatrix} \psi_N^n & \psi_E^n & \psi_D^n & \delta\dot{\phi} & \delta\dot{\lambda} & \delta\dot{h} & \delta\phi & \delta\lambda & \delta h \end{pmatrix}^T \tag{3.12}$$

$\psi_N^n, \psi_E^n, \psi_D^n$ are the orientation errors along NED directions. u consists of system error components: accelerometer bias and gyro drift in the b-frame, and error in gravity vector in the n-frame. These components form the forcing functions or system noise.

$$u = \begin{pmatrix} \delta\omega_{ib}^b \\ \delta a^b \\ \delta g^n \end{pmatrix} \tag{3.13}$$

$$G^n = \begin{pmatrix} -C_b^n & 0 & 0 \\ 0 & D^{-1}C_b^n & D^{-1} \\ 0 & 0 & 0 \end{pmatrix} \tag{3.14}$$

$$
F^n = \begin{bmatrix}
0 & -\dot{l}_1\sin\phi & \dot{\phi} & 0 & \cos\phi & 0 & -\dot{l}_1\sin\phi & 0 & 0 \\[4pt]
\dot{l}_1\sin\phi & 0 & \dot{l}_1\cos\phi & -1 & 0 & 0 & 0 & 0 & 0 \\[4pt]
-\dot{\phi} & -\dot{l}_1\cos\phi & 0 & 0 & -\sin\phi & 0 & -\dot{l}_1\cos\phi & 0 & 0 \\[4pt]
0 & \dfrac{-f_1^n}{r} & \dfrac{f_2^n}{r} & \dfrac{-2\dot{h}}{r} & -\dot{l}_1\sin2\phi & \dfrac{-2\dot{\phi}}{r} & \Gamma_{11}^n - \dot{\lambda}\dot{l}_2\cos2\phi & \Gamma_{12}^n\cos\phi & \dfrac{\ddot{\phi}+0.5\dot{\lambda}\dot{l}_2\sin2\phi+\Gamma_{13}^n}{-r} \\[10pt]
\dfrac{f_3^n}{r\cos\phi} & 0 & \dfrac{f_1^n}{r\cos\phi} & 2\dot{l}_1\tan\phi & 2(\dot{\phi}\tan\phi - \dfrac{h}{r}) & \dfrac{-2\dot{l}_1}{r} & \begin{array}{c} 2\dot{l}_1(\dot{\phi}+\dfrac{h\tan\phi}{r}) \\ +\ddot{\lambda}\tan\phi+\Gamma_{21}^n\sec\phi \end{array} & \Gamma_{22}^n & \dfrac{2\dot{\phi}\dot{l}_1\tan\phi - \ddot{\lambda} - \dfrac{\Gamma_{23}^n}{\cos\phi}}{r} \\[12pt]
f_2^n & -f_1^n & 0 & 2r\dot{\phi} & 2r\dot{l}_1\cos^2\phi & 0 & -r\dot{\lambda}\dot{l}_2\sin2\phi - r\Gamma_{31}^n & -r\cos\phi\Gamma_{32}^n & \dot{\phi}^2 + \dot{\lambda}\dot{l}_2\cos^2\phi+\Gamma_{33}^n \\[4pt]
0 & 0 & 0 & 1 & 0 & 0 & 0 & 0 & 0 \\[4pt]
0 & 0 & 0 & 0 & 1 & 0 & 0 & 0 & 0 \\[4pt]
0 & 0 & 0 & 0 & 0 & 1 & 0 & 0 & 0
\end{bmatrix}
$$

(3.15)

where:

$\dot{l}_1 = \dot{\lambda} + \omega_e$, and $\dot{l}_2 = \dot{\lambda} + 2\omega_e$

Γ_{ij}^n : Gravity gradient terms in the n-frame; i,j=1,2,3.

$r = R + h$: Mean radius of the Earth plus the ellipsoidal height.

f_i^n : Accelerometer measurements transformed to the n-frame; i=1,2,3.

D : Given by equation (2.17).

Note that the above system of equations involves some approximations; the Gaussian mean radius R is used as an approximation to the principal radii of curvature in the meridian and prime vertical. Also, the terms with second and higher order of magnitude of the second eccentricity are neglected. The order of error magnitudes introduced by using Gaussian mean radius approximation is shown in Appendix C where more rigorous derivation to the INS error model can be found.

Further reasonable approximations can be made to help characterize the error dynamics of the INS at the cost of introducing errors less than its sensors' biases. If gravity gradient components are neglected and zero Earth-referenced velocity is assumed, the orientation and horizontal components of equations (3.7-8) can be written as follows (Jekeli, 1996):

$$
\begin{aligned}
\dot{\psi}_N &= -\omega_e\sin(\phi)\psi_E + \cos(\phi)\delta\dot{\lambda} - \omega_e\sin(\phi)\delta\phi - \delta\omega_N \\
\dot{\psi}_E &= \omega_e\sin(\phi)\psi_N + \omega_e\cos(\phi)\psi_D - \delta\dot{\phi} - \delta\omega_E \\
\dot{\psi}_D &= -\omega_e\cos(\phi)\psi_E - \sin(\phi)\delta\dot{\lambda} - \omega_e\cos(\phi)\delta\phi - \delta\omega_D
\end{aligned}
$$

(3.16)

$$
\begin{aligned}
r\delta\ddot{\phi} + r\omega_e\sin(2\phi)\delta\dot{\lambda} - g\psi_E &= \delta a_N + \delta g_N \\
r\cos\phi\,\delta\ddot{\lambda} - 2r\omega_e\sin(\phi)\delta\dot{\phi} + g\psi_N &= \delta a_E + \delta g_E + 2\omega_e\cos(\phi)\delta v_D
\end{aligned}
$$

(3.17)

with the sensor's error terms coordinatized in the n-frame. The velocity and velocity rate components were substituted by angular rates and their derivatives according to the following:

$$\delta\dot{\phi} = \frac{\delta v_N}{R+h} \quad ; \quad \delta\dot{\lambda} = \frac{\delta v_E}{(R+h)\cos\phi} \tag{3.18}$$

$$\delta\ddot{\phi} = \frac{\frac{d}{dt}\delta v_N}{R+h} \quad ; \quad \delta\ddot{\lambda} = \frac{\frac{d}{dt}\delta v_E}{(R+h)\cos\phi} \tag{3.19}$$

A closer look at equations, (3.16) and (3.17), gives more insight about the interrelationship among the different sources of system errors and the ability to separate them by external information. The importance of the type of external and independent information introduced to the system comes from the ability of this new information to separate and estimate some or all of these weakly or directly coupled errors. Depending on priorities for different applications, different external aid could be used (e.g., terrestrial observations, stellar observations, laser ranges, gravity information, etc.). The direct relationship between the orientation errors (ψ) and the gyro drifts ($\delta\omega$) is obvious in equation (3.16). The orientation errors are directly coupled with the gravity disturbance vector (δg) as indicated by equation (3.17), (e.g., east orientation error, ψ_E, with north component of gravity disturbance, δg_N). Therefore, the importance to calibrate the gyros for gravity vector estimation makes it vital to introduce independent and accurate type of attitude observation to the GPS/INS system. Again, depending on the signal needs to be extracted, different external aid could be needed.

The INS initialization process, as described in Chapter 2, involves a determination of systematic errors (i.e., accelerometer biases and gyro drifts) in a least-squares estimation process. Because of their influence on the INS performance, it is important that stochastic models of these errors are correctly included. In addition to utilizing the zero velocity of stationary vehicle, the reactions to the gravitational accelerations and rotation rate of the Earth, the estimability of the systematic errors and initial misalignment depends on the availability of external sources of aiding information. The down gyro bias, for instance, is not directly connected to the vehicle's velocity. An external azimuth information would be a direct measure to the vertical orientation error ψ_D, and subsequently to the vertical gyro bias.

Precise positions and velocities of moving vehicles obtained from DGPS and pre-mission maneuvers that excite the gyros help to initialize the INS, including the estimability of the heading error ψ_D. In the field of inertial vector gravimetry, the coupling between gravity disturbance vector and orientation errors implies that external attitude information greatly helps in the estimation of longer wavelength components of the gravity disturbance vector. The effect of external attitude updates on vector gravimetry will be shown in Chapter 5. More on the INS initialization techniques to decouple INS errors can be found in Jiang and Lin (1992), Saab et al. (1994), and Jekeli (1996).

3.4 Accuracy of GPS Observables for Gravity Determination

Using GPS double-difference measurements, common atmospheric errors, orbital errors, and clock biases are canceled out. The dominant errors affecting the GPS-derived acceleration are multipath and GPS measurement noise. Multipath error is a function of receiver type and antenna characteristics, while the carrier phase measurement noise is a function of tracking bandwidth and signal to noise ratio.

To achieve accuracy of 1 mgal ($1 \times 10^{-5} m / s^2$) for the vector of gravity disturbance, the GPS aid must be supportive to this target. Under normal kinematic conditions, the measurement noise of double difference carrier phase is about 1.0 mm. Relative positioning using carrier phases is capable of achieving centimeter-positioning accuracy (Cannon, et al., 1987). The differentiation operator of position to get GPS velocity measurement amplifies the high frequency noise components. Conversely, these components are reduced by integration of INS accelerations (Salychev, 1995). GPS-derived acceleration is the most helpful to gravity vector estimation, as it is a direct measure to separate kinematic and gravitational accelerations. However, GPS high frequency measurement noise produces the dominant source of error in GPS derived accelerations. Using L1 carrier phase measurements at two stationary TOPCON Turbo SII receivers with 2.5 km separation, smoothing over 40 seconds was applied to achieve 1 mgal accuracy for GPS derived accelerations (Jekeli and Garcia, 1997). As the separation between the two receivers increase, other sources of errors could have significant effect, especially, the ionospheric effect, and therefore, smoothing to a longer interval is necessary for more accurate accelerations. For further discussion on the accuracy of GPS derived acceleration, see also Wei and Schwarz, (1995).

Especially in the estimation of the vertical component of gravity, using the double difference model and carrier phase measurements along with INS data is very supportive to the extraction process of the vertical component of gravity, and a lot of research has been done in this field for many years. Accurate GPS positions and/or velocities, however, are not sufficient to separate the horizontal components of gravity vector from the orientation errors because, at least in the short term, they provide no information on attitude of the system in the navigation frame. In Chapter 5, two methods to estimate the deflection of the verticals are compared; first, the INS/GPS estimation; second, the INS/GPS with photogrammetric orientation updates.

3.5 Photogrammetric Contribution to Gravity Determination

The position and orientation of the imaging sensors in the object coordinate frame (exterior orientation parameters) are required to extract photogrammetric information from the images. The exterior orientation parameters are usually determined by inverse photogrammetry. The process of inverse photogrammetry requires a large number of control points and highly skilled operators to measure image coordinates. In this section, the use of GPS and INS in aerial photography is briefly discussed, followed by a description of how these sensors (i.e., GPS, INS, and Camera) are utilized differently for vector gravity estimation.

The field of airborne GPS kinematic camera positioning is thoroughly investigated in recent years to minimize or even eliminate the need for ground control. Practical considerations to this investigation were briefly mentioned in Chapter 2. Using differential GPS, the exposure station position can be determined with sufficient accuracy for photogrammetric applications, and therefore, the position parameters of the exterior orientation become readily available. For the orientation parameters, a multi-antenna GPS receiver has been investigated (e.g., Lu et al., 1993; Cramer, 1995). It has been concluded that GPS attitude accuracy ($0.2^0 - 0.4^0$) can not be used for high-precision image orientation.

An alternative solution is utilizing the INS sensors for orientation parameters. Although the INS sensors have short-term stability, the errors grow rapidly with time. The synergism of GPS and INS for more accurate and stable orientation parameters has been an attractive option for photogrammetric mapping (e.g., Skaloud et al., 1994). Modeling the INS errors by time dependent moving spline functions has been investigated by Cramer and Schade (1995), where the function coefficients can be determined using both data streams of GPS and INS.

The contrary direction to the above investigations, however, is of interest here; the utilization of the sensors is reversed for vector gravity extraction. The key element to this direction is the superiority of the derived photogrammetric orientation that could applied for vector gravity estimation.

The determination of the gravity disturbance vector requires accurate and stable orientation parameters to constrain the gyro drifts. This study looks into the photogrammetric solution to the exterior orientation parameters for that purpose. In contrast to mapping applications, the gravity application uses the power of GPS and the orientation derived from inverse photogrammetry by using ground control to support the solution. The post mission accurate orientation parameters can be used to separate INS biases and lead, ultimately, to better estimation of the vector of gravity. Equation (3.17) (see also equation (3.5)) provides a rough estimate on how accurate the orientation parameters have to be to achieve specific level of accuracy in the horizontal components of the gravity vector. To achieve one arcsecond accuracy in the deflection components, the requirement on orientation accuracy comes close to one arcsecond assuming the following nominal values for the error terms in equation (3.17): 1 m/s for horizontal velocity, 0.01 m/s for the down velocity, $3*10^{-4}$ m/s^2 for horizontal acceleration, and $20*10^{-5}$ m/s^2 for accelerometer.

It is important to notice here that the photogrammetric derived orientation parameters have to be transformed into the computational frame of the system integration before they can be used. Therefore, any uncertainty in the transformation parameters must be considered. The photogrammetric orientation parameters used in this study are simulated in the local level frame, which has known transformation parameters to the navigation frame. Please refer to Appendix D for more details. Based on simulation analysis on bundle block adjustment using ground control, 3-4 arcseconds could be

achieved for omega and phi orientations, and 1-2 arcseconds for the kappa (Habib, 1998).

3.6   Estimation Algorithm for Kinematic Gravity Determination

The dynamic error equations were developed in section 3.3 to describe the behavior of the INS errors with respect to time. It is natural for physical systems to show random noise associated with their output. From knowledge of system behavior, the randomness of the system can be stochastically modeled. The system errors (states) can be estimated using external stochastic measurements that have a linear relationship with these states. It is important to note that the INS error equations were derived through linear perturbation of the navigation parameters, where second and higher order terms were neglected, and the deviation of these parameters from their true values are assumed small to validate the linear approximation. In the case that error states grow larger and larger, either the error model is not appropriate or the external aid does not contribute to restrain this error.

The Kalman filter has the advantage of accommodating different sources of information for time domain estimation. It is also optimal in the sense that the estimation is consistent, unbiased, and with minimum variance. However, this estimation technique is slaved to the success of statistically modeling the system and observational errors. Kalman estimation is well documented in the literature, e.g., Gelb (1974). Only the essentials of this recursive estimation are given. The stages upon which Kalman estimation was built are prediction, filtering, and smoothing. Based on system dynamics and initial values, prediction provides the propagation of the system states as time progresses. Filtering, as the most common estimation method, incorporates external observations, together with their statistical properties to yield better estimation of the states. Smoothing is the most accurate as it incorporates all available measurements before and after the estimation epoch.

The state variables x_k of a dynamic linear model is formally written as follows:

$$x_k = \Phi_{k,k-1} x_{k-1} + G_k w_k \qquad (3.20)$$

where $\Phi_{k,k-1}$ is the state transition matrix between times t_k and t_{k-1}. The state transition matrix and the input matrix G_k are assumed constant during transition times. The input disturbance vector w_k is described by Gaussian, zero-mean, white noise process.

$$w_k \sim N(0, Q_k) \qquad (3.21)$$

where Q_k is the covariance matrix of random system noise at t_k. It is assumed that both x_k and w_k are uncorrelated processes. At time t_k, a number of states or linear combination of states are measured according to the following measurement model:

$$z_k = Hx_k + v_k \tag{3.22}$$

where the vector v_k is assumed Gaussian, zero-mean, white noise process,

$$v_k \sim N(0, R_k) \tag{3.23}$$

Without new observations, the prediction equations are given by:

$$\hat{x}_k^- = \Phi_{k,k-1}\hat{x}_{k-1} \tag{3.24}$$

$$P_k^- = \Phi_{k,k-1}P_{k-1}\Phi_{k,k-1}^T + G_k Q_{k-1}G_k^T \tag{3.25}$$

where the $\wedge$ denotes an estimate, and the $^-$ denotes the absence of observation yet. An initial state vector with its covariance matrix is required to start the prediction process,

$$\hat{x}_0 = x_0 + e_0 \tag{3.26}$$

$$e_0 \sim N(0, P_0) \tag{3.27}$$

Both the system noise and the transition matrix are the decisive factors in state propagation. As external measurements are introduced, they update the state and its covariance matrix as follows:

$$\hat{x}_k = \hat{x}_k^- + K_k(z_k - H_k\hat{x}_k^-) \tag{3.28}$$

$$P_k = (I - K_k H)P_k^- \tag{3.29}$$

where:

$$K_k = P_k^- H^T(HP_k^- H^T + R_k)^{-1} \tag{3.30}$$

where K_k is called Kalman gain matrix; $z_k - H_k\hat{x}_k^-$ is called innovation vector.

Misleading results or even a divergent solution might be the outcome of Kalman estimation if an erroneous initial covariance matrix and/or oversimplification of the mathematical models are used. Numerical instability in the recursive algorithm (Equations (3.25) and (3.29)) might also cause the solution to diverge. Inaccurate mathematical description in the dynamic and/or measurement model will invalidate the estimation, and thus, any drawn conclusion based on it. It is, therefore, crucial to verify the validity of the assumed mathematical models.

The Kalman filtering estimation technique is utilized in this study to estimate the horizontal components of gravity disturbance vector δg, based on GPS positions and photogrammetric orientation updates to an inertial navigation system. The observation model of the Kalman filter (Equation 3.22) assumes that measurements are contaminated

only with white noise. The GPS carrier phase observations are assumed uncorrelated and having same accuracy (±1.0 mm). The double difference formulations from the observed phases, however, are correlated according to the law of variance-covariance propagation. Therefore, a decorrelation process, called homogenization (described later in Chapter 4), is applied to the GPS double difference observations before using them in the Kalman filter measurement update module.

The INS and GPS error models used in the Kalman filter of this study are described in Chapter 4. For photogrammetric orientation, however, the simulated data were plotted and a correlation analysis was done to derive a stochastic error model for the correlated photogrammetric orientation noise (see Chapter 2). The validity of the autocorrelation models used comes from the closeness of these models to the simulated data. As mentioned earlier in Chapter 2, the cross correlation between the orientation parameters is neglected.

The complication arises from the timely correlated orientation measurements requires a modification to the Kalman filter measurement model. As the measurement correlations are modeled into the dynamics equation, the measurement covariance matrix R becomes equal to [0] (Equation 3.22). The computational flow of the Kalman filter does not require R to be positive definite. However, $(HP_k^- H^T + R_k)$ must be invertible (Equation 3.30). The equations of the new measurement model are described with more details later in Chapter 4.

CHAPTER 4

STOCHASTIC MODELING AND INTEGRATION

4.1 Introduction

The measurement of any physical instrument has a random part associated with it, i.e., this measurement is not totally predictable as compared to a deterministic signal or output. Probabilistic description of random signals is used extensively in the field of optimal estimation based on prior knowledge on the behavior of the signal.

A set of random variables and the associated probabilistic distributions are called random or stochastic process. The random process is called *stationary in the strict sense* if none of the probability distributions characterizing the process change with time. *Stationary in the wide sense*, however, means that the mean and the covariance only do not change with time. One more concept that is usually assumed to characterize the process is *ergodicity*. The process is called ergodic if the stochastic characteristics of the process over time are equivalent to the stochastic characteristics over the ensemble of all possible realizations of the process. The following two sections discuss the stochastic error models and the dynamics model used in this study. Section 4.4 describes different ways of combining GPS and INS data streams with emphasis on tight GPS/INS integration. Loosely integrated process of camera data with GPS/INS is discussed in section 4.5. Finally, section 5.6 commented on the process of tightly integrated camera, GPS, and INS data streams.

4.2 Stochastic Error Models

This section briefly describes the stochastic models used for the Kalman filter error states of this work. Some of these error models prove to be valuable in describing the behavior of the INS and GPS error states.

A *white noise* is a stationary random process with uniformly distributed power spectral density over all frequencies. A Guassian white sequence is referred to as a discrete time sequence of zero mean, normally distributed, and all variables are mutually uncorrelated with all other members of the sequence (Brown and Hwang, 1992).

The *random constant* model assumes a constant value for all variables of a single realization of the process. Therefore, this model is stationary but not ergodic. The random constant is represented by the following differential equation:

with zero expectation and $\sigma_{x_0}^2$ variance. The corresponding discrete process is given by:

$$\dot{x}(t) = 0 \qquad\qquad x(t_0) = x_0 \qquad\qquad (4.1)$$

$$x_{k+1} = x_k \qquad\qquad (4.2)$$

A *random walk* process models the output of an integrator of uncorrelated variables contaminated with random noise. If the random noise is normally distributed, the process in called a Wiener process or Brownian-motion process. The following differential equation represents the process:

$$\dot{x}(t) = w(t) \tag{4.3}$$

where w is a zero-mean white noise process. The corresponding discrete form of the process is given as follows:

$$x_{k+1} = x_k + w_k \tag{4.4}$$

Assuming that the gyro's measurements (incremental angular rates) are contaminated with white noise, then the orientation errors could each be modeled as a random walk.

A Gauss-Markov process often describes a correlated signal. The continuous first order of this family is associated with the following differential equation

The equivalent discrete process is represented by the following difference

$$\dot{x}(t) + \beta_1 x(t) = w(t) \tag{4.5}$$

equation,

$$x_{k+1} = e^{-\beta_1 \Delta t} x_k + w_k \tag{4.6}$$

which is approximated by the following difference equation:

$$x_{k+1} \approx (1 - \beta_1 \Delta t) x_k + w_k \tag{4.7}$$

The value of the variable at time t_{k+1} depends only on the value one step in the past and on the input variable (Markovian process), and this could be represented mathematically as follows:

$$f\left[x(t_k) \,|\, x(t_{k-1}), \ldots, x(t_1)\right] = f\left[x(t_k) \,|\, x(t_{k-1})\right] \tag{4.8}$$

where f is the probability distribution function of the process $x(t_k)$.

The inverse of the parameter β_1 in equation (4.5) indicates the degree of correlation and is often called the correlation distance or time. The variance of the white noise generating this process equals $2\beta_1 \sigma^2$, where σ^2 is the variance of the variable x.

In this study, the gravity disturbance vector is augmented to the Kalman filter error states and modeled as a first order Gauss-Markov process with correlation distance of about 37 km. Many mathematical and statistical models are used in the literature to

describe the Earth's gravity field. More discussion on these models is documented in Appendix A. More about the error states estimation process and the system's stochastic modeling comes in the subsequent sections.

4.3 Dynamic Error Modeling and Estimation

The Kalman filter is well suited for dynamic state space estimation. In addition to its flexibility in accommodating a variety of noisy measurements, The Kalman formulation allows stochastic modeling of the system's random processes. Selecting the appropriate stochastic models for the random processes is vital to the success of the Kalman estimation. The fundamental equations of the Kalman solution are given in Chapter 3.6. In this section, state vector augmentation and stochastic modeling are discussed. In addition, a brief discussion on practical limitations of the Kalman solution is given, followed by a discussion on the dynamic equations and integration schemes.

The observability of the Kalman states is a factor for a convergent solution. The filter must have enough independent information through the measurement system to estimate correctly all state variables. The Kalman estimation, however, is designed to yield the best possible results under the available information. Introducing the right measurements to observe a particular set of variables could have a substantial effect on the estimability of these variables. This fact is shown clearly in the results of this work.

Now, following the perturbation rules (distinguish between angular and translatory perturbations) of the INS navigation equations, choices of error variables, and coordinate system to coordinatize the equations, different formulation of state equations might be reached. For more on INS error modeling and representation see Arshal, (1987), Goshen-Meskin, (1992), and Jekeli, (1996). A compact state equation takes the following form:

$$
\begin{pmatrix} \dot{x}_1 \\ \dot{x}_2 \\ \dot{x}_3 \\ \dot{x}_4 \\ \dot{x}_5 \\ \dot{x}_6 \end{pmatrix} = \begin{pmatrix} F_{11} & F_{12} & F_{13} & F_{14} & 0 & 0 \\ 0 & F_{22} & 0 & 0 & 0 & 0 \\ 0 & 0 & 0 & 0 & 0 & 0 \\ 0 & 0 & 0 & F_{44} & 0 & 0 \\ 0 & 0 & 0 & 0 & F_{55} & 0 \\ 0 & 0 & 0 & 0 & 0 & F_{66} \end{pmatrix} \begin{pmatrix} x_1 \\ x_2 \\ x_3 \\ x_4 \\ x_5 \\ x_6 \end{pmatrix} + G \begin{pmatrix} w_1 \\ w_2 \\ w_3 \\ w_4 \\ w_5 \\ w_6 \end{pmatrix} \tag{4.9}
$$

where x_1, x_2, x_3, x_4, x_5 and x_6 are the error states of the navigation solution, accelerometers, gyroscopes, gravity, ionospheric GPS, and correlated photogrammetric orientation respectively. These error states include the following:

$$x_1 = \begin{pmatrix} \delta r_N & \delta r_E & \delta r_D & \delta v_N & \delta v_E & \delta v_D & \psi_N & \psi_E & \psi_D \end{pmatrix}^T$$

$$x_2 = \begin{pmatrix} b_{ax} & b_{ay} & b_{ay} & S_{ax} & S_{ay} & S_{az} \end{pmatrix}^T$$

$$x_3 = \begin{pmatrix} b_{gx} & b_{gy} & b_{gz} \end{pmatrix}^T$$

$$x_4 = \begin{pmatrix} \delta g_N & \delta g_E & \delta g_D \end{pmatrix}^T \qquad (4.10)$$

$$x_5 = \begin{pmatrix} d1_{ION} & d2_{ION} & . & . & . & d8_{ION} \end{pmatrix}^T$$

$$x_6 = \begin{pmatrix} C_{cN} & C_{cE} & C_{cD} \end{pmatrix}^T$$

where δr and δv are the error states in position and velocity respectively. ψ has the three attitude errors. b_a, S_a, and b_g are the accelerometer bias, scale, and gyro drift error states respectively. x_4 contains the three components of the gravity disturbance vector. x_6 consists of three components of photogrammetric orientation correlated noise. x_5 has the GPS double difference ionospheric error terms. It is important to notice here that DD ambiguity error terms are excluded from the error dynamics equation as a pre-processing was done to the raw GPS data to resolve the DD ambiguities. The subscripts N, E, and D refer to the three components of the local level coordinate, North, East and Down, respectively. The submatrices of the dynamics matrix F are provided in detail in Appendix B. w_i are zero-mean Gaussian noise vectors. The corresponding discrete form of Equation (4.9), assuming time interval $\Delta t = t_k - t_{k-1}$, is given as

$$x_x = \Phi_{k,k-1} x_{k-1} + G_{k,k-1} w_{k-1} \qquad (4.11)$$

$$\Phi_{k,k-1} = I + F(t_{k-1})\Delta t + \frac{1}{2!} F(t_{k-1})\Delta t^2 + H.O.T. \qquad (4.12)$$

with

$$w_k = \int_{k-1}^{k} w(t)dt \qquad (4.13)$$

$$E\{w_k w_k^T\} = q\Delta t \; ; \; \text{q is the PSD of the white noise.} \qquad (4.14)$$

$G_{k,k-1}$ is a formulation of noise weight matrix containing the necessary transformations. This matrix is also provided in Appendix B.

As was stated in the preceding chapter, proper modeling of GPS and INS errors is crucial for the optimality of Kalman filter estimation. However, truth models could be very complex and expensive to implement. Therefore, a suboptimal solution is mostly accepted as more practical and worthy the sacrifice of the highest possible accuracy. In addition, the accumulated experience through the years of investigating the INS error behavior as time progresses, from both the scientific and commercial communities, yields more accurate description of the INS error sources. Based on recommendations from the

INS manufacturer (Litton Systems, Inc.) about the INS error states, and from different trials and simulation during the development process of the GPS/INS integration software, twenty-one error states were used. In addition, eight states for GPS errors were augmented to the system as shown in equations (4.9) and (4.10). To accommodate for the independent source of photogrammetric orientation in the estimation process, another three error states were also added to account for the camera correlated noise. Accelerometer biases are modeled as random constants. Each time the INS is turned on, new values of accelerometer biases are produced and presumably remain constant for all time of operation. Assuming that gyro raw measurements (incremental angular rates) are driven by white noise, a proper modeling of gyro drifts would be random walk stochastic process. Random walk models an output of integrator on uncorrelated measurements. For the GPS error states, an extensive study was done at the Center for Mapping (CFM) at the Ohio State University to examine the behavior of ionospheric effect of GPS signal. It was found that first order Gauss-Markov process is appropriate to model the double difference ionospheric delay. However, random walk model is used as it fits quite well the double difference ionospheric estimates obtained from ionosphere-only linear combinations (Grejner-Brzezinska, 1998). The gravity anomaly and deflections are modeled as first-order Gauss-Markov processes. It should be noticed, however, that such a model of the gravity disturbance is contrived merely to illustrate the use of external orientation on the estimation process of the horizontal components of gravity vector. The actual gravity components are neither linear, nor finite-order as modeled in this study. The stochastic modeling of the anomalous gravity field has been investigated by many authors, and many analytical autocorrelation functions have been published in the literature to show the importance of properly modeling the anomalous gravity field in GPS/INS integration. More details on gravity field modeling can be found in Wang and Jekeli (1998), Jekeli (1991), Knickmeyer (1990), and Eissfeller (1989). Appendix A shows some of the analytical autocorrelation functions used in the literature to model the anomalous gravity field.

Camera correlated noise parameters are modeled as first-order Gauss-Markov processes as shown in Chapter 2; cross correlations, however, are neglected. Due to the spatial separation between the GPS antenna and the INS center, a lever arm error vector could be added to the Kalman states. Precise knowledge of this separation eliminates the necessity to add this vector. Similarly, three error states could also be added for the lever arm between the exposure station of the camera and the INS center. The spatial separation is assumed precisely known during the simulation process. Table 4.1 summarizes the number of the error states, their initial standard deviation, and the system states' statistical models. The initial values of the error states' standard deviation are rough estimates and expected to be improved as the mission progresses.

4.4 GPS/INS Integration
An extensive development of GPS/INS integration and development has been done in recent years in both ground and airborne applications (see Napier (1988), Eissfeller and Spietz (1989), and Sohne and Groten (1994)). On one hand, the INS is supported by the GPS positions with an update of mostly 1 Hz. On the other hand, the

INS is used to interpolate positions between the updates and helps in cycle slip detection and fixing. These features are particularly advantageous for high dynamic navigation when the aircraft frequently loses satellite signals during sharp turns and other maneuvers. It is important to note here that precise navigation requires gravitational corrections for the INS, especially if the GPS interruption lasts for long time. Numerical simulations on position errors of the INS due to unknown gravity components can be found in Jekeli (1997). In the sequel, different methods to integrate GPS with INS are briefly discussed, with some emphasis on GPS/INS gravity determination.

GPS and INS sensors exhibit complementary error behavior that makes their integration for navigation superior to either of the systems alone. However, in this study, the integration of GPS and INS is combined for the estimation of gravity, being a quantity that affects one system but not the other. Both accuracies of IMU components and GPS measurements were extensively investigated to determine if a combined system is capable of extracting the gravity vector signal. A primary conclusion of these studies states that GPS errors limit the high frequency recovery of the components of gravity vector and that the drift of the gyros is the most significant hindrance to recover the long-wavelength parts of the horizontal components. See, for example, Huddle (1978); Schwarz et al. (1992); Jekeli (1994); and Mangold (1995).

There are different approaches to combine GPS and INS sensors which are used traditionally for positioning applications. Similarly some of these alternative approaches could also be adapted to the gravity vector estimation. Some approaches are more complex than others (Greenspan, 1994). For the positioning applications, the simplest approach is to reset the INS position and velocity to the GPS position and velocity. As mentioned by Cox, (1980), this uncoupled procedure suffers from relatively large errors made by the unaided GPS filter, especially in the presence of severe dynamical situations. A substantially better approach is called loose, cascaded, or decentralized integration. In this integration, two separate filtering schemes are used to derive both GPS and INS navigation parameters. The GPS derived position and/or velocity is used as measurements in the INS filter. An optimum solution could be achieved by a centralized or tight integration approach. This approach combines both sensors at their raw measurement level in a single centralized Kalman filter, rather than cascading two filters. Among other advantages, this approach is optimum in the sense that it uses all available GPS measurements no matter if these measurements are enough to provide GPS solution or not. Navigation capability would be lost in case INS fails, however. Other synergism schemes were also used in the past years. Aided GPS, for instance, uses GPS as its primary navigation system with INS as an auxiliary only. When GPS signal is jammed or interrupted, the INS takes over. The INS gives the navigation solution in the period of GPS outages only, but it also helps in acquiring the GPS signal.

| Error Type, Stochastic Models	# of States	One Sigma (1σ) (initial)	Model Parameters Process σ, Beta, & Noise PSD
* Navigation Parameters:			
Position errors	3	10.0 m	
Velocity errors	3	1.0 m/s	
Attitude errors	2	0.015 deg	
Heading errors	1	0.05 deg	
* Accelerometers:			
Bias errors (random constant)	3		20 mgal
or (random walk)			$\sqrt{2}*5$ mgal/Hz$^{1/2}$
Scale errors (random walk)	3		40 ppm , $\sqrt{2}*5$ ppm/ hr $^{1/2}$
* Gyroscopes:			
Drift errors (random walk)	3		0.01 deg/hr , 0.001 deg/ hr $^{1/2}$
* Gravity:			
Gravity Deflections (1st order G-M)	2		25 mgal , $\beta^{-1}=3.704*10^{4}$ m $\sqrt{2\beta v_h}*25$ mgal/ Hz$^{1/2}$
Gravity Anomaly (1st order G-M)	1		30 mgal $\beta^{-1}=3.704*10^{4}$ m
* GPS:			
Ionospheric delay (random walk)	8		2.0 cm 1.0 mm/Hz$^{1/2}$
* Camera:			
Correlated noise	3		
Pitch (1st order G-M)			$2.98*10^{-4}$ deg/Hz$^{1/2}$, $\beta^{-1}=150$ sec
Roll (1st order G-M)			$2.77*10^{-4}$ deg/Hz$^{1/2}$, $\beta^{-1}=125$ sec
Heading (1st order G-M)			$1.59*10^{-4}$ deg/Hz$^{1/2}$, $\beta^{-1}=130$ sec

1st order G-M: 1st order Gauss-Markov process

Table 4.1: Kalman filter states, models, initial conditions, and system noise.

Figure 4.1 shows the architecture of the semi-tightly coupled GPS/INS system that continuously provides precise inertial navigation parameters from inertial solution and IMU sensor calibration. The term "semi-tightly" is describing the process, rather than "tightly" as appeared in the reference, because two different computation modules are used for GPS and INS which are combined together in one filter. The IMU error estimates are fed back to update the IMU measurements and to correct the inertial solution. This integration supports On-The-Fly (OTF) ambiguity resolution and cycle slip fixing based on quality checks of GPS data, ionospheric error modeling, and positioning information from integration. The INS prediction helps in resolving new integer ambiguities by narrowing their search space.

A similar integration scheme was assumed for the estimation of gravity vector from integrating GPS/INS with photogrammetric orientations. The integration scheme is described is the next section. It is important to notice, however, that the availability of photogrammetric data is not as frequent as GPS data, and therefore, a sequential scheme of measurement updates is used. More detailed description on the process with schematic diagram is given in Chapter 5.

Airborne Data Collection
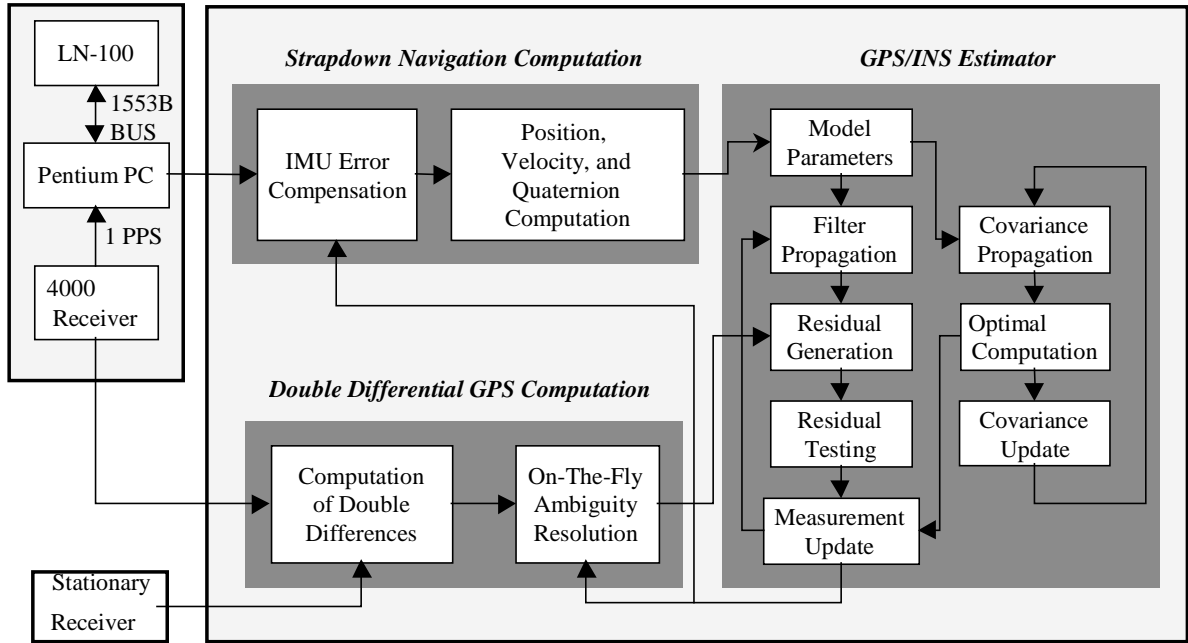
Ground Data Collection

Figure 4.1: Semi-tightly coupled GPS/INS system (Da, 1997).

4.5 Loose Photogrammetric Integration with GPS/INS

The exterior orientation determines the location and orientation of a photograph relative to the ground coordinate system. Based on collinearity transformation model (equation 2.30), the exterior orientation of all photographs and ground coordinates of all tie points are computed simultaneously. The bundle block adjustment model has many advantages over other photogrammetric modeling; it could be extended to incorporate external information. In addition, calibration parameters of the camera could be part of the adjustment solution. However, this modeling usually requires intensive computing capability. The high accuracy orientation parameters derived from photogrammetric solution directly relate to the geometric structure of the observations. Each measured point must appear in at least two images. The bundle solution returns the best fit of points in different images to their corresponding points on the ground.

The so-called loose integration is one approach selected for this research to integrate derived camera orientation parameters with GPS/INS system. A schematic diagram for the loose integration process is shown in Figure 5.7, page 113.

It is appropriate to pause here and reflect on the correlation in the measurement noise. The measurements in this study are a sequence of photogrammetric orientations obtained from a source completely independent of the GPS/INS system. These measurements are available only at the epochs of image acquisition. As indicated by Brown and Hwang, 1992, if external fixes are available only on an occasional basis, it is reasonable to assume that their errors will be uncorrelated. Thus, v_k in the measurement model (equation 3.22) satisfies the necessary requirements, that is, it must be a white noise sequence. However, the orientation measurements used in this study are obtained, together with their covariance matrix, from a bundle solution. A correlation analysis on the simulated data has been discussed in the Chapter 2.

To accommodate the complexity arising from the non-whiteness of the measurement noise, which violates the assumption of the Kalman filter measurement model, one should model the correlated noise by augmenting the state vector with additional parameters to be estimated during the estimation process. The autocorrelation function, as shown previously in Chapter 2, fits approximately an exponential representation, which makes it appropriate to model these correlations by a first-order Gauss-Markov process. The exponential function was shown by equation (2.28), where β^{-1} is the correlation time, and the differential equation associated with this process was shown in equation (4.5). Both equations are repeated here for convenience.

$$C_v(\tau) = \sigma_{0\,v}^2 e^{-\beta_v |\tau|} \tag{4.15}$$

$$\dot{v}(t) + \beta_1 v(t) = w_v(t) \tag{4.16}$$

The time-wise correlated measurement noise necessitates a modification to the traditional measurement model of the Kalman filter estimation. As the measurement noise is now modeled into the dynamics equation, the covariance matrix of the measurements has values of zeros. The orientation measurement model could be written as follows:

$$\begin{pmatrix} \psi_N \\ \psi_E \\ \psi_D \end{pmatrix}_k = \begin{bmatrix} 0_{(3x6)} & C_{l\,(3x3)}^n & 0_{(3x20)} & I_{(3x3)} \end{bmatrix} x_{k\,(32x1)} + \begin{bmatrix} 0_{(3x1)} \end{bmatrix} \tag{4.17}$$

$$R_k = [0_{(3x3)}] \tag{4.18}$$

where x_k is the vector of Kalman filter states. C_l^n is the transformation matrix from local level frame to the navigation frame. Note that the corresponding measurement noise vector and its covariance matrix in both equations (3.22) and (3.23) are now zero. The

observation vector consists of the three orientation error components, being the difference between photogrammetric orientation and GPS/INS orientation. The corresponding elements of the white noise covariance matrix, Q_k (equation 3.21) can be written as follows:

$$Q_{c_k} = \begin{pmatrix} \sigma_{0_N}^2 (1 - e^{-2\beta_N \Delta t}) & 0 & 0 \\ 0 & \sigma_{0_E}^2 (1 - e^{-2\beta_E \Delta t}) & 0 \\ 0 & 0 & \sigma_{0_D}^2 (1 - e^{-2\beta_D \Delta t}) \end{pmatrix} \qquad (4.19)$$

In addition to the above modeling, several other cases to process the data are considered in this study (more details in Chapter 5). One, in particular, uses the full variance-covariance matrix at each update epoch, while in-between epochs correlations are ignored. In this case, v_k is again assumed to be white noise, R_k is the covariance matrix, and the states, x_6 are omitted. Also, the following technique is used to transform the photogrammetric observation (solution) vector at each measurement update epoch into one where the observations are uncorrelated and have equal variance. Consider the Gauss-Markov model discussed before in Chapter 3 (Equations (3.22) and (3.23)). Using Choleskey decomposition, the weight matrix P could be decomposed as follows:

$$P = GG^T \qquad (4.20)$$

The upper triangular matrix G^T can be used to transform the observation vector in Equation (4.22) to a new uncorrelated one. By utilizing the law of error propagation, the transformed observation vector and its covariance matrix would be of the following:

$$G^T z = G^T H x + G^T v \qquad (4.21)$$

$$D(G^T z) = D(G^T v) = \sigma_0^2 I \qquad (4.22)$$

The transformation of the observation equation (3.22) into equation (4.21) means that each observation equation in multiplied by the square root of the weight of its observation. This process is called homogenization (Koch, 1987).

The GPS measurement model uses double difference (DD) carrier phase observations (equation 2.5). Depends on baseline length, some of the DD errors could have a significant effect on positioning accuracy. In particular, the ionospheric effect is modeled as random walk and augmented to the dynamics equation of the Kalman filter as mentioned earlier. The differential equation for the random walk process and the corresponding discrete form are given by equations (4.3) and (4.4), respectively. The differential effect of multipath should not exceed 1-2 cm for horizontal components and could be larger for the vertical component (Shi and Cannon, 1995). From GPS preprocessing, the DD residuals show a level of 1-2 cm accuracy in all three directions; therefore, multipath is not modeled (Da, 1997). On the other hand, real-time GPS/INS

positioning system requires a reliable On-The-Fly (OTF) ambiguity resolution module. For this study, however, real-time is not as critical and post processing is applied. Therefore, pre-processing was performed to ensure quality of GPS data and resolve integer ambiguities.

The GPS observation vector applied to the measurement update consists of the DD error components, being the difference between the observed GPS DD carrier phase and the computed DD using INS navigation solution. The GPS measurement model could be written as follows:

$$\left(GPSDD - INSDD\right)_{k_{(mx1)}} = \left[H_{(mx3)} \quad 0_{(mx18)} \quad C^n_{e\ (mxm)} \quad 0_{(mx3)}\right] \mathrm{x}_k + v_{k_{(mx1)}} \qquad (4.23)$$

where H contains the partial derivatives of GPS observations with respect to the position parameters transformed to navigation frame. C^n_e is the transformation matrix from Earth-fixed-Earth-centered frame (the e-frame) to navigation frame and is given by:

$$C^n_e = \begin{pmatrix} -\sin\varphi\cos\lambda & -\sin\varphi\sin\lambda & \cos\varphi \\ -\sin\lambda & \cos\lambda & 0 \\ -\cos\phi\cos\lambda & -\cos\phi\sin\lambda & -\sin\varphi \end{pmatrix} \qquad (4.24)$$

where φ and λ are the geodetic latitude and longitude.

It should be noted here that, even though the raw GPS carrier phases are assumed uncorrelated, the linear DD operator transforms them into correlated set of measurements. Therefore, the homogenization technique is applied to decorrelate (whiten) the GPS DDs before using them in the Kalman filter measurement update module.

4.6 Tight Photogrammetric Integration with GPS/INS

The photogrammetric tight integration would combine directly the image measurements with GPS/INS in the dynamic process of Kalman filter estimation where the photogrammetric observation of each image could be used as feedback for the GPS/INS system calibration. In this case, the ground control could be added directly into the filter in the form of point constraints through the collinearity equations. Subsequently, pass points constraints from image measurements might be added directly as they become available. On the other hand, the bundle block adjustment program enforces the bundle of light rays of common points to intersect, as close as possible, at their corresponding points at the ground. In other words, the solution provides the best possible overall fit to rebuild the geometric structure of the points at the time of exposure. This important property is lost during the tight integration process where every image would be processed separately and sequentially.

The flexibility of the bundle solution to extend the mathematical model to incorporate additional lens and film parameters adds complexity to the tightly integrated process. In addition, the bundle solution solves for the unknown tie points coordinates in one step. Taking care of the unknown tie points adds another level of complexity to the tightly integrated process that requires special attention. For these reasons, a tight integration is not considered; and this study utilizes the bundle solution to the orientation angles together with GPS/INS to investigate gravity vector determination in a post-processing uncoupled mode.

CHAPTER 5

TESTING AND RESULTS

5.1 Introduction and AIMS Initiative

The Center for Mapping (CFM) at The Ohio State University has been developing a fully digital, real time data acquisition system for large-scale mapping and other precise positioning applications (Bossler, 1996). This system, known as the Airborne Integrated Mapping System (AIMS), incorporates both GPS/INS positioning and digital imaging technologies. In addition to photogrammetric aerial triangulation with no ground control necessary (at least in theory), a potential for many other military and commercial applications is emerging, e.g., transportation infrastructure, utility lines, natural resource management, and emergency response deployment. One of the main objectives of AIMS is to obtain 4-7 centimeter level of relative positioning accuracy and better than 10 arcseconds orientation accuracy in real time (Grejner-Brzezinska and Wang, 1998). Although the gravity vector estimation was not a goal for AIMS, its sensors are capable of extracting gravity information along the flight trajectory in post-processing mode.

In photogrammetric aerotriangulation, GPS/INS was viewed as an external help to the camera, which pays back in less ground control needed. The GPS or GPS/INS camera exposure station position is obtained to the required accuracy for high precision mapping. The camera orientation derived from ground control and GPS exposure station position is still superior to the GPS/INS orientation. The GPS, INS, and camera could be utilized for different navigation and mapping applications. They also have the potential to collect information about the physical variations of the gravity field.

The results shown in this Chapter are an attempt to make use of mapping missions, with navigation and photogrammetric sensors on board, to compile gravity information. The superior photogrammetric orientation parameters are used to improve the estimation process of the horizontal components of gravity vector.

The system hardware and its specification are described in section 5.2. The real GPS/INS data and the description of the photogrammetric simulation process are shown in section 5.3. Finally, the data processing and test results are given in sections 5.4 and 5.5 respectively.

5.2 Description of the Inertial and GPS Systems

The Litton LN-100 Zero-lock™ Laser Gyro (ZLG™) and A-4 accelerometer triad is a medium-to-high accuracy strapdown INS that provides time tagged attitude angles (roll, pitch, and azimuth), position, velocity, and accelerations. The LN-100 is rated at about 1.0 km/hr circular error probable (CEP), using self-contained gyrocompass alignment (4-minute) and a strapdown wander azimuth navigation equation system mechanization. In contrast to the mechanical dithering of the conventional Ring Laser Gyros (RLG), the ZLG has no moving parts and it uses optical biasing to avoid the lock-in phenomenon. In spite of the resulting performance improvement, the gyro white noise (expressed as

random walk in angle) is still one of the major contributors to the navigation and alignment errors. Litton's A-4 accelerometer is a high performance, inertial-grade accelerometer packaged in a triad configuration. Performance characteristics of the ZLG and A-4 accelerometer are shown in Table 5.1 (Litton, private communication). The accelerometer misalignment is a primary factor limiting the estimability of the horizontal components of gravity vector. As mentioned before in Chapter 1, one arcsecond of leveling error would generate five mgals error in the horizontal gravity components. Any future improvement to the inertial systems to minimize the accelerometer's misalignment would be of great help to gravity vector estimation. The INS data acquisition system is built on a Pentium PC system and based on two specific hardware boards: the GLD PC/S 1553B interface card from Digital Technologies, Inc., and a CIO-DIO 24/CTR three-channel timer board from Computer Boards, Inc. The timer board implements a real-time clock providing one microsecond timing resolution and is synchronized to GPS time. Using the GPS serial line, the microsecond count is updated by the 1PPS GPS signal (Da, 1997). The INS accompanying software provides modules to start the INS initialization process and switches to navigation mode when the initialization is done. Different modules can be utilized to customize the INS output messages. It should be mentioned here that the INS characteristics shown in Table 5.1 are not the ones used in the data processing of this study. Table 4.1, on the other hand, together with Chapter 4.3 have detailed description and rational on data models used to process the data.

Gyro Performance (1 sigma)	
Bias Repeatability	**0.003 deg/hr**
Scale Factor Stability	**0.2 ppm**
Random Walk	$\mathbf{< 0.001\ deg/\sqrt{hr}}$
Misalignment	**1.5 arcsec**
Accelerometer Performance (1 sigma)	
Bias Repeatability	**20 mgal**
Scale Factor	**40 ppm**
Misalignment	**2 arcsec**
White Noise	$\mathbf{5\ mgal/\sqrt{Hz}}$

Table 5.1: Summary of Litton LN-100 Characteristics.

The Trimble 4000 SSI geodetic GPS receiver is designed for high-precision navigation applications. This receiver automatically acquires and simultaneously tracks up to nine GPS satellites; it precisely measures carrier and code phases (C/A and P, when available) and stores them in an internal, battery backed-up memory. The Trimble 4000 SSI receiver utilizes cross-correlation measurements during periods of Anti-Spoof (AS) encryption. This enables the recovery of full-cycle L1 and L2 phase signals and dual-frequency code tracking at all times (Trimble Navigation Limited, 1992). The collected

binary format GPS data is transferred from the GPS receiver to a PC by running the manufacturer provided software TRIM4000.

5.3 Test Data

In July 1997, the CFM carried out a flight test over Oakland, California to evaluate the capability of the GPS/INS system to determine the camera exterior orientation parameters without ground control. The imaging system used for this test was Zeiss RMK TOP aerial camera provided by the CFM development partner on the AIMS project, the Hammon, Jensen, Wallen & Associates, Inc. (HJW). The system's capability to provide exterior orientation parameters was compared with superior and independent solution using many ground control points scattered at the test field. Only fifteen photographs were collected over the test area where about forty ground control points exist. The aerial photographs were processed on analytical plotter and the exterior orientations were computed using bundle adjustment program based on ground control points. In contrast to the process of photogrammetric acquisition, the GPS/INS data are collected along the total flight trajectory and not only over the test field. To utilize the GPS/INS data for this study, a photogrammetric data set is simulated along the flight trajectory and processed together with GPS/INS in this chapter to analyze the system's capability to recover the gravity signal. Figure 5.1 shows the three-dimensional flight trajectory, Figure 5.2 gives the planimetric projection of the flight, and Figure 5.3 shows the flight altitude. The actual photogrammetric data collected over the test field were not used because it was only collected over a small area where many ground controls exist. The area of the test field can be seen in Figure 5.2 where the aircraft trajectory is making loops around the test field.
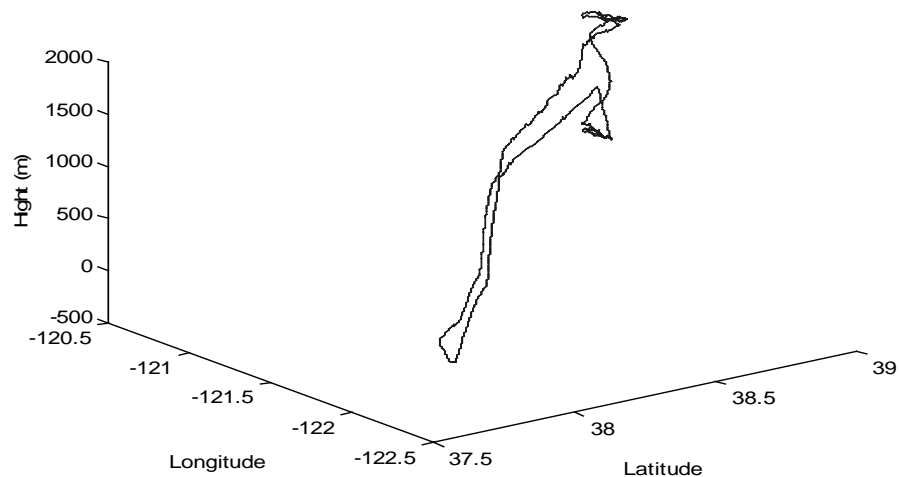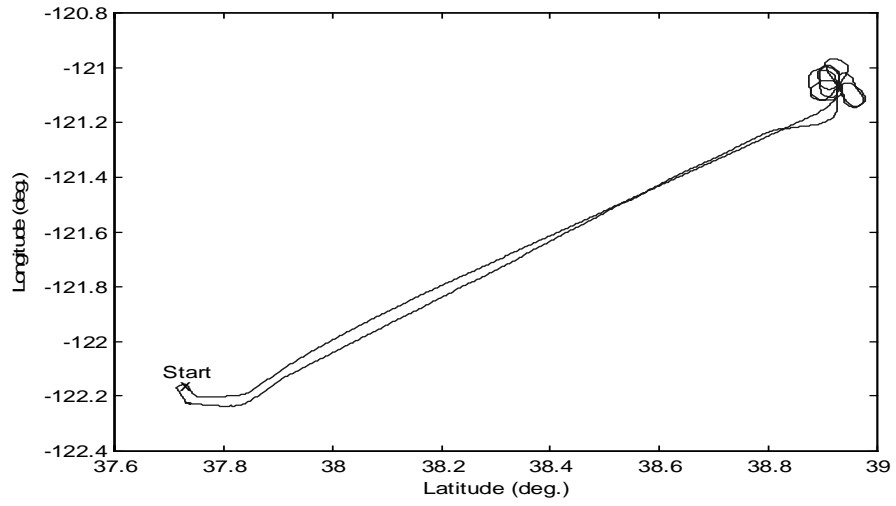

Figure 5.1: Flight trajectory

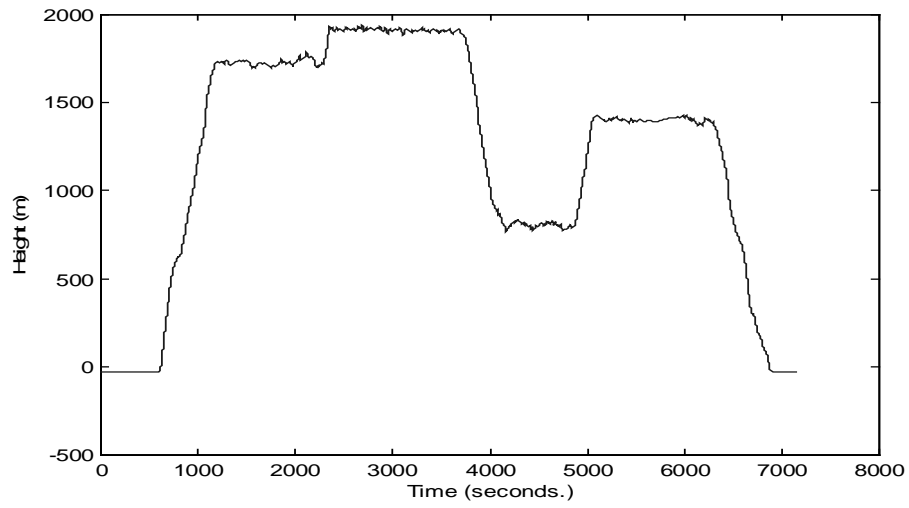Figure 5.2: Horizontal flight trajectory.

Figure 5.3: Flight Altitude

5.3.1 Photogrammetric Data Simulation

Based on real GPS/INS data collected during the Oakland flight test, the position, velocity, and orientation of the aircraft were used to simulate a set of 150 photographs along the forward flight trajectory. Normal angle frame camera with focal length of 152 mm was assumed. Using average flight altitude of 1800 m, 60% overlap, the frequency of acquiring images comes close to 11 seconds. A 10-seconds imaging interval is used.

Three different methods were used to simulate the 150 set of photographs. In the first method, six consecutive subsets of 25 photographs each were simulated. With each subset, only three ground control points with one centimeter level of accuracy ($1\sigma = \pm 1$ cm) were used in the first photograph (or first pair of photographs) to establish the absolute orientation between the image coordinate frame and the ground coordinate frame. The pass points are sufficient to keep up with the relative change in orientation of the sequence of collected images. At least five well-distributed conjugate pass points must be measured in each of the consecutive photographs to establish relative orientation. For more details on how to accomplish relative and absolute orientation, the reader is referred to Slama et al. (1994). The second method uses three consecutive subsets with 50 photographs each. Similar to the first method, three control points were also used to establish the absolute orientation ($1\sigma = \pm 1$ cm). The third method differs from the second by the number and the distribution of the ground control points, In addition to the three ground control at the beginning of the simulated sets, two additional ground control points are added at the last photograph. Each subset of the three methods was processed separately by the bundle adjustment program to solve for the orientation parameters.

The 150 photographs could be simulated in one step. However, processing all of them at once with the bundle adjustment program might lead to numerical instability as the number of unknowns gets very large. In addition, using only three control points in the first pair of photographs to resolve the orientation parameters of the whole strip result in much deteriorated accuracy of these parameters, especially towards the end of the trajectory.

The simulation program generates a Digital Elevation Model (DEM) around a central point of the area to be photographed. The DEM is created by using simple polynomial as a function of the point coordinates. The density of the DEM is specified by the user. Spatial separation of 400-500 m is used in this simulation. Depending on the orientation of the simulated photograph, the spatial separation generates between 10-20 points in each photograph. Following the collinearity principle, the DEM points are projected to the images to generate the image coordinate file. Including in the simulation program is a user-defined level of normally distributed random noise, generated to substitute for the measurement noise. The simulated image coordinates were contaminated by normally distributed random noise with $\sigma = 3$ micron (1 micron = 10^{-3} mm).

The Bundle adjustment with Self-Calibration program (BSC), as mentioned earlier in section 2.3.5, is used for simultaneous least squares solution to the unknown parameters. The unknown parameters are nine exterior and interior orientation

parameters for each image and the object space coordinates of the pass points. The observation vector consists of image coordinates of both pass and control points. The non-linear mathematical model that relates the observations with the unknowns was discussed with sufficient details in section 2.3.3. The orientation angles of the images together with their full variance-covariance matrix were extracted from the solution file. A complete description of the input files to the BSC is given in Appendix F.

Figures 5.4-6 show the standard deviation in arcseconds of the three angles errors as extracted from the bundle adjustment program. As the strip gets longer without additional ground control, the accuracy of the orientation deteriorates as clearly shown in the Figures 5.4 and 5.5. Furthermore, the heading level of accuracy is superior over both roll and pitch angles. This superiority is derived as heading angle is controlled by horizontal coordinates which are usually more accurate as compared to vertical coordinates. Figure 5.6 shows the standard deviation in arcseconds where 5 ground control points are used at the beginning and at the end of the simulated strip.

The photogrammetric simulation process has been done separately for both cases of 25 and 50 simulated subsets. It is important to notice here that different initial condition in ground control and their distribution yield different accuracies in orientation angles. In addition, as Figures 5.4 and 5.5 show, the edge effect makes the standard deviation of the angles in the first photograph slightly higher than the second one. The best standard deviation values resulted from this simulation are about 2.50, 2.50, and 0.93 arcseconds for roll, pitch, and heading respectively.
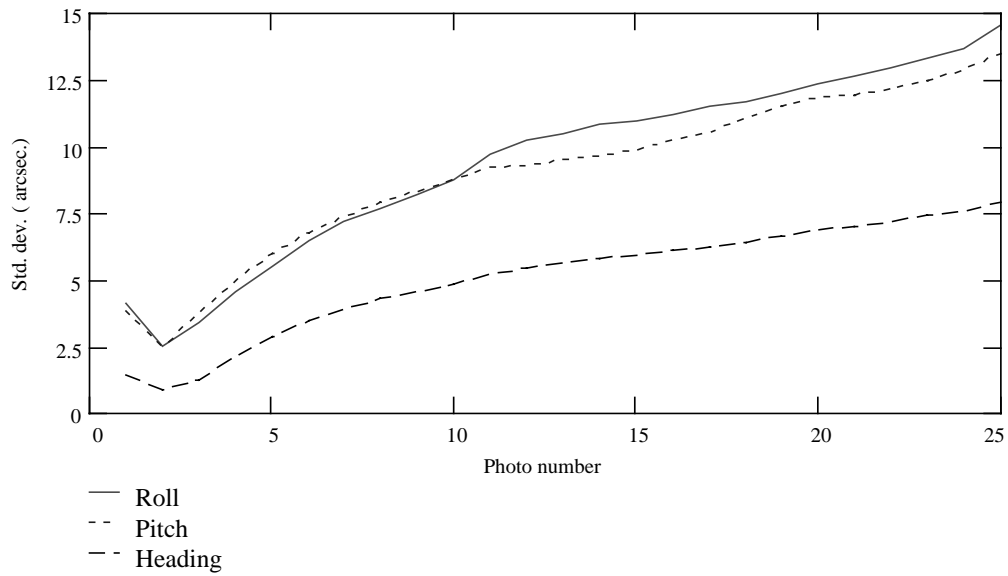
Figure 5.4: Standard deviation (arcseconds) of the orientation angles errors simulated 25 images with three ground control points.
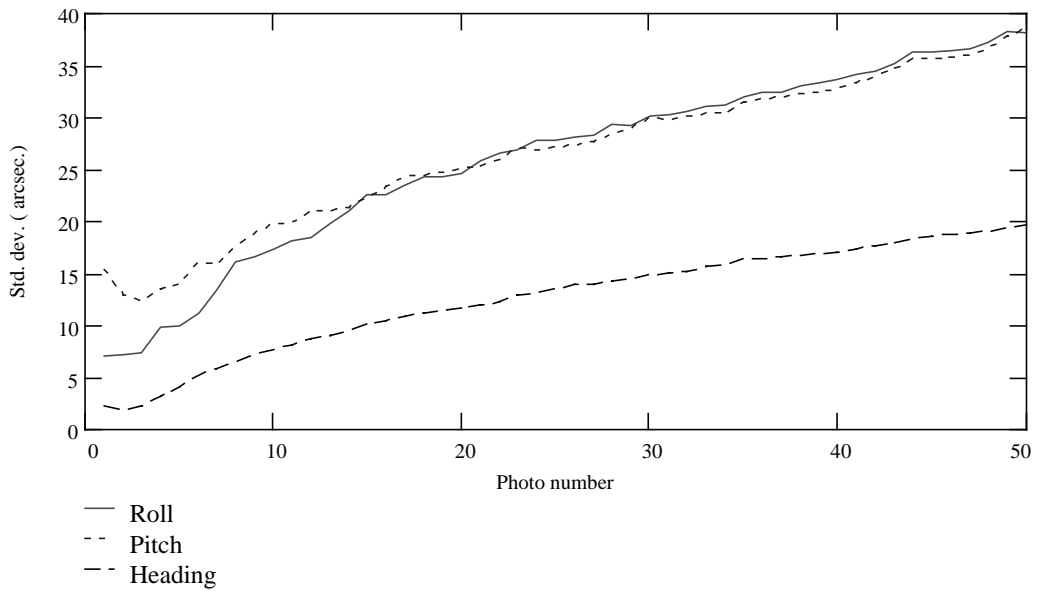

Figure 5.5: Standard deviation (arcseconds) of the orientation angles errors simulated 50 images with three ground control points.
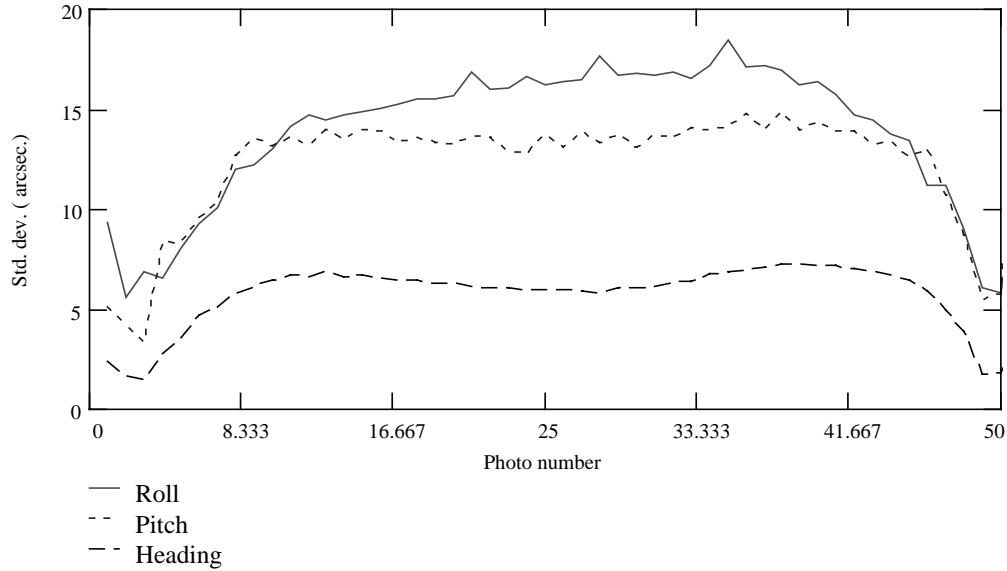
Figure 5.6: Standard deviation (arcseconds) of the orientation angles errors simulated 50 images with five ground control points.

5.4 Data Processing

The carrier phase double-difference observable (see equation 2.5) is used since it cancels, to the first order, common errors between the base and the rover stations. As the separation between the base receiver and the rover receiver, the double-difference ionospheric and tropospheric effects might have significant effects if not properly modeled. The double difference ionospheric delay is modeled and augmented in the Kalman filter state vector along with the other states (see equation 4.9). The double difference integer ambiguities are not modeled as a preprocessing has done to the GPS data where all ambiguities have been resolved.

Using the manufacturer provided software (TRIM4000), the collected GPS data was transferred to the computer and stored in the standard RINEX format. A GPS-alone solution was generated for preliminary assessments and testing purposes.

The LN-100 data acquisition software provided by the manufacturer has the functionality to start the initial alignment process. Upon completion, the software switches the INS from initial alignment mode to navigation mode. Also, the software allows the user to specify what type and frequency of data to be collected, and the place where the data is to be stored. In addition to the navigation solution, the LN-100 was also used to collect raw IMU measurements, namely, the linear and angular velocity rates. In contrast to using the navigation solution generated by the INS computational module, the raw IMU data was directly used in the semi-tightly integrated process and in the feedback calibration of the IMU sensors. The strapdown navigation module is divided into two separate submodules to process IMU raw data for attitude and navigation determination. The attitude sub-module computes the Direction Cosine Matrix (DCM) between the b-frame and the n-frame. The navigation submodule uses the DCM to

compute the equivalent specific force components in the n-frame. These components are integrated numerically to determine velocity and position.

The high-accuracy semi-tightly integrated GPS/INS software has been developed by the Center for Mapping for the AIMS project. The software uses C++, an object oriented programming language, that utilizes individual modules to enhance the efficiency and robustness of the software. During the development of the software, different forms of INS error models have been tried to reach the desired accuracy. Through private consultation with the CFM development partner and INS provider (Litton Systems, Inc.), a twenty-one state model was selected (Da, 1997). The error states include nine parameters for position, velocity, and orientation errors, six parameters for accelerometer biases and scale errors, three parameters for gyro drifts, and three parameters for gravity anomaly and deflections. The higher order GPS ionospheric terms were also added to the state model as shown previously in Chapter 4. Furthermore, as the camera data is integrated with GPS/INS data, three additional parameters were augmented to account for the camera correlated measurement noise. A detailed description on the stochastic modeling of the integrated system noise can be found in the previous chapter.

The GPS/INS and camera data are integrated loosely. The photogrammetric determination of the orientation angles and the corresponding GPS/INS determined angles are differenced to create the observation vector used by Kalman filter. As the photogrammetric orientation parameters become available, a measurement update to the Kalman filtering states is executed to further help gyro calibration. Due to the correlations in the orientation noise that violate one of the assumptions of the Kalman estimation, a modified measurement model is used. The measurement equations are given in Chapter 4. A schematic diagram for the GPS, INS, and photogrammetry integration process is shown in Figure 5.7.
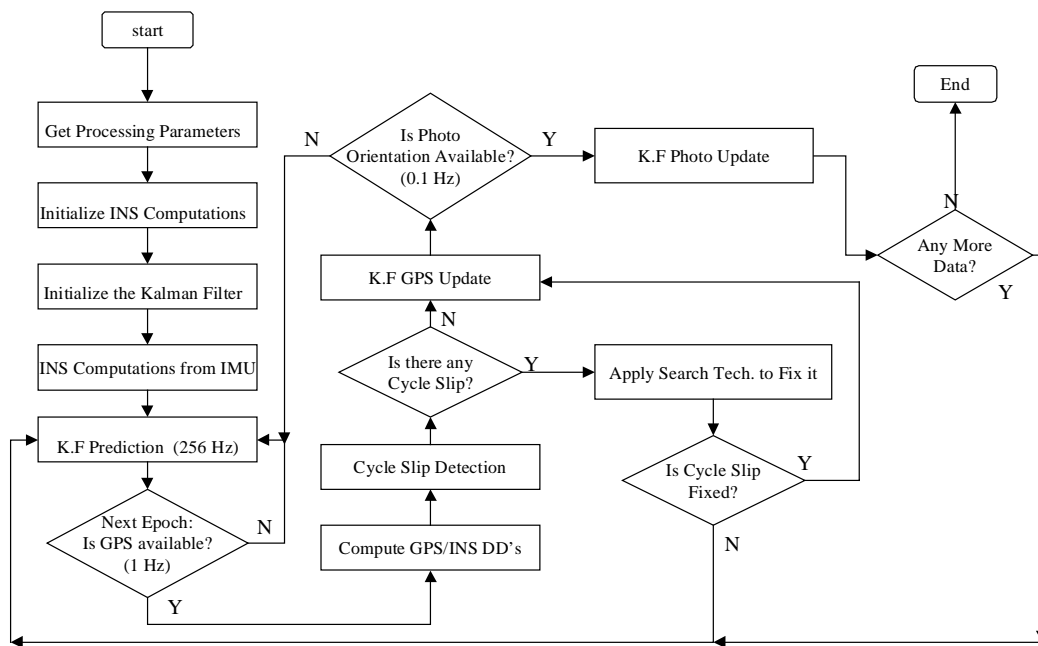
Figure 5.7: Schematic diagram for GPS/INS/Photo Integration process.

The INS/GPS/Camera data have been processed through the Kalman filter to determine the standard deviations of the estimated horizontal components of the gravity vector. Six different cases are considered with regard to the integrated photogrammetric orientations and their accuracy. These cases are described as follows:

1. ***Fixed variance***: This case considers only white noise in the photogrammetric orientation measurements. The standard deviations for the three orientation angles remain unchanged along the entire simulated 150-photo strip. Two different runs are considered for this case. In the first run, values representing the best standard deviations achieved from the photogrammetric simulations are used. These values are ±2.5, ±2.5, and ±0.93 arcseconds for roll, pith, and heading respectively. The results of this run will be labeled as "Fixed". In the second run, the standard deviations of the correlated measurement noise analysis are used (see Table 4.1 and Figures 2.7 and 2.8). These values are ±9.29, ±7.88, and ±4.62 arcseconds for roll, pith, and heading respectively. The results of this run will be labeled as "CorrFixed".

2. ***Diagonal variance***: This case also considers only white noise in the photogrammetric orientation measurements. However, the standard deviations for the three angles used are the ones generated by the simulation process. The outputs generated from this process will be labeled as "Diag25" and "Diag50" for both simulation cases as described in the previous section.

3. ***Full variance-covariance matrix***: This case considers the correlations at the epochs of orientation measurement updates. Between-epoch correlations, however, are ignored. Homogenization process is used to decorrelate the orientation before they are used in the Kalman filter (see Chapter 4 for more details). The results of this case are labeled as "Full25" and "Full50".

4. ***Colored noise***: This case considers between-epoch correlations in the orientation measurements. The new measurement model is described in Chapter 4. The results of this process are labeled as "Corr25", referring to the first set of simulated photographs. At-epoch correlations, however, are neglected.

5. ***Less colored noise***: This case is the same as case 4, but assumes less correlation in the orientation measurements. Half the correlation time (β^{-1}) is used in this case, and results are labeled as "CorrB".

6. ***Additional control points at end of strip***: This case is the same as case 2, but assumes additional ground control points at the end of the strip. The processing results are labeled as "Diag50BE".

The estimation results from all cases are compared with the results from "GPS/INS" alone process. Graphical representations of the data processes are presented in the next section.

5.5 Test Results

It was not the intention of the flight test designers to consider gravity estimation as part of the test goals. The flight test was done primarily to examine AIMS system and to access its achievable navigational accuracy. Nevertheless, this flight test has become very valuable in terms of evaluating GPS/INS airborne vector gravimetry and for suggesting directions to further investigations in this field. The flight contains four different segments that are crucial in the evaluation and interpretation of the test results. These segments give more insight to the characteristics and behavior of the sensors during different phases of the flight. These segments and their approximate time intervals are shown in Table 5.2.

The 150 photographs utilized in this study were simulated based on the GPS/INS data collected during the forward segment (Table 5.2) of the flight test. As mentioned in section 5.3.1, two different cases are considered. In the first case, three ground control points were introduced in each subset of twenty-five photographs to establish a connection with the ground coordinate frame. In the second case, three ground control points were introduced in each subset of fifty photographs. The following graphical results show the standard deviation of the orientation errors as well as the standard

Segment	Approximate Time Interval Total Time (seconds)		Description	Comments
Climbing (1)	1200	1200	From start until reaching flying altitude where image simulation starts.	-
Forward (2)	1500	2700	Continuing until reaching control area where actual image collection starts.	Used for this study
Looping (3)	2200	4900	Looping control area.	-
Backward (4)	2243	7143	Return to the base.	-

Table 5.2: Different segments of the flight test and their approximate times.

deviation of the horizontal components of gravity vector for the different cases mentioned in the previous section. For the sake of examining the change in the standard deviation values during the various segments of the flight, some results are plotted over the whole period of the flight, and not only during the period when photogrammetric measurements are introduced. Especially when the results between different cases are not significant, only the study segment of the flight is plotted to make the difference more clear.

For the *fixed variance* case, Figures 5.8-10 show the standard deviation, in arcseconds, of the orientation angles errors (East/West (E/W), North/South (N/S), and Heading), as determined by both GPS/INS and GPS/INS/Photogrammetry. The standard deviations of the N-S and E-W components of the gravity vector are shown in Figures 5.11 and 5.12 respectively.

In both E/W and N/S orientation errors, the GPS/INS integration results show smooth estimated precision of about four arcseconds over the whole period of the forward phase of the flight. The photogrammetric orientations are introduced to the system in ten seconds intervals. The precision of the photogrammetric measurements for the "Fixed" case represent the best results determined during the simulation process. The results achieved by this case reflect the great effect of accurate and independent orientation on GPS/INS orientation accuracy as well as on the horizontal gravity estimation. The standard deviation of the orientation parameters drops slightly below one arcsecond. The standard deviation of the horizontal components of gravity, on the other hand, drops from about 20 mgal to about 8.5 mgal.
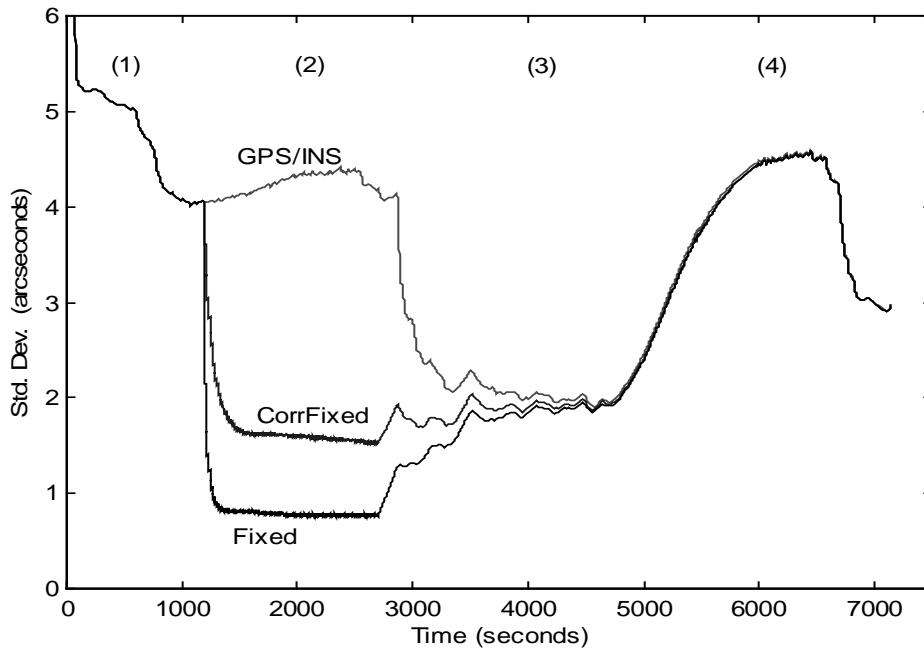
Figure 5.8: Standard deviation of the E/W orientation error (arcseconds) from GPS/INS, CorrFixed, and Fixed cases.

The "CorrFixed" case uses the same variances derived from the correlation analysis at all measurement update epochs (see Table 4.1). This case also assumes only white noise in the photogrammetric measurements. The results of this case show significant improvements over GPS/INS estimation for both orientation and gravity components (Figures 5.8-12).

The heading yields the most significant increase in the estimated precision as shown in Figure (5.10). The heading angle is controlled by horizontal points, which are usually determined more accurately in both GPS/INS and photogrammetry processing. At the end of the second segment of the flight where no more photogrammetric data are available, the estimated precision of all orientation states starts to converge, though not immediately, to the GPS/INS solution.

The third segment of the flight test is the looping period (see Table (5.2) and Figure (5.2)). Even though there were no photogrammetric data available to the system during this segment, the estimated precision has improved significantly in the three orientation angles to a level close to the same level of using photogrammetric orientation updates. This precision improvement also reflects on the estimation of gravity components as Figures (5.11) and (5.12) show. This segment of the flight test clearly demonstrates the effect of aircraft maneuvers on gyro calibration and orientation precision. The substantial change in the orientation of the aircraft yields similar effects as introducing new attitude observations to the system.

The direct relationship between the estimated precision of the orientation angles and the deflections of the vertical can be clearly seen in equations (3.16-17). This relationship is reflected in Figures (5.11-12). Observing the orientation parameters results in a clearly improved estimability of the vector gravity. For more details, see section 3.2.
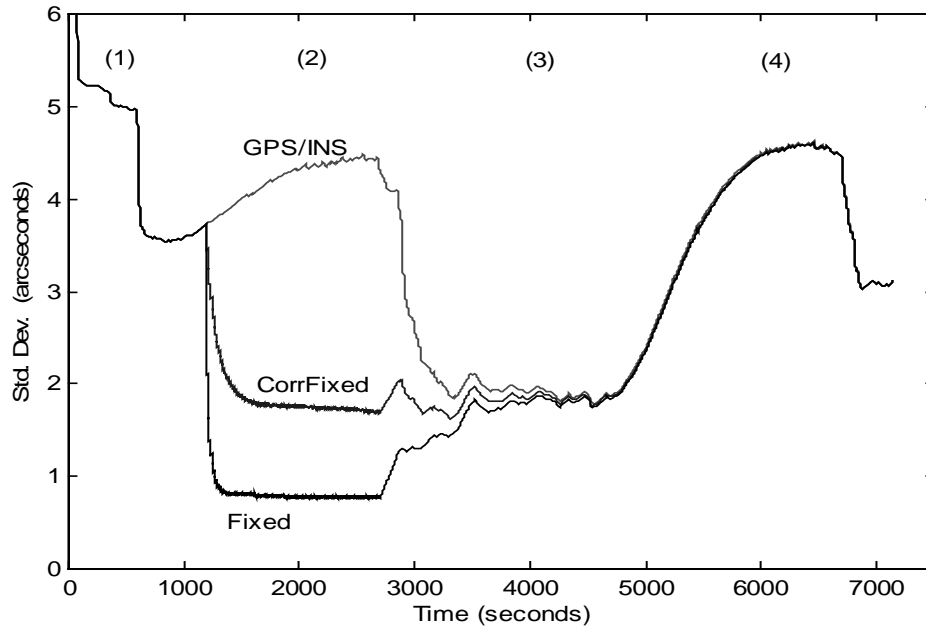

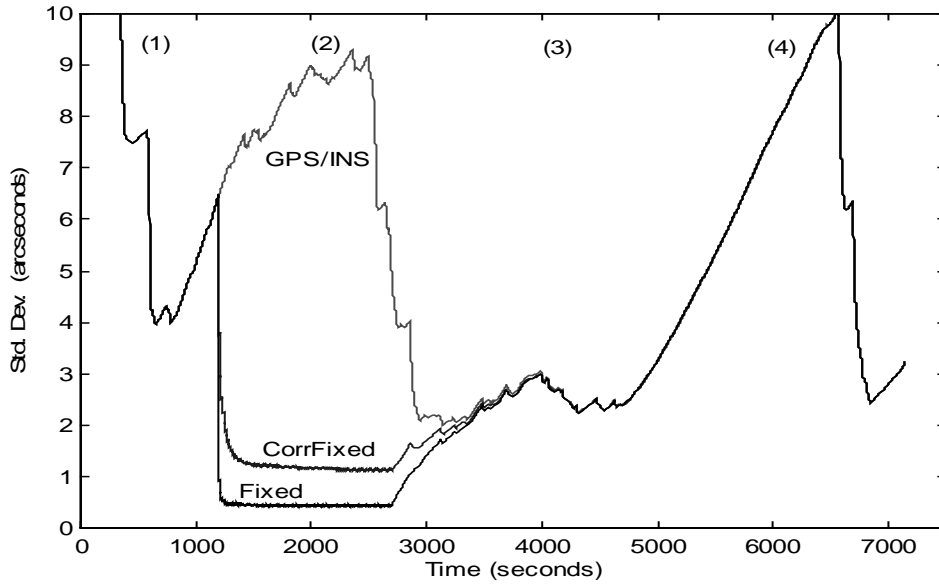Figure 5.9: Standard deviation of the N/S orientation error (arcseconds) from GPS/INS, CorrFixed, and Fixed cases.

Figure 5.10: Standard deviation of the heading angle error (arcseconds) from GPS/INS, CorrFixed, and Fixed cases.
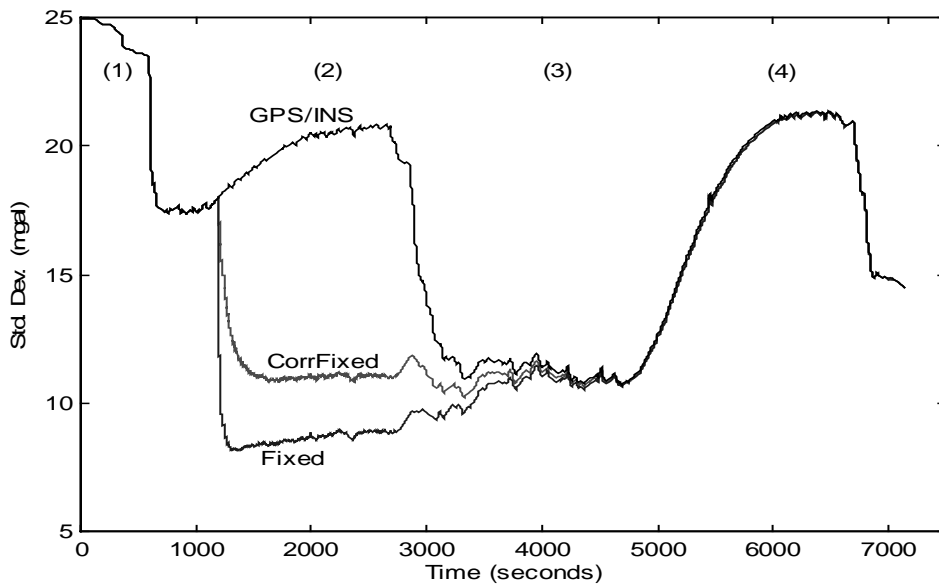
Figure 5.11: Standard deviation of the N-S component of gravity (mgal) from GPS/INS, CorrFixed, and Fixed cases.
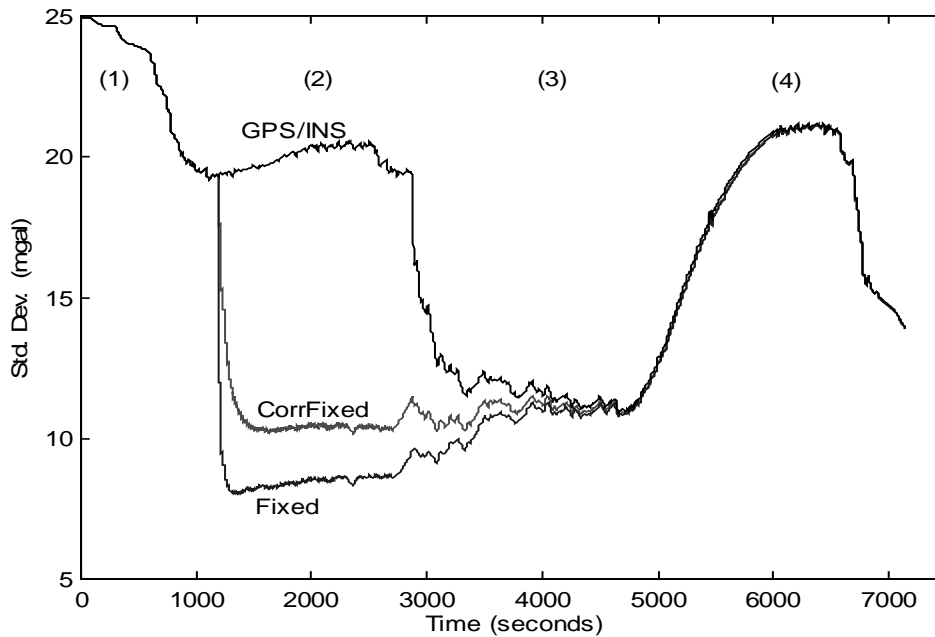
Figure 5.12: Standard deviation of the E-W component of gravity (mgal) from GPS/INS, CorrFixed, and Fixed cases.

The fourth and last segment of the flight test is the backward period. This segment begins as soon as the aircraft is headed back to the base (see Table (5.2) and Figure (5.2)). The backward segment demonstrates a significant decline in the estimated precision as little change in the aircraft orientation occurs. The effect of the aircraft orientation activity during the landing period transforms into an improved estimated precision as can be shown in the figures.

Figures 5.13-16 show the results of the ***Diagonal variance*** and ***Full variance-covariance matrix*** cases for the 50-photographs simulation (see Chapter 5.3.1). The precision of the photogrammetric measurements used for the "Diag50" and "Full50" cases was determined from the simulation process (see Figure 5.5). The horizontal orientation errors are shown, as they are more relevant to horizontal gravity estimation. In addition, only the second segment of the flight test is plotted to show more clearly the small difference between the results of both cases. The corresponding figures for the 25-photograph simulation case can be found in Appendix G.

The results achieved by processing these cases illustrate the effect of at-epoch measurement correlations on the estimated parameters. Considering at-epoch correlations results in a maximum deterioration in the orientation precision of about 0.25 arcsecond, and about one mgal in the gravity components. The degraded precision in the simulated N/S orientation of the second and third sets reflects clearly in the estimated errors of both N/S orientation (Figure 5.14) and N-S gravity component estimation (Figure 5.15).
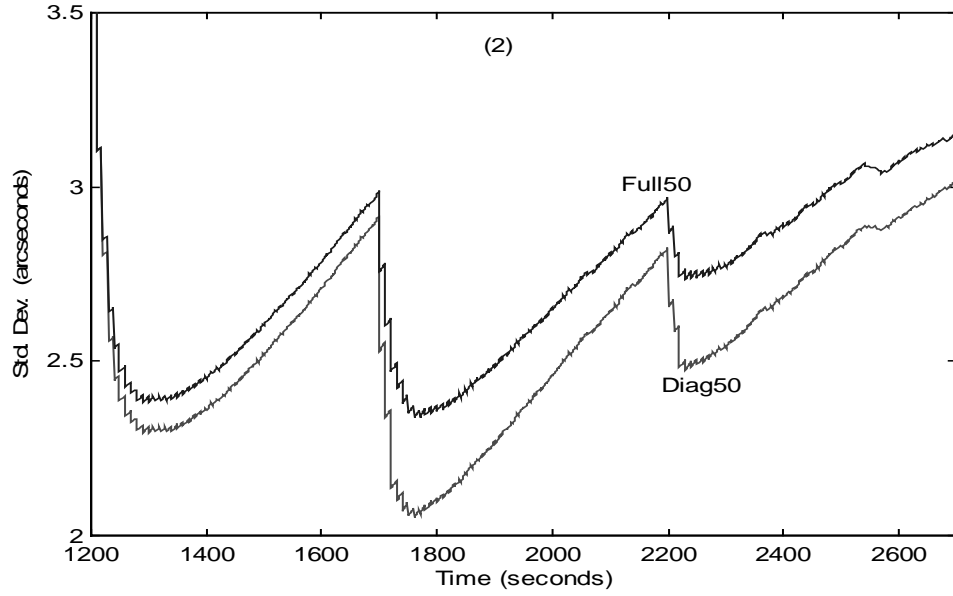
Figure 5.13: Standard deviation of the E/W orientation error (arcseconds) from Diag50 and Full50 cases.
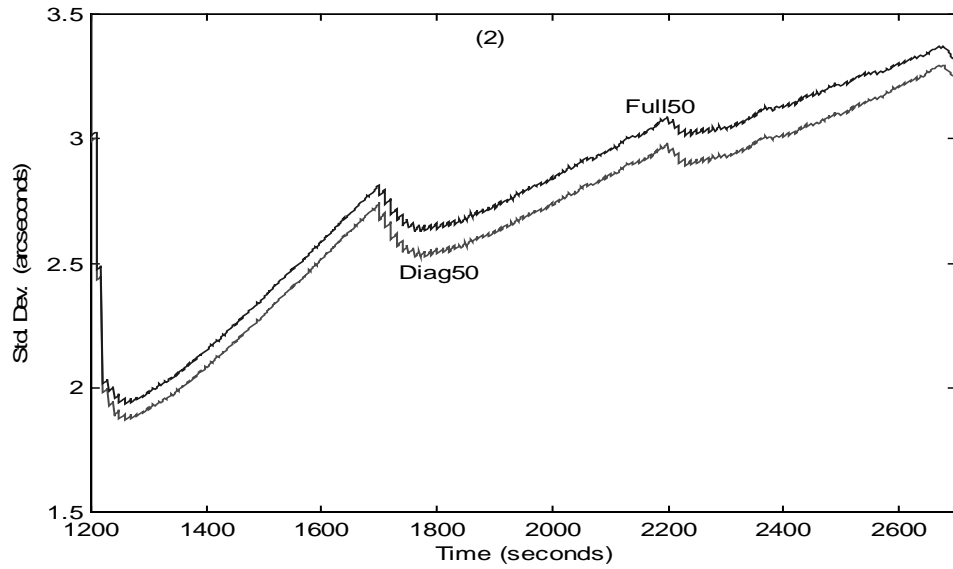
Figure 5.14: Standard deviation of the N/S orientation error (arcseconds) from Diag50 and Full50 cases.
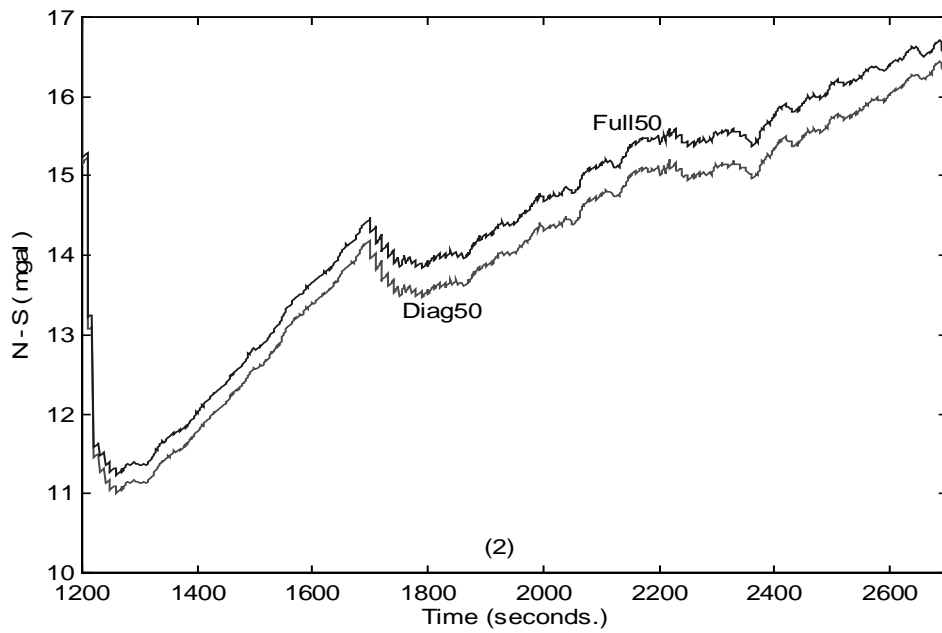

Figure 5.15: Standard deviation of the N-S component of gravity (mgal) from Diag50 and Full50 cases.
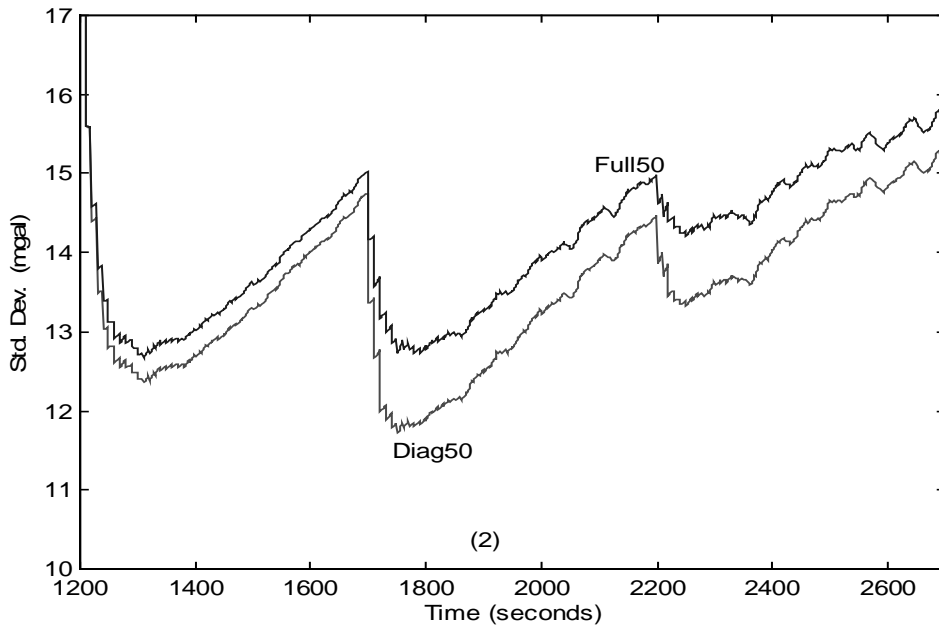
Figure 5.16: Standard deviation of the E-W component of gravity (mgal) from Diag50 and Full50 cases.

Figures 5.17-21 show the results of the *colored noise* and *less colored noise* cases for the 25-photographs simulation (see Chapter 5.3.1). The processes of these cases were done according to the modified Kalman filtering estimation due to the colored measurement noise (see Chapter 4). The autocorrelations were modeled as first order Gauss-Markov processes and three additional states were added to the estimation process.

The results achieved by processing these cases illustrate the effect of between-epoch correlations on the estimated precision of the orientation angles and gravity components. As one expects, the white noise assumption in the Kalman filter measurement model would provide more precise estimation. However, by modeling the between-epoch correlations, a significantly different conclusion is reached. Although the results show improved estimation accuracy results from colored photogrammetric noise, the gyroscopes' error calibration from aircraft maneuvers (segment (3) of the flight) provides almost twice the improvement to the estimated parameters. The colored measurement noise has improved the estimation of the gravity components by about 3-4 mgals compared to the GPS/INS-only solution (see Figures 5.20 and 5.21).

The *less colored noise* process labeled as "Corr25B" represents a less constrained solution. The improved results of this process over the *colored noise* process (about 1.0 mgal) in the gravity components error estimation indicates that weaker time correlations exist for the whole photogrammetric simulation process.
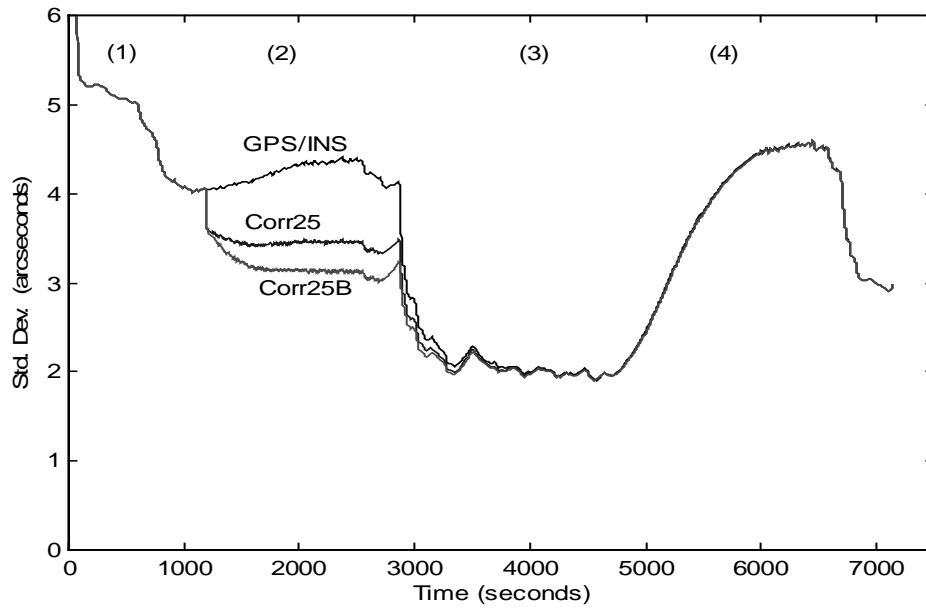
72

Figure 5.17: Standard deviation of the E/W orientation error (arcseconds) from GPS/INS, Corr25, and Corr25B.
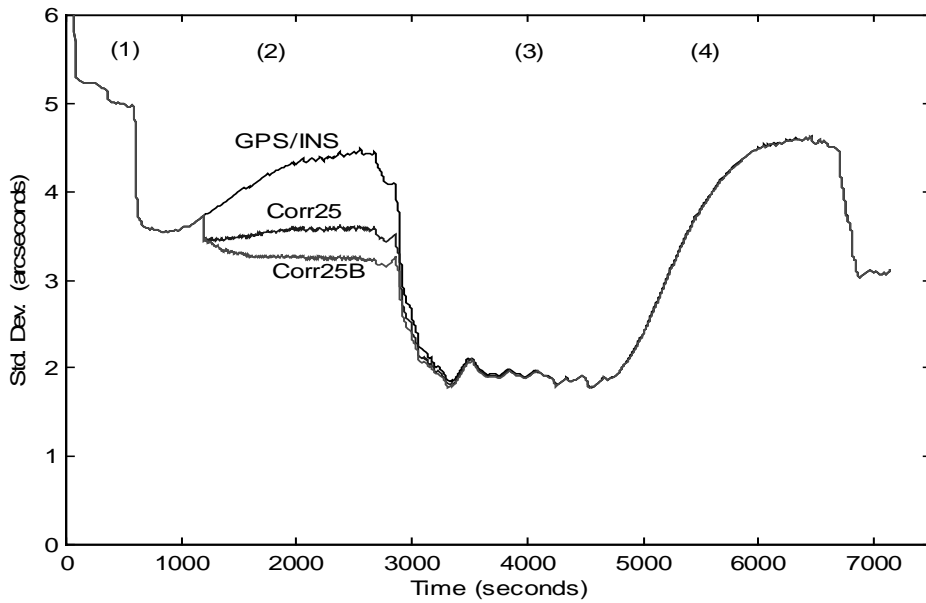

Figure 5.18: Standard deviation of the N/S orientation error (arcseconds) from GPS/INS, Corr25, and Corr25B.
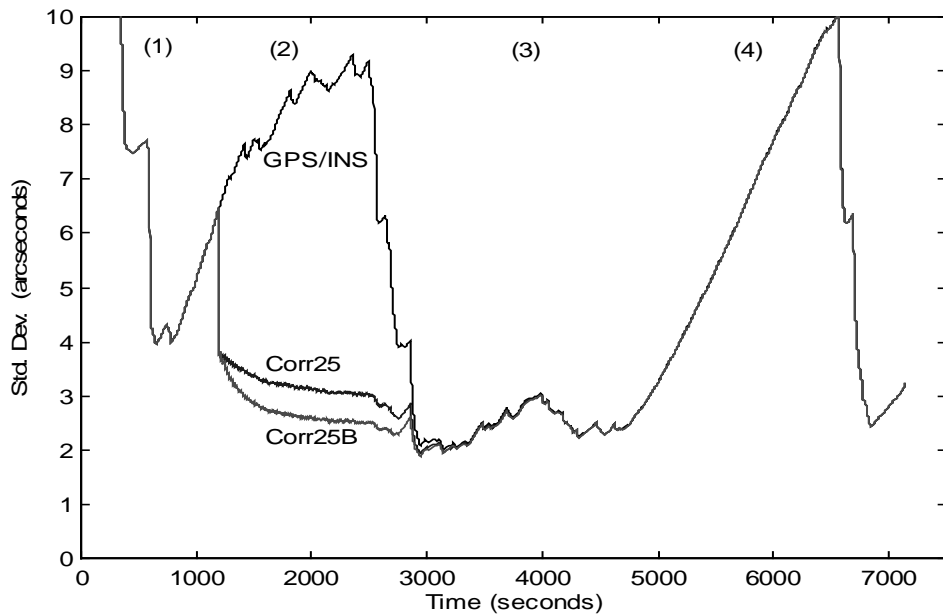
Figure 5.19: Standard deviation of the heading angle error (arcseconds) from GPS/INS, Corr25, and Corr25B.
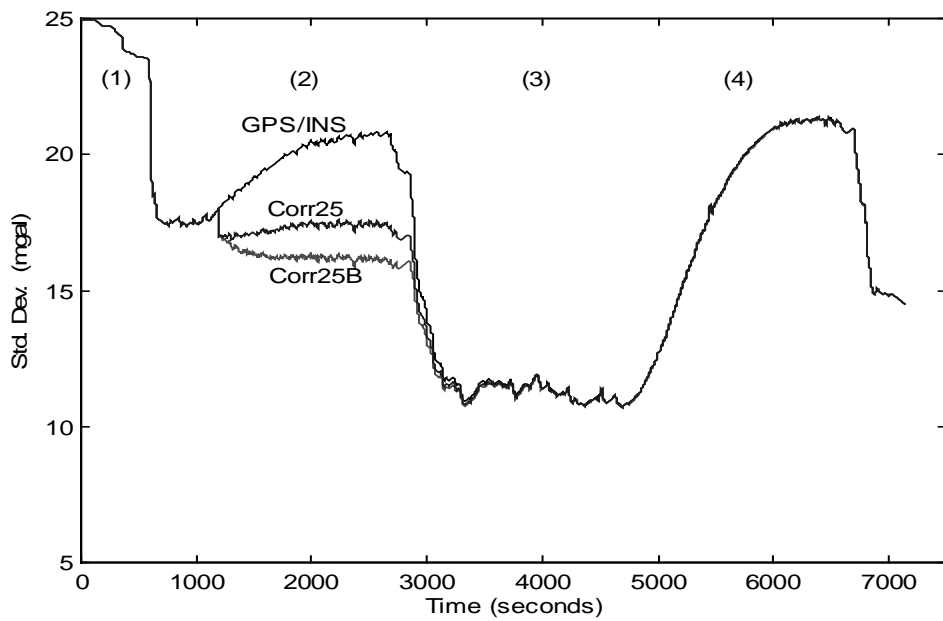

Figure 5.20: Standard deviation of the N-S component of gravity (mgal) from GPS/INS, Corr25, and Corr25B.
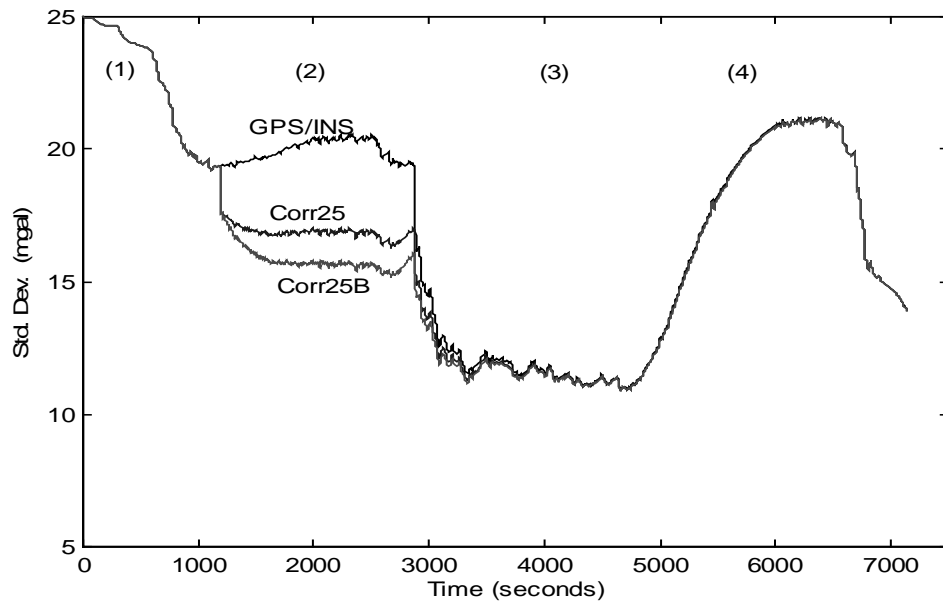
Figure 5.21: Standard deviation of the E-W component of gravity (mgal) from GPS/INS, Corr25, and Corr25B.

Figures 5.22-26 show the results of the *colored noise* and *less colored noise* cases for the 25-photographs simulation (see Chapter 5.3.1). The processes of these cases are the same as the previous *colored noise* and *less colored noise* cases, but accelerometer biases are modeled as random constant instead of random walk as originally modeled. It was found that the difference between the random walk and random constant models affects the precision of the gravity components by about 0.2 mgal. The process labeled as "Corr25C" is added towards the end of this study where twice the correlation time (β^{-1}) is used. As the correlation increases in the orientation measurements, less new information are added to the filter. In the limit, perfectly correlated orientations add no new information and orientation errors should increase with time.

Figure 5.22: Standard deviation of the E/W orientation error (arcseconds) from GPS/INS, Corr25, Corr25B, and Corr25C.
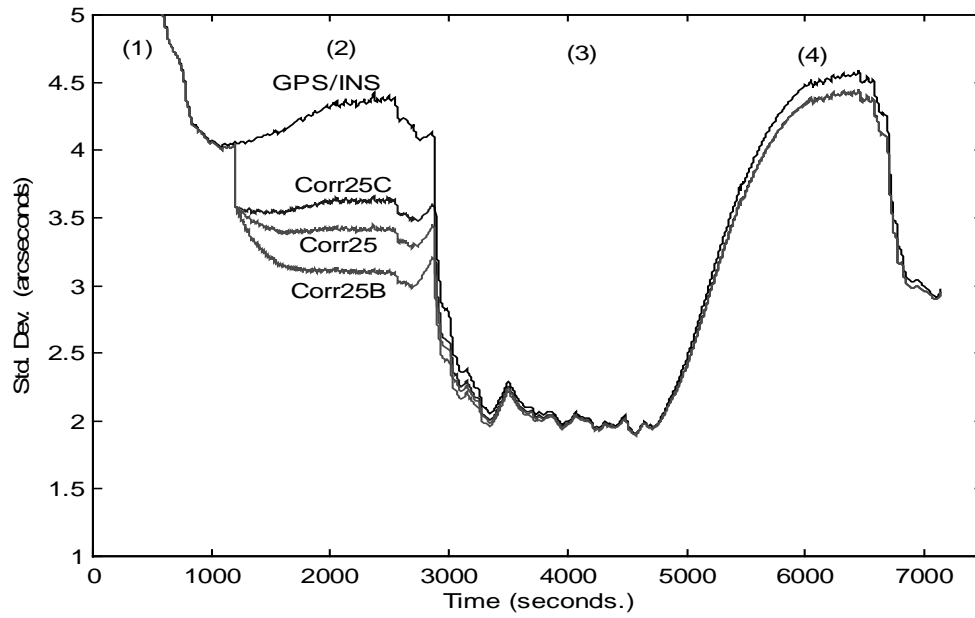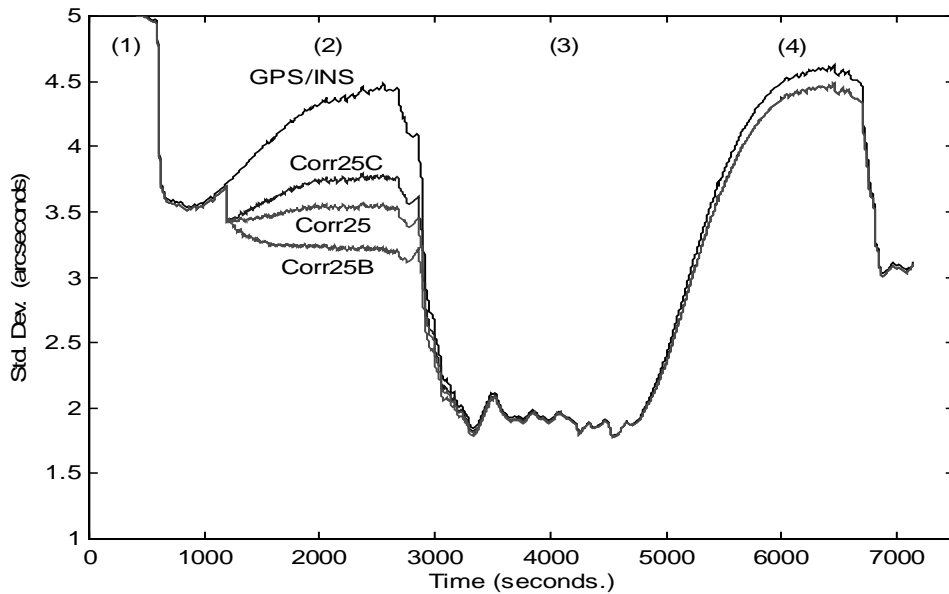

Figure 5.23: Standard deviation of the N/S orientation error (arcseconds) from GPS/INS, Corr25, Corr25B, and Corr25C.
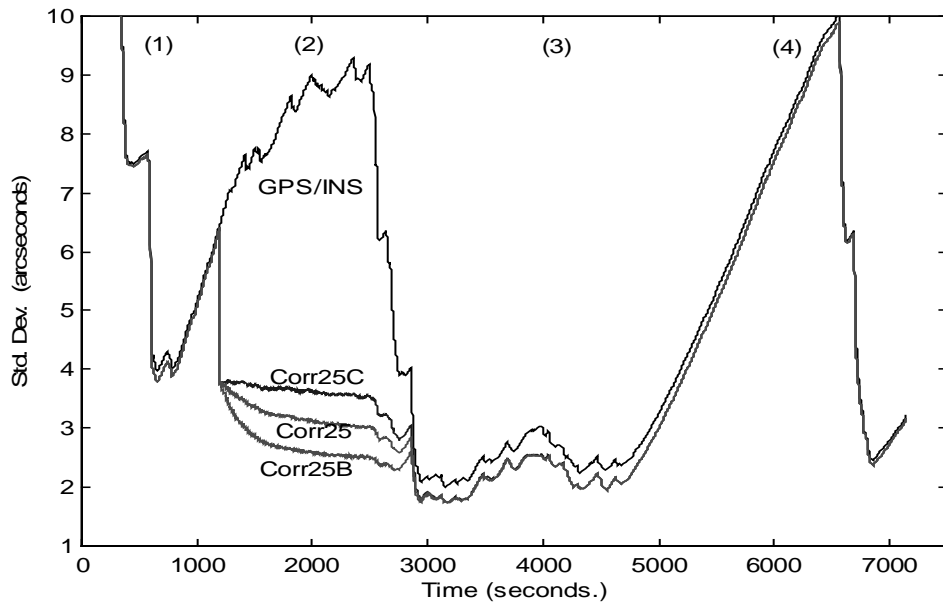
Figure 5.24: Standard deviation of the heading angle error (arcseconds) from GPS/INS, Corr25, Corr25B, and Corr25C.

Figure 5.25: Standard deviation of the N-S component of gravity (mgal) from GPS/INS, Corr25, Corr25B, and Corr25C.
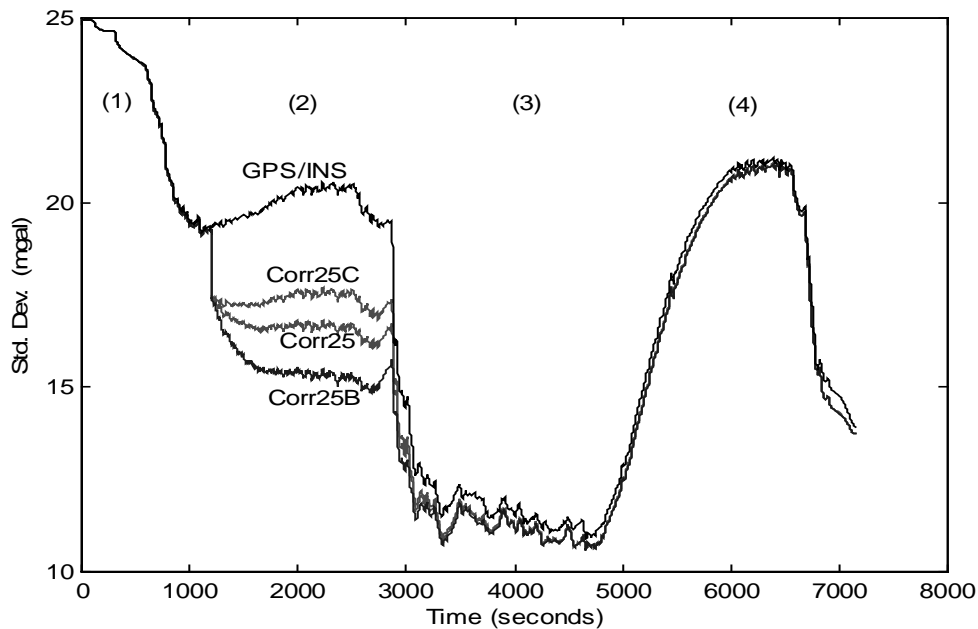
Figure 5.26: Standard deviation of the E-W component of gravity (mgal) from GPS/INS, Corr25, Corr25B, and Corr25C.

The last case considered in this analysis in the ***Diagonal variance with control at both ends***. This case uses ground control points at the beginning and at the end of the simulated set of photographs. The advantage of this configuration is shown in Figure 5.6 where the standard deviations of the orientation parameters are suppressed at both ends of the simulated sets. The standard deviation of the second and the third simulated sets show larger standard deviation. This fact is reflected clearly on the estimated gravity components of this case. The results of this case are shown in Figures 5.27-31. The standard deviation in Figures 5.30 and 5.31 gets larger by about 1 mgal (after time = 1700 seconds) due to deterioration in the accuracy of the orientation updates after the first simulated set.
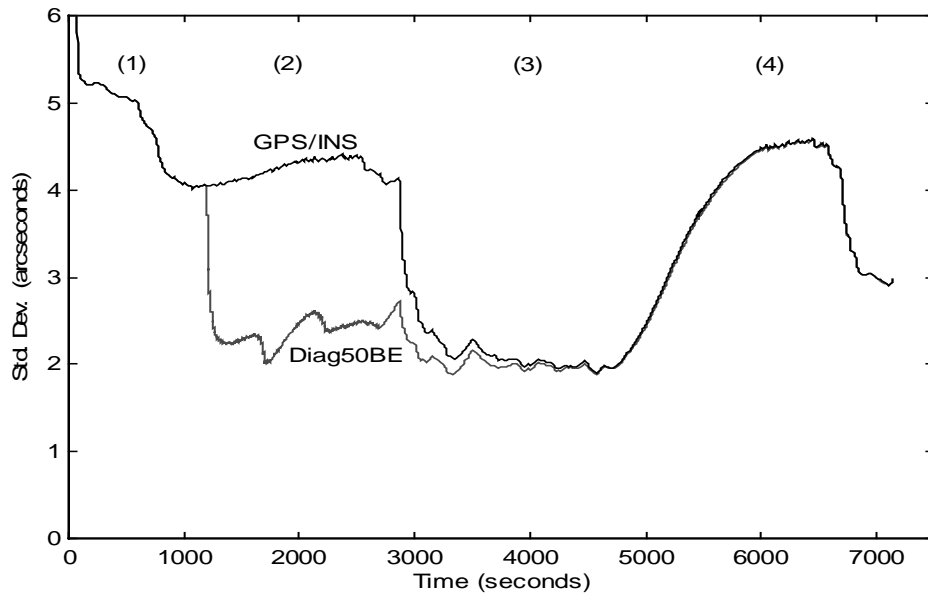
Figure 5.27: Standard deviation of the E/W orientation error (arcseconds) from GPS/INS and Diag50BE cases.
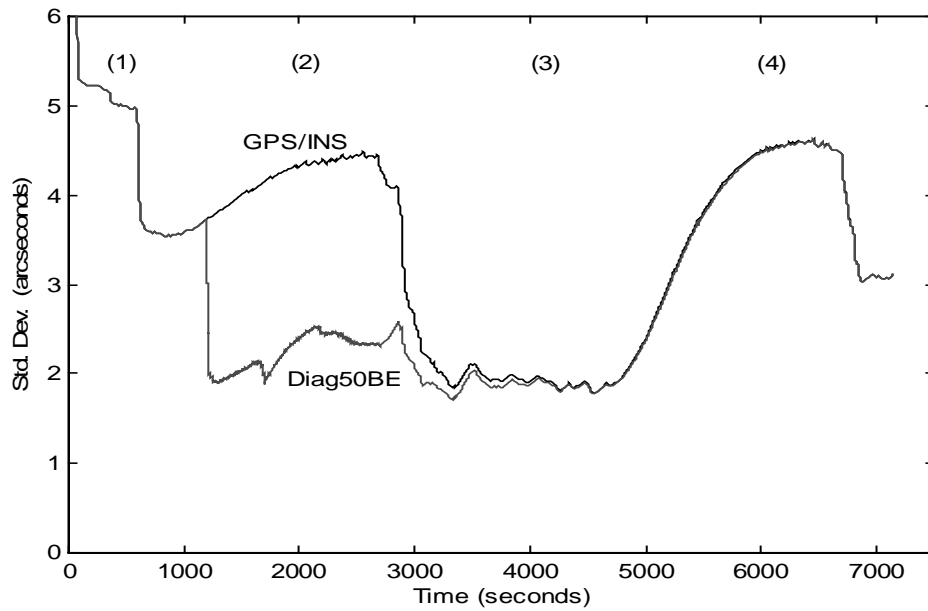
Figure 5.28: Standard deviation of the N/S orientation error (arcseconds) from GPS/INS and Diag50BE cases.
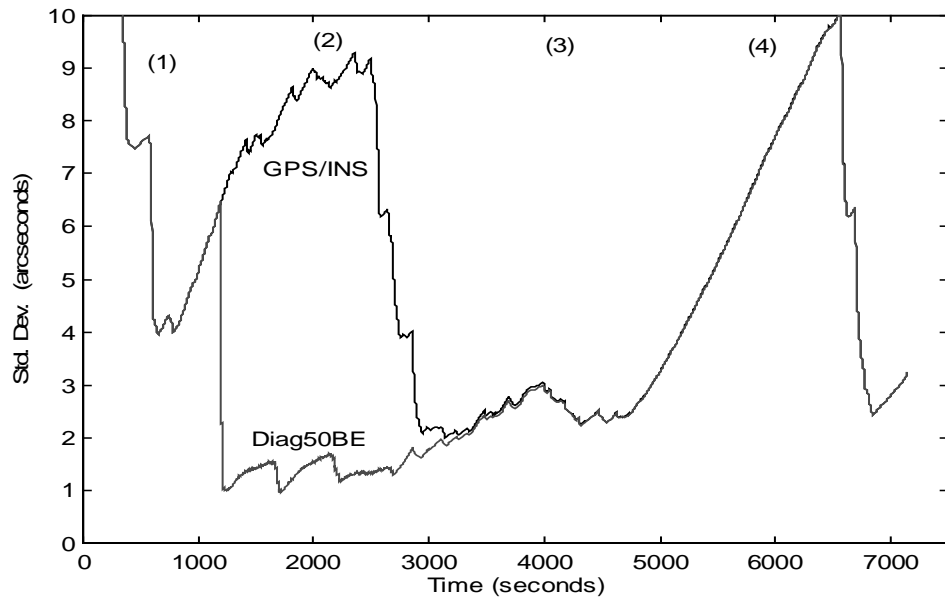
Figure 5.29: Standard deviation of the heading angle error (arcseconds) from GPS/INS and Diag50BE cases.
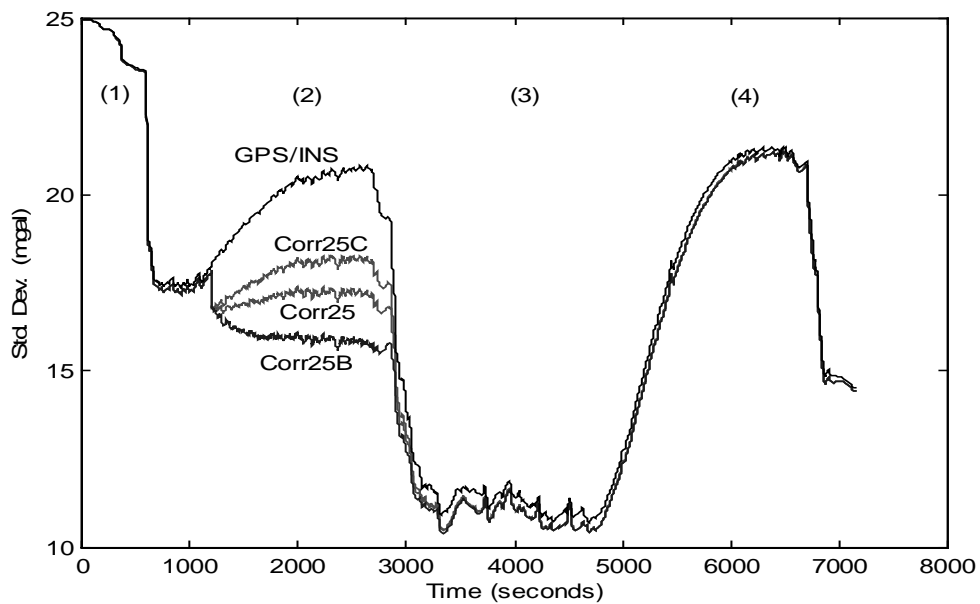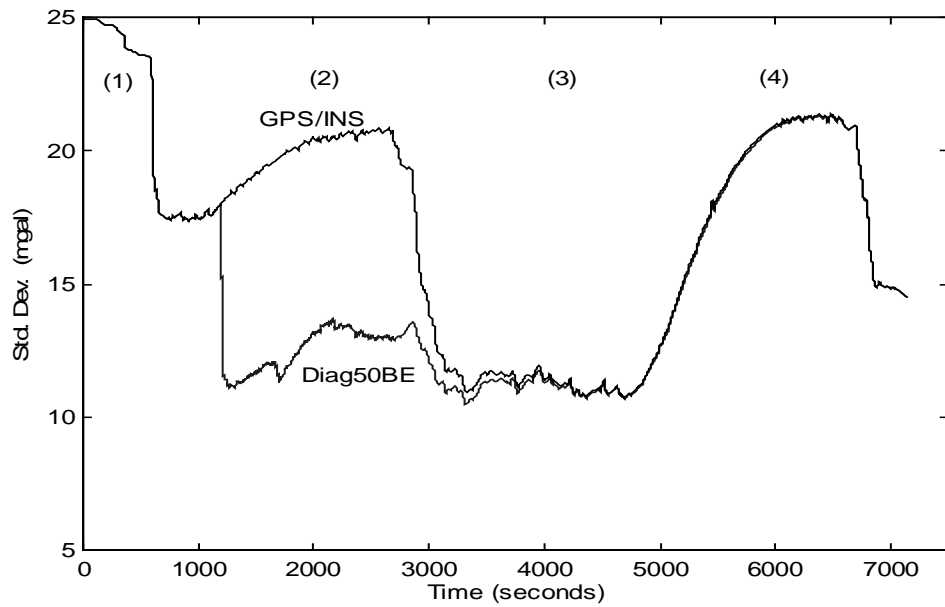

Figure 5.30: Standard deviation of the N-S component of gravity (mgal) from GPS/INS and Diag50BE cases.
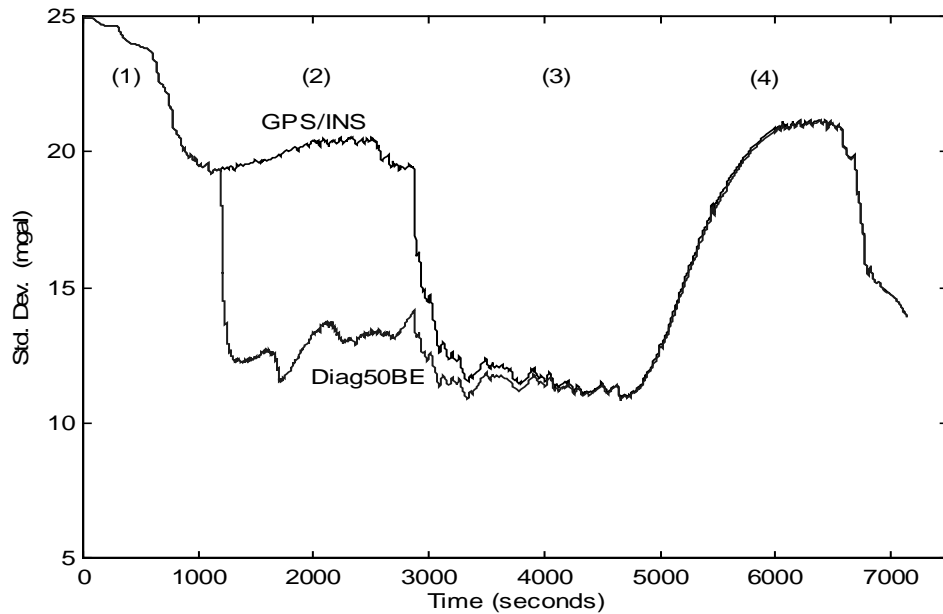
Figure 5.31: Standard deviation of the E-W component of gravity (mgal) from GPS/INS and Diag50BE cases.

Table 5.3 summarizes the results and shows the effect of the photogrammetric orientation update on both the orientation parameters and the horizontal components of gravity vector for all different cases considered in this study. The results clearly emphasize the direct relationship between the orientation accuracy and the estimability of the horizontal components of gravity. The results also show the effect of time-correlated measurements (colored noise observations) as compared with white noise measurements on the estimation process of horizontal gravity components. The processes labeled in Table 5.3 are defined in Chapter 5.4.

Process	Orientation N/S (”)	Orientation E/W (”)	Orientation Heading (”)	Gravity N/S (mgal)	Gravity E/W (mgal)
GPS/INS	4.2437	4.2163	8.0528	20.0076	19.9505
Fixed	0.8192	0.8217	0.4594	8.6680	8.4928
CorrFixed	1.8632	1.6974	1.2605	11.3436	10.6993
Diag25	1.5238	1.7003	1.0124	10.2935	10.6673
Full25	1.5805	1.7480	1.0411	10.4533	10.8099
Diag50	2.6814	2.5725	1.7293	14.0571	13.5715
Full50	2.7741	2.7343	1.7863	14.3923	14.1508
Corr25	3.5077	3.4175	3.1850	17.0921	16.6702
Corr25B	3.2503	3.1554	2.7072	16.0131	15.5715
Corr25C	3.6720	3.5861	3.6044	17.7880	17.3856
Diag50BE	2.3849	2.2442	1.3671	12.5260	12.9026

Table 5.3: Mean of the standard deviation for the orientation parameters (arcseconds) and horizontal components of gravity vector (mgal) during the second segments of the flight (study period) for all different processes.

The different processing scenarios in this study provided consistent results; the more accurate and independent orientation parameters updates, the more accurate estimation to the horizontal gravity components. The time-correlated measurement noise among the orientation parameters should be analyzed and modeled for more accurate estimation and cautious interpretation of the results. The results also highlight the importance and efficiency of the aircraft maneuvers to the INS gyro's calibration. The feasibility of aircraft maneuvers in a flight mission may substitute for independent external orientation updates.

Many geodesists and geophysicists would hope to achieve better overall accuracy results in the horizontal gravity components than the ones shown in Table 5.3. Despite this fact, the above results have proved the methodology and algorithm by showing the ability of the AIMS's sensors collection on board could serve to extract a helpful gravity information. The advancement in the design and algorithm of the integrated sensors and information would soon reveal more precise achievements.

CHAPTER 6

CONCLUSION AND RECOMMENDATIONS

Terrestrial gravimetric missions used the ZUPT technique with success in recovering the gravity vector, where the vehicle is brought to a stop at points along the way. In addition to known zero velocity at these points, a known deflections of the vertical also help in recovering the gravity vector between the points. For airborne gravimetry where the aircraft stop is not possible, the lack of high quality updates has delayed the airborne gravimetric surveys for about many years. Improved GPS receiver capabilities, the availability of powerful micro computers for data logging and analysis, international cooperation to establish continuos tracking stations, all have helped to achieve high quality position updates for airborne gravimetric missions.

Gravity vector advancements in measurement and estimation are among the many areas where precise positions of GPS had a great influence. An extensive research and simulation analyses has been done in the field of airborne vector gravimetry estimation using inertial navigation systems with GPS positions updates. This study, however, investigates the influence of yet another type of updates, namely, the orientation updates from photogrammetry, which are vital to the estimation of the horizontal components of the gravity vector, in particular. An estimation technique to the horizontal components of the gravity disturbance vector has been described. The estimation process utilizes the measurements of the Litton LN-100 inertial system, Trimble 4000 SSI GPS dual frequency receiver, and a metric frame camera. An optimal filtering technique is used to integrate both GPS and INS on the level of raw measurement of both systems. The strength of introducing accurate and independent orientation parameters, e.g., a photogrammetric source in this work, demonstrates its effect on the calibration of inertial gyros. This effect leads to substantial improvement in extraction of the horizontal components of the gravity vector.

Conventional aerial triangulation requires many ground control points for precision mapping applications. The precise positioning provided by GPS replaces the required density of ground control points in the photogrammetric aerial triangulation process. The unlimited, well-distributed GPS points of the perspective center can have tremendous effect on the photogrammetric parameter's accuracy. With GPS technology, the expensive cost of establishing ground control is reduced significantly, and photogrammetric parameters could be derived with sufficient accuracy for precise applications. The photogrammetric orientation parameters utilized in this study are derived from simulated sets of photographs with a minimal number of ground control points used to process each set. More on the simulation process can be found in Chapters 2 and 5. The orientation angles derived from photogrammetry were used to help recover the weak horizontal components of the gravity disturbance vector. As unavoidable gyro drifts most adversely affect these components, the photogrammetric orientation update is a potential cure for the drift problem.

This study considers three photogrammetric simulation processes. The basic difference between the first two processes is in the number of simulated photographs which uses the same number of ground control. The results of both cases show substantial improvements in the standard deviation estimates for both the orientation parameters and the horizontal components of gravity vector. A complete description of the simulation process can be found in Chapter 2. The third simulation process uses different distribution of ground control points.

Using different assumptions, the derived photogrammetric measurements were integrated differently with GPS/INS filter. Depending on the process specifications, an improvement of about 50% in the estimated standard deviation of the GPS/INS derived E/W and N/S angle errors was achieved from orientation updates assuming white noise measurements. For heading, the standard deviation estimate with photogrammetric updates could reach about 8 times better than the corresponding estimates from GPS/INS. These results are directly reflected on the estimated standard deviation of the horizontal components of gravity vector. An improvement of about 50%, from about 20 mgal to about 11 mgal, in the standard deviation estimates was achieved assuming no correlation between orientation updates. For colored noise measurements, however, the standard deviation estimates were improved by about 20%. Considering at-epoch correlation only, a deterioration of about 0.2 - 0.6 mgal in the standard deviation estimates as compared with white noise case. All results are summarized in Table 5.3.

Directly related to the concept of aircraft maneuvering for INS sensor's excitement and calibration, a substantial improvement in the standard deviation of the orientation angles, as well as the horizontal components of gravity vector, almost equivalent to the white noise assumption of photogrammetric updates to the GPS/INS filter was achieved by consistently changing the aircraft orientation. The change in the orientation parameters is comparable to introducing new independent observations of the orientation angles to the GPS/INS filter, which helps to separate gyro drifts from horizontal component of the gravity vector. It is noted, however, that an aerial survey of the gravity vector would more likely follow a trajectory as described in the Forward (or Backward) segment than in the looping segment. Without photogrammetric orientation during the Backward segment, the gravity vector estimation again quickly deteriorates to the level of the Forward segment without orientation updates. It is important to note here that a separate study by a colleague (Kwon, 1998) on airborne GPS/INS vector gravimetry has shown instability in the deflection components determination during aircraft maneuvers. Aircraft dynamics adversely affect gravity determination during aircraft maneuvers.

Loose integration of photogrammetry with semi-tightly integrated GPS/INS is the integration mode selected for this study. In this mode, the simulated photographs were first processed by bundle adjustment program to solve for the exterior orientation parameters. The resolved orientation parameters were used as external updates to the GPS/INS Kalman filter. The time-correlation in the measurement noise is considered in this study and the results of the correlation analysis were used in the integrated process. The correlated measurement updates violates the Kalman assumption that the

measurements can only be contaminated with white noise. This study uses a modified measurement model where the time correlations are modeled in the filter. The modified measurement model is described in Chapter 4.

In this era of sensor integration, e.g. GPS, INS, Camera, Altimeter, Synthetic Aperture Radar (SAR), etc., different combinations might lead to substantially improved accuracy. This work has demonstrated the ability to considerably calibrate the INS gyros, which is critical part in the field of airborne gravimetry. While there is still a great deal of research and development necessary to improve the accuracy and wavelength resolution in airborne gravimetry, the results of this study proved the benefit of photogrammetric sensor for GPS/INS gravimetric missions. Using such sensors for mapping missions could be easily used to guide geophysical exploration missions in prospective areas.

In contrast to the horizontal components of gravity vector where the INS gyro drifts are the main target need to be stabilized, the scalar gravimetry (vertical component) has been successfully implemented as the gyro drifts do not have the same diverse impact on its accuracy. The airborne vector gravimetry proved to be more efficient and more economic survey than the traditional gravimetric land survey missions. As the technology advances and more robust and more accurate integrated INS/GPS/Camera systems are built, the fruitful results of more accurate gravity signal will be achieved, of course, in addition to the navigational and mapping side of the integrated system.

In accordance with the accomplishment of this work, it could be advised to investigate modeling alternatives to the Kalman filtering states. The Kalman filtering process is sensitive to the statistical representation of its states. More accurate mathematical models that fit real data should be searched and used. It is also recommended to look after parameters that were not modeled, multipath, troposphere, and aircraft dynamics, for instance. It should be mentioned that the first order Gauss-Markov stochastic modeling to the gravity disturbance vector used in this study is a considerable simplification to the true gravity field. More accurate gravity field modeling needs to be used. The photogrammetric derived orientation accuracy depends on the spatial distribution of the ground control points. Different distribution designs may yield different results. More variability in the simulated DEM would build stronger geometry and results in more accurate orientations from the bundle adjustment computations. To build confidence in results obtained, it would be worthwhile to design a flight test over a selected area with stronger variation in gravity field and with all required sensors onboard. Unlike traditional photogrammetric aerotriangulation, digital photogrammetry uses epipolar geometry to refine orientation parameters. The epipolar geometry is the process of aligning two photographs in order to cause the line connecting the point of interest in both photos to be parallel to the airbase of both photos. As GPS/INS computations deliver accurate exposure station positions and good attitude approximations, conjugate points measurements are sufficient to support more accurate orientation parameters. This direction of research is worth the effort for more investigation.

APPENDIX A

GRAVITY FIELD MODELING

A.1 Introduction

One major source of error in inertial geodesy is the unknown gravity field. Using normal gravity field as an approximation does not yield satisfactory results for precision applications. The Earth's gravitational field derived from detailed global gravitational field models could be known to better than one part 10^5 (Jekeli, 1997). The positional error caused by anomalous gravity field was presented by Forsberg (1986), Groten et al. (1987), and Jekeli (1996). The systematic gravity induced position error δp in a Schuler-tuned channel of a free INS may be roughly approximated by $\delta p = \delta g/\omega_s^2$; δg is gravity disturbance and ω_s is Schuler frequency (Eissfeller and Spietz, 1989). The state space modeling of the anomalous gravity field has been applied successfully in the past years, (e.g., Schwarz, 1986; Jekeli, 1991; Knickmeyer, 1990; and Eissfeller, 1996). As the gravity field is not a finite dimensional state space variable, the Markovian representation of gravity models was criticized by several authors. Nevertheless, the first and the second-order Gauss Markov covariance model for local gravity field was among the best practical choices as it was confirmed by real data. For the second-order model, and following Eissfeller (1996), the derivation of upward gravity potential is shown. Unlike traditional covariance functions where height dependency is ignored, the variance and correlation length are derived as functions of height. In this appendix, the auto covariance gravity models are briefly reviewed and a height and azimuth dependent covariance function is derived.

A.2 Covariance Functions for the Anomalous Gravity Field

The covariance functions play a key role in gravity field prediction and estimation. As the anomalous quantities of the gravity field are related, it is essential to derive all covariance functions from one basic covariance function (kernel); all other covariance functions can be derived using covariance propagation. Following Moritz (1980), an isotropic and homogenous covariance function of the disturbing potential has the following form:

$$K(P,Q) = \sum_{n=2}^{\infty} k_n \left(\frac{R^2}{rr'} \right)^{n+1} P_n(\cos\psi) \tag{A.1}$$

where:

k_n : Conventional harmonic coefficients.

R : Radius of spherical Earth.

r, r' : Radius vectors of P and Q respectively.

$P_n(\cos\psi)$: Conventional Legendre polynomials.

ψ : Spherical distance between P and Q.

Isotropic and homogenous assumptions mean invariance with respect to rotation and translation, respectively. In a neighborhood of a specified point on the sphere, the spherical distance might be replaced by its tangent plane (z = 0), as the spherical covariance function is approximated by flat Earth model,

$$K(P,Q) = K(\rho) \tag{A.2}$$

where ρ is the horizontal distance between P and Q.

Three parameters are of importance in defining covariance functions: the variance $K(0)$ is the value of covariance function at $\rho = 0$; the correlation length ξ is the value of the ρ where $K(\rho)$ equals half of $K(0)$, and the correlation parameter β is a dimensionless quantity related to the curvature κ of the covariance curve.

$$\beta = \frac{\kappa \xi^2}{K(0)} \tag{A.3}$$

Positive definiteness is an important property of a covariance function. $K(P,Q)$ type is positive definite if all k_n coefficients are nonnegative. It can also be shown Moritz (1980), that the covariance functions of the functionals (gravity anomaly, deflection of the vertical, etc.) derived from this kernel by covariance propagation are positive definite. Nonnegativity of the spectrum $S(\omega)$ is also equivalent to positive definiteness. The transform pair between state and frequency domain of the two dimensional covariance function $K(\rho)$ is defined by Hankel transform as follows:

$$K(\rho) = 2\pi \int_0^\infty S(\omega) J_0(\omega\rho) \omega \, d\omega \tag{A.4}$$

$$S(\omega) = \frac{1}{2\pi} \int_0^\infty K(\rho) J_0(\omega\rho) \rho \, d\rho \tag{A.5}$$

where ω stands for frequency, and J_0 is Bessel's function of zero order.

Many analytical covariance functions for the anomalous gravity field have been used in the literature. An overview of these models can be found in Eissfeller (1996) and Knickmeyer (1990). Some of these models are shown in Table A.1.

Name	Covariance Function	2D-Power Spectral Density
Gaussian	$\sigma^2 \exp(-\beta^2 \rho^2)$	$\exp(-\omega^2 / 4\beta^2)$
Reciprocal Distance	$\sigma^2 / (1 + \beta^2 \rho^2)^{1/2}$	$\dfrac{\exp(-\omega/\beta)}{\omega}$
Poisson	$\sigma^2 / (1 + \beta^2 \rho^2)^{3/2}$	$\exp(-\omega/\beta)$
2$^\text{nd}$ Order Gauss Markov	$\sigma^2 \exp(-\beta\rho)[1 + \beta\rho]$	$4\sigma^2 \beta^3 / (\omega^2 + \beta^2)^2$
3$^\text{rd}$ Order Gauss Markov	$\sigma^2 \exp(-\beta\rho)\left(1 + \beta\rho + \frac{1}{3}\beta^2 \rho^2\right)$	$16\sigma^2 \beta^5 / 3(\omega^2 + \beta^2)^3$

Table A.1: Analytical covariance functions for the anomalous gravity field.

A way from highly nonlinear covariance models, and as confirmed by several authors, among them Vassiliou and Schwarz (1987), that the second order Gauss Markov modeling of the local gravity field is the best choice as, besides its linearity, it fits real data well. However, both the variance and the correlation parameters are independent from the third dimension. In other words, the covariance model is function of only the horizontal distance. The following section is one step towards deriving a covariance function where the third dimension (height) and the direction (azimuth) are parameters in its variance and correlation length.

A.3 Height and Azimuth-Dependent Covariance Function

The two-dimensional covariance function given by equation (A.4) can be extended to account for height and direction dependence as shown in the following form:

$$K(P,Q) = 2\pi \int_{0}^{\infty} S(\omega) J_0(\omega\rho) \phi_1(z_P,\omega) \phi_1(z_Q,\omega) \phi_2(\alpha_{PQ},\omega) \omega d\omega \tag{A.6}$$

Both functions $\phi(z_P,\omega)$ and $\phi(z_Q,\omega)$ represent a similar form of height factor. $\phi(\alpha_{PQ},\omega)$ corresponds to the azimuth factor of point Q with respect to point P. Using ρ, α, and z coordinates, the Laplace's equation may be written as follows (Moritz, 1976):

$$\Delta K = K_{\rho\rho} + \frac{1}{\rho} K_{\rho} + \frac{1}{\rho^2} K_{\alpha\alpha} + K_{zz} \tag{A.7}$$

The covariance function for the disturbing potential K(P,Q) satisfies Laplace's equation at both points P and Q. At point P Laplace's equation is represented by:

$$\frac{\partial^2 K}{\partial \rho^2} + \frac{1}{\rho} \frac{\partial K}{\partial \rho} + \frac{1}{\rho^2} \frac{\partial^2 K}{\partial \alpha_{PQ}^2} + \frac{\partial^2 K}{\partial z_P^2} = 0 \tag{A.8}$$

Applying this condition on the form of (A.6) of the covariance function results in the following:

$$\left[\frac{\partial^2 J_0(\omega\rho)}{\partial \rho^2} + \frac{1}{\rho} \frac{\partial J_0(\omega\rho)}{\partial \rho}\right] \phi_1(z_P,\omega) \phi_2(\alpha_{PQ},\omega) + \frac{1}{\rho^2} \frac{\partial^2 \phi_2(\alpha_{PQ},\omega)}{\partial \alpha_{PQ}^2} \cdot$$
$$J_0(\omega\rho) \phi_1(z_P,\omega) + \frac{\partial^2 \phi_1(z_P,\omega)}{\partial z_{PQ}^2} J_0(\omega\rho) \phi_2(\alpha_{PQ},\omega) = 0 \tag{A.9}$$

The Bessel's function of first kind and order n satisfies the following differential equation:

$$x^2 y'' + x y' + (x^2 - n^2) y = 0 \tag{A.10}$$

and for zero order (n = 0), equation (A.10) becomes

$$y'' + \frac{y'}{x} + y = 0 \qquad\qquad (A.11)$$

By applying equation (A.11) into equation (A.9) and rearranging terms, equation (A.9) reduced to the following:

$$\frac{1}{\rho^2}\frac{\partial^2 \phi_2(\alpha_{PQ},\omega)}{\partial \alpha_{PQ}^2}\phi_1(z_P,\omega) + \frac{\partial^2 \phi_1(z_P,\omega)}{\partial z_{PQ}^2}\phi_2(\alpha_{PQ},\omega) - \omega^2 \phi_1(z_P,\omega)\phi_2(\alpha_{PQ},\omega) = 0 \quad (A.12)$$

or:

$$\frac{1}{\rho^2}\frac{\phi_2''}{\phi_2} + \frac{\phi_1''}{\phi_1} = \omega^2 \qquad\qquad (A.13)$$

where:

$$\phi_2 = \phi_2(\alpha_{PQ},\omega)$$
$$\phi_1 = \phi_1(z_P,\omega)$$

The upward continuation factor has been derived to satisfy the following boundary conditions see Moritz (1976) and Eissfeller (1996):

$$\phi_1(z_P = 0,\omega) = 1$$
$$\phi_1(z_P \to \infty,\omega) = 0$$

and it is given by:

$$\phi_1(z_P,\omega) = e^{-z_P\omega} \qquad\qquad (A.14)$$

Similarly,

$$\phi_1(z_Q,\omega) = e^{-z_Q\omega} \qquad\qquad (A.15)$$

For the azimuth factor, the following periodic function (period $= 2\pi$), which satisfies the differential equation (A.13) is proposed.

$$\phi_2(\alpha_{PQ},\omega) = A + B\omega\alpha_{PQ} \qquad\qquad (A.16)$$

where both A and B are constants determined empirically. The Fourier series representation of this function takes the following form:

$$\phi_2(\alpha_{PQ},\omega) = A + 2A\sum_{n=1}^{\infty}\left[\sin c(n\pi\omega)\right]\sin n\omega\alpha_{PQ} +$$

$$2B\sum_{n=1}^{\infty}\frac{1}{n}\left[\sin c(n\pi\omega) - \cos(n\pi\omega)\right]\cos n\omega\alpha_{PQ} \tag{A.17}$$

where

$$\sin c(n\pi\omega) = \frac{\sin n\pi\omega}{n\pi\omega} \tag{A.18}$$

and for (n=1), this function becomes:

$$\phi_2(\alpha_{PQ},\omega) = A + 2A\left[\sin c(\pi\omega)\right]\sin \omega\alpha_{PQ} + 2B\left[\sin c(\pi\omega) - \cos \pi\omega\right]\cos \omega\alpha_{PQ} \tag{A.19}$$

Substituting equations (A.14-A.16) into equation (A.6) gives the following:

$$K(P,Q) = 2\pi\int_{0}^{\infty}S(\omega)J_0(\omega\rho)e^{-\omega(z_P+z_Q)}$$

$$\left[A + 2A\left[\sin c(\pi\omega)\right]\sin \omega\alpha_{PQ} + 2B\left[\sin c(\pi\omega) - \cos \pi\omega\right]\cos \omega\alpha_{PQ}\right]\omega d\omega \tag{A.20}$$

Finally, the height and direction dependent covariance function has the following structure:

$$K(P,Q) = f(\rho, z_P + z_Q, \alpha_{PQ}) \tag{A.21}$$

The analytical evaluation of equation (A.20) is not trivial. However, utilizing the convolution theorem of Fourier transform represents an alternative. A general representation of the PSD of the height and azimuth dependent autocorrelation function (ACF) of the nth order can be written as:

$$S_n(\omega,z,\alpha) = S_n(\omega)\exp(-\omega z)\phi(\omega\alpha) \tag{A.22}$$

where $S_n(\omega)$ is the one-dimensional PSD of the nth order flat Earth ACF for the anomalous gravity potential $K_n(\rho)$. Both the ACF and the PSD are given by Gelb (1974) as follows:

$$K_n(\rho) = \sigma^2 \exp(-\beta\rho)\sum_{k=0}^{n-1}\frac{\Gamma(n)(2\beta\rho)^{n-k-1}}{(2n-2)!k!\Gamma(n-k)} \tag{A.23}$$

$$S_n(\omega) = \frac{\sigma^2 (2\beta)^{2n-1} \Gamma(n)^2}{(2n-2)!(\omega^2 + \beta^2)^n} \qquad (A.24)$$

where:

σ : Standard deviation of anomalous gravity potential.

β : Correlation parameter.

Γ : Gamma function.

As mentioned earlier, the second-order (n=2) Gauss Markov modeling of gravity field is among the best models as it was confirmed by real data. It is of interest, therefore, to investigate the special case of second order. The second order Gauss Markov process and its PSD are given as follows:

$$K_{TT}(\rho) = \sigma_T^2 (1 + \beta\rho) \exp(-\beta\rho) \qquad (A.25)$$

$$S(\omega) = \frac{4\sigma^2 \beta^3}{(\omega^2 + \beta^2)^2} \qquad (A.26)$$

The inverse Fourier transform of equation (A.22), for the second order, reveals the height and azimuth dependent ACF in state space.

$$K(\rho, z_{PQ}, \alpha_{PQ}) = F^{-1}\{G_1(\omega)G_2(\omega)G_3(\omega)\} \qquad (A.27)$$

with:

$$G_1(\omega) = S_2(\omega) \qquad (A.28)$$

$$G_2(\omega) = \exp(-\omega z_P) \qquad (A.29)$$

$$G_3(\omega) = A + 2A[\operatorname{sinc}(\pi\omega)]\sin\omega\alpha_{PQ} + 2B[\operatorname{sinc}(\pi\omega) - \cos\pi\omega]\cos\omega\alpha_{PQ} \qquad (A.30)$$

The following equations give the height-dependent model and the associated differential equations of the disturbing potential. For more details the reader is referred to Eissfeller (1996).

$$\Phi_{TT}(\rho, z) = \sigma^2 \exp(-\beta\rho)\frac{2}{\pi}\{(1+\beta\rho)f_1(z) - \beta z f_2(z)\} \qquad (A.31)$$

with:

$$f_1(z) = \sin(\beta z)ci(\beta z) - \cos(\beta z)si(\beta z) \qquad (A.32)$$

$$f_2(z) = \cos(\beta z)ci(\beta z) + \sin(\beta z)si(\beta z) \qquad (A.33)$$

91

and

$$si(x) = \sum_{k=1}^{\infty} \frac{(-1)^{k+1} x^{2k-1}}{(2k-1)(2k-1)!} - \frac{\pi}{2} \tag{A.34}$$

$$ci(x) = \sum_{k=1}^{\infty} \frac{(-1)^{k} x^{2k}}{2k(2k)!} + \ln x + C \tag{A.35}$$

$ci(x)$ and $si(x)$ are called sine and cosine integral functions respectively. C=0.577215664 and is known as Euler's constant.

The height-dependent auto-covariance function parameters can be defined as follows:

$$\sigma^2(z) = \frac{2}{\pi}(f_1 - \beta_0 z f_2)\sigma_0^2 \tag{A.36}$$

$$\beta(z) = \frac{\beta_0}{1 - \beta_0 z \dfrac{f_2}{f_1}} \tag{A.37}$$

where:

- $\sigma(z)$: Height-dependent variance.
- σ_0 : Variance at zero height.
- $\beta(z)$: Height-dependent correlation parameter.
- β_0 : Correlation parameter at zero height.

INS ERROR MODEL AND DYNAMICS MATRIX

The system linear dynamics of the Kalman filter state equation is given by equation (4.9). This equation is repeated below in (B.1) for convenience. The state vector elements of this equation are defined in Chapter 4, equation (4.10).

This appendix gives the elements of the submatrices of the dynamics matrix based on the INS error model derived in Chapter 3 and based on the stochastic modeling of the system noise detailed in Chapter 4.

$$
\begin{pmatrix} \dot{x}_1 \\ \dot{x}_2 \\ \dot{x}_3 \\ \dot{x}_4 \\ \dot{x}_5 \\ \dot{x}_6 \end{pmatrix} = \begin{pmatrix} F_{11} & F_{12} & F_{13} & F_{14} & 0 & 0 \\ 0 & F_{22} & 0 & 0 & 0 & 0 \\ 0 & 0 & 0 & 0 & 0 & 0 \\ 0 & 0 & 0 & F_{44} & 0 & 0 \\ 0 & 0 & 0 & 0 & F_{55} & 0 \\ 0 & 0 & 0 & 0 & 0 & F_{66} \end{pmatrix} \begin{pmatrix} x_1 \\ x_2 \\ x_3 \\ x_4 \\ x_5 \\ x_6 \end{pmatrix} + G \begin{pmatrix} w_1 \\ w_2 \\ w_3 \\ w_4 \\ w_5 \\ w_6 \end{pmatrix} \tag{B.1}
$$

The submatrix F_{11} is given by equation (3.15). The following matrices F_{12}, F_{13} and F_{14} show the effect of sensor errors on the navigation solution errors.

$$
F_{12} = \begin{bmatrix} 0_{(3\times3)} & 0_{(3\times3)} \\ D^{-1}C_b^n & D^{-1}C_b^n \begin{bmatrix} f_1 & 0 & 0 \\ 0 & f_2 & 0 \\ 0 & 0 & f_3 \end{bmatrix} \\ 0_{(3\times3)} & 0_{(3\times3)} \end{bmatrix} \tag{B.2}
$$

$$
F_{13} = \begin{bmatrix} 0_{(3\times3)} \\ -C_b^n \\ 0_{(3\times3)} \end{bmatrix} \tag{B.3}
$$

$$
F_{14} = \begin{bmatrix} 0_{(3\times3)} \\ D^{-1}{}_{(3\times3)} \\ 0_{(3\times3)} \end{bmatrix} \tag{B.4}
$$

where C_b^n is the transformation matrix from *b*-frame to *n*-frame. (f_1, f_2, f_3) is the accelerometer sensed specific force. *D* matrix is a conversion matrix and given by equation (2.17).

$$C_b^n = \begin{bmatrix} \cos\chi\cos\alpha & -\cos\eta\sin\alpha+\sin\eta\sin\chi\cos\alpha & \sin\eta\sin\alpha+\cos\eta\sin\chi\cos\alpha \\ \cos\chi\sin\alpha & \cos\eta\cos\alpha+\sin\eta\sin\chi\sin\alpha & -\sin\eta\cos\alpha+\cos\eta\sin\chi\sin\alpha \\ -\sin\chi & \sin\eta\cos\chi & \cos\eta\cos\chi \end{bmatrix}$$

(B.5)

where χ, η, and α are the angles pitch, roll, and yaw respectively.

F_{22}, F_{33} and F_{44} correspond to the stochastic models of the sensor error:

$$F_{22} = [0]_{(6x6)} \tag{B.6}$$

$$F_{44} = diag[-\beta_{gN}, -\beta_{gE}, -\beta_{gD}] \tag{B.7}$$

$$F_{66} = diag[-\beta_{CN}, -\beta_{CE}, -\beta_{CD}] \tag{B.8}$$

$$F_{55} = [0]_{(8x8)} \tag{B.9}$$

The formulation of the noise weight matrix $G_{k,k-1}$ in equation (4.11) is given by the following:

$$G_{k,k-1} = \begin{pmatrix} 0 & 0 & 0 & 0 & 0 & 0 & 0 & 0 & 0 \\ 0 & C_b^n & 0 & 0 & 0 & 0 & I & 0 & 0 \\ 0 & 0 & C_b^n & 0 & 0 & 0 & 0 & 0 & 0 \\ 0 & 0 & 0 & 0 & 0 & 0 & 0 & 0 & 0 \\ 0 & 0 & 0 & 0 & I & 0 & 0 & 0 & 0 \\ 0 & 0 & 0 & 0 & 0 & I & 0 & 0 & 0 \\ 0 & 0 & 0 & 0 & 0 & 0 & I & 0 & 0 \\ 0 & 0 & 0 & 0 & 0 & 0 & 0 & I_8 & 0 \\ 0 & 0 & 0 & 0 & 0 & 0 & 0 & 0 & I \end{pmatrix}$$

(B.10)

Note that all elements are sub-matrices of size (3x3) except the corresponding column and row where I_8 is located (GPS ionospheric terms).

APPENDIX C

INS ERROR MODELING AND

APPROXIMATIONS

The derivation of the INS error model in Chapter 3 approximates the principal radii of curvature N and M by the mean Gaussian radius of the Earth, R.

$$R = \sqrt{NM} \tag{C.1}$$

This appendix derives the INS error model without the above approximation, and provides numerical values to the errors introduced in the model caused by such approximation. The linear perturbation to the navigation equations, expressed in the n-frame is given in equations (3.6) and (3.7). These equations are repeated here for convenience. The definitions of the separate elements are not repeated and can be found in Chapter 3.

$$\dot{\psi}^n = -\omega_{in}^n \times \psi^n - C_b^n \delta\omega_{ib}^b + \delta\omega_{in}^n \tag{C.2}$$

$$\frac{d}{dt}\delta v^n = -\delta(\Omega_{in}^n + \Omega_{ei}^n)v^n - (\Omega_{in}^n + \Omega_{ie}^n)\delta v^n + \delta f^n + \overline{\Gamma}^n \delta p^n + \delta g^n \tag{C.3}$$

The individual terms of these equations are shown below:

$$\dot{\psi}^n = \frac{d}{dt}\begin{bmatrix} \psi_N^n & \psi_E^n & \psi_D^n \end{bmatrix}^T \tag{C.4}$$

$$\omega_{in}^n \times \psi^n = \begin{pmatrix} \dot{\ell}_1 \cos\phi \\ -\dot{\phi} \\ -\dot{\ell}_1 \sin\phi \end{pmatrix} \times \begin{pmatrix} \psi_N^n \\ \psi_E^n \\ \psi_D^n \end{pmatrix} = \begin{pmatrix} \dot{\ell}_1 \sin\phi\, \psi_E^n - \dot{\phi}\, \psi_D^n \\ -\dot{\ell}_1 \cos\phi\, \psi_D^n - \dot{\ell}_1 \sin\phi\, \psi_N^n \\ \dot{\ell}_1 \cos\phi\, \psi_E^n + \dot{\phi}\, \psi_N^n \end{pmatrix} \tag{C.5}$$

$$C_b^n \delta\omega_{ib}^b = R_3(-\text{yaw})R_2(-\text{pitch})R_1(-\text{roll})\begin{pmatrix} \psi_1^b \\ \psi_2^b \\ \psi_3^b \end{pmatrix} \tag{C.6}$$

$$\delta\omega_{in}^n = \begin{pmatrix} \delta\dot{\lambda}\cos\phi - \dot{\ell}_1 \sin\phi\,\delta\phi \\ -\delta\dot{\phi} \\ -\delta\dot{\lambda}\sin\phi - \dot{\ell}_1 \cos\phi\,\delta\phi \end{pmatrix} \tag{C.7}$$

$$\frac{\mathrm{d}}{\mathrm{dt}}\delta v^n = \begin{pmatrix} \dot{\phi}\delta\dot{h} + \dot{h}\delta\dot{\phi} + \ddot{\phi}\delta h + (M+h)\delta\ddot{\phi} \\ \left(\begin{array}{l} \dot{\lambda}\cos\phi\delta\dot{h} + \dot{h}\cos\phi\delta\dot{\lambda} - \dot{h}\dot{\lambda}\sin\phi\delta\phi + \delta h(\ddot{\delta}\cos\phi - \dot{\lambda}\dot{\phi}\sin\phi) + \\ (N+h)[(\delta\ddot{\lambda} - \dot{\lambda}\dot{\phi}\delta\phi)\cos\phi - (\ddot{\lambda}\delta\phi + \dot{\phi}\delta\dot{\lambda} + \dot{\lambda}\delta\dot{\phi})\sin\phi] \end{array} \right) \\ -\delta\ddot{h} \end{pmatrix} \tag{C.8}$$

$$\delta(\Omega_{in}^n + \Omega_{ei}^n)v^n = \begin{pmatrix} 0 & \delta\dot{\lambda}\sin\imath + \dot{\ell}_2\cos\phi\delta\phi & -\delta\dot{\phi} \\ -\delta\dot{\lambda}\sin\phi - \dot{\ell}_2\cos\phi\delta\phi & 0 & -\delta\dot{\lambda}\cos\phi + \dot{\ell}_2\sin\phi\delta\phi \\ \delta\dot{\phi} & \delta\dot{\lambda}\cos\phi - \dot{\ell}_2\sin\phi\delta\phi & 0 \end{pmatrix} \begin{pmatrix} (M+h)\dot{\phi} \\ (N+h)\cos\phi\dot{\lambda} \\ -\dot{h} \end{pmatrix} \tag{C.9}$$

$$\delta(\Omega_{in}^n + \Omega_{ei}^n)v^n = \begin{pmatrix} (N+h)\cos\phi\dot{\lambda}[\delta\dot{\lambda}\sin\phi + \dot{\ell}_2\cos\phi\delta\phi] + \dot{h}\delta\dot{\phi} \\ -(M+h)\dot{\phi}[\delta\dot{\lambda}\sin\phi + \dot{\ell}_2\cos\phi\delta\phi] + \dot{h}(\delta\dot{\lambda}\cos\phi - \dot{\ell}_2\sin\phi\delta\phi) \\ (M+h)\dot{\phi}\delta\dot{\phi} + (N+h)\cos\phi\dot{\lambda}[\delta\dot{\lambda}\cos\phi - \dot{\ell}_2\sin\phi\delta\phi] \end{pmatrix} \tag{C.10}$$

$$(\Omega_{in}^n + \Omega_{ei}^n)\delta v^n = \begin{pmatrix} 0 & \dot{\ell}_2\sin\phi & -\dot{\phi} \\ -\dot{\ell}_2\sin\phi & 0 & -\dot{\ell}_2\cos\phi \\ \dot{\phi} & \dot{\ell}_2\cos\phi & 0 \end{pmatrix} \begin{pmatrix} \dot{\phi}\delta h + (M+h)\delta\dot{\phi} \\ \dot{\lambda}\cos\phi\delta h + (N+h)[\cos\phi\delta\dot{\lambda} - \sin\phi\dot{\lambda}\delta\phi] \\ -\delta\dot{h} \end{pmatrix} \tag{C.11}$$

$$(\Omega_{in}^n + \Omega_{ei}^n)\delta v^n = \begin{pmatrix} \dot{\ell}_2\sin\phi[\cos\phi\dot{\lambda}\delta h + (N+h)(\cos\phi\delta\dot{\lambda} - \sin\phi\dot{\lambda}\delta\phi)] + \dot{\phi}\delta\dot{h} \\ -\dot{\ell}_2\sin\phi[\dot{\phi}\delta h + (M+h)\delta\dot{\phi}] + \dot{\ell}_2\cos\phi\delta\dot{h} \\ \dot{\phi}[\delta h + (M+h)\delta\dot{\phi}] + \dot{\ell}_2\cos\phi[\cos\phi\dot{\lambda}\delta h + (N+h)(\cos\phi\delta\dot{\lambda} - \sin\phi\dot{\lambda}\delta\phi)] \end{pmatrix} \tag{C.12}$$

$$\delta f^n = f^n \mathrm{x}\psi^n + C_b^n \delta f^b = \begin{pmatrix} f_2^n\psi_3^n - f_3^n\psi_2^n \\ f_3^n\psi_1^n - f_1^n\psi_3^n \\ f_1^n\psi_2^n - f_2^n\psi_1^n \end{pmatrix} + C_b^n \begin{pmatrix} \delta f_1^b \\ \delta f_2^b \\ \delta f_3^b \end{pmatrix} \tag{C.13}$$

$$\overline{\Gamma}^n \delta p^n = \begin{pmatrix} \overline{\Gamma}_{NN} & \overline{\Gamma}_{NE} & \overline{\Gamma}_{ND} \\ \overline{\Gamma}_{EN} & \overline{\Gamma}_{EE} & \overline{\Gamma}_{ED} \\ \overline{\Gamma}_{DN} & \overline{\Gamma}_{DE} & \overline{\Gamma}_{DD} \end{pmatrix} \begin{pmatrix} (M+h)\delta\phi \\ (N+h)\cos\phi\delta\lambda \\ -\delta h \end{pmatrix} \tag{C.14}$$

$$\delta g^n = \begin{pmatrix} \delta g_N^n \\ \delta g_E^n \\ \delta g_D^n \end{pmatrix} \tag{C.15}$$

The above equations (C.4-15) can be combined and substituted in the following general form of error model:

$$\frac{\mathrm{d}}{\mathrm{dt}}\varepsilon^n = \mathrm{F}^n\varepsilon^n + \mathrm{G}^n u \tag{C.16}$$

with,

$$\varepsilon^n = \begin{pmatrix} \psi_N^n & \psi_E^n & \psi_D^n & \delta\dot\phi & \delta\dot\lambda & \delta\dot{h} & \delta\phi & \delta\lambda & \delta h \end{pmatrix} \qquad (C.17)$$

The individual elements of the dynamics matrix, F^n, are listed below; $\overline{M}$ is substituted for $(M+h)\cos\phi$,

$F_{(1,1)} = 0$

$F_{(1,2)} = -\dot{\ell}_1 \sin\phi$

$F_{(1,3)} = \dot\phi$

$F_{(1,4)} = 0$

$F_{(1,5)} = \cos\phi$

$F_{(1,6)} = 0$

$F_{(1,7)} = -\dot{\ell}_1 \sin\phi$

$F_{(1,8)} = 0$

$F_{(1,9)} = 0$

$F_{(2,1)} = \dot{\ell}_1 \sin\phi$

$F_{(2,2)} = 0$

$F_{(2,3)} = \dot{\ell}_1 \cos\phi$

$F_{(2,4)} = -1$

$F_{(2,5)} = 0$

$F_{(2,6)} = 0$

$F_{(2,7)} = 0$

$F_{(2,8)} = 0$

$F_{(2,9)} = 0$

$F_{(3,1)} = -\dot\phi$

$F_{(3,2)} = -\dot{\ell}_1 \cos\phi$

$F_{(3,3)} = 0$

$F_{(3,4)} = 0$

$F_{(3,5)} = -\sin\phi$

$F_{(3,6)} = 0$

$F_{(3,7)} = -\dot{\ell}_1 \cos\phi$

$F_{(3,8)} = 0$

$F_{(3,9)} = 0$

$F_{(4,1)} = 0$

$F_{(4,2)} = -\dfrac{f_3^{\,n}}{N+h}$

$F_{(4,3)} = -\dfrac{f_2^{\,n}}{N+h}$

$F_{(4,4)} = -\dfrac{2\dot{h}}{N+h}$

$F_{(4,5)} = -\dot{\ell}_1 \sin 2\phi$

$F_{(4,6)} = -\dfrac{2\dot\phi}{N+h}$

$F_{(4,7)} = \dfrac{1}{N+h}\left[\begin{array}{l}(N+h)\dot\lambda\dot{\ell}_2 \cos 2\phi \\ +(M+h)\overline{\Gamma}_{NN}\end{array}\right]$

$F_{(4,8)} = \cos\phi\,\overline{\Gamma}_{NE}$

$F_{(4,9)} = -\dfrac{1}{N+h}\left[\ddot\phi + 0.5\dot{\ell}_2\dot\lambda\sin 2\phi + \overline{\Gamma}_{ND}\right]$

$F_{(5,1)} = \dfrac{f_3^{\,n}}{\overline{M}}$

$F_{(5,2)} = 0$

$F_{(5,3)} = -\dfrac{f_1^{\,n}}{\overline{M}}$

$F_{(5,4)} = \dfrac{\sin\phi}{\overline{M}}\left[(N+h)\dot\lambda + (M+h)\dot{\ell}_2\right]$

$F_{(5,5)} = \dfrac{1}{\overline{M}}\left[(N+M+2h)\dot\phi\sin\phi - 2\dot{h}\cos\phi\right]$

$F_{(5,6)} = -\dfrac{2\dot{\ell}_1\cos\phi}{\overline{M}}$

$F_{(5,7)} = \dfrac{1}{\overline{M}}\left[\begin{array}{l}2\dot{\ell}_1\dot{h}\sin\phi + (M+h)[\overline{\Gamma}_{EN} + \ddot\phi\dot{\ell}_2\cos\phi] \\ +(N+h)[\dot\lambda\dot\phi\cos\phi + \ddot\lambda\sin\phi]\end{array}\right]$

$F_{(5,8)} = \overline{\Gamma}_{EE}$

$F_{(5,9)} = \dot\lambda\dot{\ell}_2\cos^2\phi + \dot\phi^2 + \overline{\Gamma}_{ED}$

$F_{(6,1)} = f_2^{\,n}$

$F_{(6,2)} = f_1^{\,n}$

$F_{(6,3)} = 0$

$F_{(6,4)} = 2\dot\phi(M+h)$

$F_{(6,5)} = 2\dot{\ell}_1(N+h)\cos^2\phi$

$F_{(6,6)} = 0$

$F_{(6,7)} = -\dot\lambda\dot{\ell}_2(N+h)\sin 2\phi - \overline{\Gamma}_{DN}(M+h)$

$F_{(6,8)} = -\overline{\Gamma}_{DE}(N+h)\cos\phi$

$F_{(7,4)} = 1$

$F_{(8,5)} = 1$

$F_{(9,6)} = 1$

$$F_{(6,9)} = \ddot{\lambda}\dot{\ell}_2 \cos^2\phi + \dot{\phi}^2 + \overline{\Gamma}_{DD}$$

The last three rows of the F matrix contain only three non-zero elements. These elements are shown above.

To assess the error contribution introduced by using Gaussian mean radius approximation, the nominal values shown in Table C.1 are used to compute the components of $F^n\varepsilon^n$ with and without Gaussian mean radius approximation. The computed values are differenced and the error contribution to each component is shown in Table C.2. The results show that using Gaussian mean radius to substitute for the principal radii of curvature N and M is a reasonable approximation.

Description	Nominal value
Position (Lat., Long., Ht.)	$(40^o, 277^o, 500$ m$)$
Velocity (horizontal)	60 m/s
Mean radius	6371000 m
Position error	10 m
Velocity error	1 m/s
Orientation error	30 arcsec.
Gravity gradients	$3 * 10^{-8}$ s^{-2}
Down-down component	$0.31 * 10^{-5}$ s^{-2}

Table C.1: Nominal values to assess errors introduced by using Gaussian mean approximation.

corresponding $F^n \varepsilon^n$ components	magnitude
$\dot{\psi}_N^n$	0
$\dot{\psi}_E^n$	0
$\dot{\psi}_D^n$	0
$\delta\ddot{\phi}$	$-2.4 * 10^{-14}$ rad/s^{-2}
$\delta\ddot{\lambda}$	$2.15 * 10^{-13}$ rad/s^{-2}
$\delta\ddot{h}$	$7.8 * 10^{-7}$ m/s^{-2}
$\delta\dot{\phi}$	0
$\delta\dot{\lambda}$	0
$\delta\dot{h}$	0

Table C.2: Order of error magnitudes introduced to $F^n \varepsilon^n$ components by using Gaussian mean approximation.

APPENDIX D

COORDINATE FRAMES AND TRANSFORMATION MATRICES

D.1 Coordinate Frames

D.1.1   Local-Level (l-frame)
         Origin – Center of the sensor.
         x-axis – East direction on ellipsoid (E).
         y-axis – North direction on ellipsoid (N).
         z-axis – Upward direction along the ellipsoidal normal (U).

D.1.2   Navigation (n-frame)
         Origin – Center of the sensor.
         x-axis – North direction on ellipsoid (N).
         y-axis – East direction on ellipsoid (E).
         z-axis – Downward direction along the ellipsoidal normal (D).

D.1.3   Body (b-frame)
         Origin – Center of the sensor.
         x-axis – Forward.
         y-axis – to the Right.
         z-axis – Down.

D.1.4   Camera (c-frame)

Origin – Center of the image.
         x-axis – Forward.
         y-axis – to the Left.
         z-axis – Upward.

Figure D.1 shows a representation of the coordinate frames and the orientation parameters to transform from one coordinate frame to another.
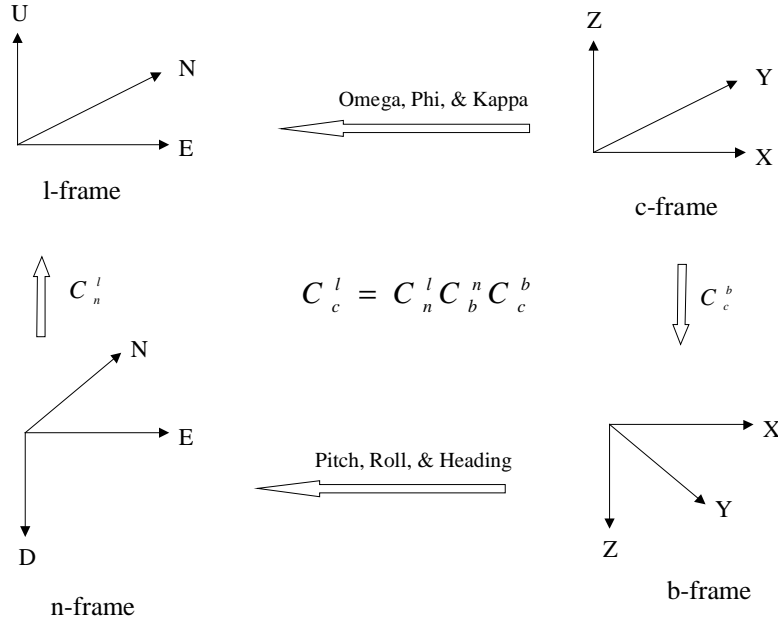
Figure D.1: Coordinate frames and orientation parameters.

$$C_l^n = \begin{pmatrix} 0 & 1 & 0 \\ 1 & 0 & 0 \\ 0 & 0 & -1 \end{pmatrix} \qquad C_b^c = \begin{pmatrix} 1 & 0 & 0 \\ 0 & -1 & 0 \\ 0 & 0 & -1 \end{pmatrix} \qquad \text{(D.1)}$$

$C_{\omega_p\kappa}$ is transformation matrix from image coordinate frame to ground coordinate frame (local-level). This matrix is given by the following:

$$C_{\omega\varphi\kappa} = C_c^l = R_1(\omega)R_2(\varphi)R_3(\kappa) \qquad \text{(D.2)}$$

where, for example, $R_1(\omega)$ is the rotation about the first axis by the angle ω.

$$C_c^l = \begin{pmatrix} \cos\varphi\cos\kappa & -\cos\varphi\sin\kappa & \sin\varphi \\ \cos\omega\sin\kappa + \sin\omega\sin\varphi\cos\kappa & \cos\omega\cos\kappa - \sin\omega\sin\varphi\sin\kappa & -\sin\omega\cos\varphi \\ \sin\omega\sin\kappa - \cos\omega\sin\varphi\sin\kappa & \sin\omega\cos\kappa + \cos\omega\sin\varphi\sin\kappa & \cos\omega\cos\varphi \end{pmatrix} \qquad \text{(D.3)}$$

$\omega : Omega$

$\varphi : Phi$

$\kappa : Kappa$

C_c^l matrix could also be computed by the following transformations:

$$C_c^l = C_n^l C_b^n C_c^b \qquad \text{(D.4)}$$

$$C_b^n = R_3(-\alpha)R_2(-\chi)R_1(-\eta) \qquad \text{(D.5)}$$

C_n^l and C_c^b give the transformation matrices between l-frame and n-frames and between b-frame and c-frame respectively. Both matrices are given in equation D.1. The transformation matrix between b-frame and n-frame is given in equation D.5, where η, χ, α are roll, pitch and yaw angles respectively. By substituting equations (D.1) and (D.5) into equation (D.4), one could reach the following:

$$C_c^l = \begin{pmatrix} \cos\chi\sin\alpha & \cos\chi\sin\alpha & \sin\chi \\ -\cos\eta\sin\alpha - \sin\eta\sin\chi\cos\alpha & \cos\eta\cos\alpha - \sin\eta\sin\chi\sin\alpha & \sin\eta\cos\chi \\ -\sin\eta\sin\alpha - \cos\eta\sin\chi\sin\alpha & -\sin\eta\cos\alpha - \cos\eta\sin\chi\sin\alpha & \cos\eta\cos\chi \end{pmatrix} \qquad \text{(D.6)}$$

$\chi : Pitch$

$\eta : Roll$

$\alpha : Yaw$

From equations (D.3) and (D.6), the relationship between the *camera Omega, Phi,* and *Kappa* and the INS *Pitch, Roll,* and *yaw* could be derived as follows:

$-\sin\omega = \sin\eta$

$\cos\omega = \cos\eta \qquad \longrightarrow \qquad \eta = -\omega$

$\sin\varphi = \sin\chi$

$\cos\phi = \cos\chi \qquad \longrightarrow \qquad \chi = \varphi$

$-\sin\kappa = \cos\alpha$

$\cos\kappa = \sin\alpha \qquad \longrightarrow \qquad \alpha = \dfrac{\pi}{2} - \kappa$

APPENDIX E

COLLINEARITY EQUATIONS AND NORMAL MATRIX

The mathematical model that relates image coordinates to object coordinates is the collinearity transformation. Geometrically, this model states that image point, perspective center, and object point must lie on a straight line. The model equations can be written as follows:

$$x = x_p - c\frac{r_{11}(X-X_0)+r_{21}(Y-Y_0)+r_{31}(Z-Z_0)}{r_{13}(X-X_0)+r_{23}(Y-Y_0)+r_{33}(Z-Z_0)}$$

$$y = y_p - c\frac{r_{12}(X-X_0)+r_{22}(Y-Y_0)+r_{32}(Z-Z_0)}{r_{13}(X-X_0)+r_{23}(Y-Y_0)+r_{33}(Z-Z_0)}$$

with all terms defined in section 2.3.3. To display the elements of the coefficient matrix and the structure of the normal matrix, the collinearity equations could be written in the following form:

$$x = x_p - c\frac{N_x}{D}$$

$$y = y_p - c\frac{N_y}{D}$$

where:

$$N_x = r_{11}(X-X_0)+r_{21}(Y-Y_0)+r_{31}(Z-Z_0)$$
$$N_y = r_{12}(X-X_0)+r_{22}(Y-Y_0)+r_{32}(Z-Z_0)$$
$$D = r_{13}(X-X_0)+r_{23}(Y-Y_0)+r_{33}(Z-Z_0)$$

With all elements defined earlier. The partial derivatives of these equations with respect to the unknown parameters (exterior orientation and tie points coordinates), are needed to build the coefficient matrix. The following equations detail these derivatives:

$$\frac{\partial x}{\partial X_0} = -\frac{c}{D^2}(r_{13}N_x - r_{11}D) \qquad \frac{\partial y}{\partial X_0} = -\frac{c}{D^2}(r_{13}N_x - r_{12}D)$$

$$\frac{\partial x}{\partial Y_0} = -\frac{c}{D^2}(r_{23}N_x - r_{21}D) \qquad \frac{\partial y}{\partial Y_0} = -\frac{c}{D^2}(r_{23}N_x - r_{22}D)$$

$$\frac{\partial x}{\partial Z_0} = -\frac{c}{D^2}(r_{33}N_x - r_{31}D) \qquad \frac{\partial y}{\partial Z_0} = -\frac{c}{D^2}(r_{33}N_x - r_{32}D)$$

$$\frac{\partial x}{\partial \omega} = -\frac{c}{D}\left[((Y-Y_0)r_{33}-(Z-Z_0)r_{23})\frac{N_x}{D}-(Y-Y_0)r_{31}+(Z-Z_0)r_{21}\right]$$

$$\frac{\partial y}{\partial \omega} = -\frac{c}{D}\left[((Y-Y_0)r_{33}-(Z-Z_0)r_{23})\frac{N_y}{D}-(Y-Y_0)r_{32}+(Z-Z_0)r_{22}\right]$$

$$\frac{\partial x}{\partial \varphi} = \frac{c}{D}\left[(N_x\cos\kappa-N_y\sin\kappa)\frac{N_x}{D}+D\cos\kappa\right]$$

$$\frac{\partial y}{\partial \varphi} = \frac{c}{D}\left[(N_x\cos\kappa-N_y\sin\kappa)\frac{N_y}{D}+D\cos\kappa\right]$$

$$\frac{\partial x}{\partial \kappa} = -\frac{c}{D}N_y \qquad\qquad \frac{\partial y}{\partial \kappa} = \frac{c}{D}N_x$$

$$\frac{\partial x}{\partial X} = -\frac{c}{D^2}(Dr_{11}-N_x r_{13}) \qquad\qquad \frac{\partial y}{\partial X} = -\frac{c}{D^2}(Dr_{12}-N_y r_{13}$$

$$\frac{\partial x}{\partial Y} = -\frac{c}{D^2}(Dr_{21}-N_x r_{23}) \qquad\qquad \frac{\partial y}{\partial Y} = -\frac{c}{D^2}(Dr_{22}-N_y r_{23})$$

$$\frac{\partial x}{\partial Z} = -\frac{c}{D^2}(Dr_{31}-N_x r_{33}) \qquad\qquad \frac{\partial y}{\partial Z} = -\frac{c}{D^2}(Dr_{32}-N_y r_{33})$$

Let $\quad N_{ij} = A_i^T P A_j, \qquad c_i = A_i^T P y$,

The normal equations can be written as follows:

$$\begin{pmatrix} N_{11} & N_{12} \\ N_{21} & N_{22} \end{pmatrix}\begin{pmatrix} \hat{\xi}_1 \\ \hat{\xi}_2 \end{pmatrix} = \begin{pmatrix} c_1 \\ c_2 \end{pmatrix}$$

Solving for $\hat{\xi}_1$ parameters only gives the following reduced normal equations:

$$(N_{11}-N_{12}N_{22}^{-1}N_{21})\hat{\xi}_1 = c_1 - N_{12}N_{22}^{-1}c_2$$

The covariance matrix of the reduced observation vector (right hand side of Equation 2.33) is derived using basic error propagation.

$$c = c_1 - N_{12}N_{22}^{-1}c_2$$
$$D\{c\} = \left[A_1^T P - N_{12}N_{22}^{-1}A_2^T P\right]D\{y\}\left[A_1^T P - N_{12}N_{22}^{-1}A_2^T P\right]^T$$
$$= \sigma_0^2\left(N_{11}-N_{12}N_{22}^{-1}N_{12}^T\right)$$

It is important to note that the matrix N_{11} is a block diagonal of size 6x6. N_{22} matrix is also block diagonal of size 3x3. This structure of N_{22} in particular makes it simple to invert the matrix by inverting the individual 3x3 submatrices. In addition, the process of homogenization could be used to decorrelate the reduced observation vector.

The singular value decomposition technique is used to decompose the above matrix as follows:

$$D\{c\} = \sigma_0^2 FDF^T = GG^T \qquad\qquad G = FD^{1/2}$$
$$D\{Gc\} = \sigma_0^2 I$$

D is diagonal matrix containing the eigenvalues of the cofactor matrix.

Once the exterior parameters are available, the coordinates of the tie points can be determined by:

$$\hat{\xi}_2 = N_{22}^{-1}c_2 - N_{22}^{-1}N_{21}\hat{\xi}_1$$

The estimated variance covariance matrix of the adjusted exterior orientation parameters is given by:

$$\hat{D}\{\hat{\xi}_1\} = \hat{\sigma}_0^2 (N_{11} - N_{12}N_{22}^{-1}N_{21})^{-1}$$
$$\hat{\sigma}_0^2 = \frac{\tilde{e}^T P \tilde{e}}{n - m}$$
$$\tilde{e} = y - A_1\hat{\xi}_1 - A_2\hat{\xi}_2$$

with *n-m* degrees of freedom.

INPUT DATA FILES DESCRIPTION

TO THE BUNDLE BLOCK ADJUSTMENT

This Appendix describes the input files to run the Bundle adjustment with self-calibration (BSC) program. All input files must be stored in a subdirectory named "data" from the working directory where the BSC program is located. Inside the input files, any line starts with the character (!) is considered as comment line. The input files are:

1. <u>Project File (*.prj):</u>

This file contains the list of input data files names and some control parameters. For example, number of iteration, tolerance to terminate the program, and antenna offsets if GPS is used and the associated covariance matrix. The list of the input data files needed for the process are the camera, orientation, image coordinates, ground control files. These files are described below.

2. <u>Camera File (*.cam):</u>

This file contains the camera type, its interior orientation parameters and their covariance matrix, number of fiducial marks (reference marks in the image frame), and number of distortion parameters if available.

3. <u>Orientation File (*.ori):</u>

This file contains the data connected with each image. For example, photo id, camera type, sigma of image measurements, degree of polynomial and its coefficients to interpolate for position and orientation for linear array scanners, orientation time, rotation angles, and perspective center coordinates. The file format is described as follows:

Photo id   Camera   Photo Type   Sigma (xy) Poly(angle)   Poly(position)
Coefficients
Coefficients.
No. of images
Current No.   Time   Orientation Angles
Perspective Center

Example:
344845   rmk15   FRAME   0.01 0.0   0   0
0
0
1
1   344845 1.47086873004628   -0.918944600927547   52.7051653772285
            672783.1582   1868848.8155   1731.93838

```
344855    rmk15    FRAME    0.01  0.0   0    0
0
0
1
1    344855  2.70838694875886       -2.15931386008048       53.5366343218396
                673382.0906            1869356.735            1733.7778
```

4. Image Coordinate File (*.icf):

This file contains the image coordinates in the photo coordinate frame, in according to the following format:

Photo id   Point id   x   y   Dispersion matrix $_{(2x2)}$
Example:

```
344845    27    -16.86653    37.2201     1.0  0.0  0.0  1.0
344845    28     17.34005    62.96911    1.0  0.0  0.0  1.0
344845    29     51.10301    88.39205    1.0  0.0  0.0  1.0
344845    51    -17.21      -33.6052     1.0  0.0  0.0  1.0
```

5. Ground Control File (*.gcf):

This file contains the data about ground control points, tie points, and their covariance matrix. The ground control points could be differentiated by their small variances (cm level of accuracy) relative to the tie points variances (10 m level of accuracy). The following format must be followed:

Point id   X   Y   Z   Dispersion matrix $_{(3x3)}$.
Example:

```
27       672350         1.869e+006      -33.0
1.0e+01          0.0             0.0
0.0              1.0e+01                 0.0
0.0              0.0             1.0e+01
28             672350         1.8695e+006      -31.50
1.0e+01          0.0             0.0
0.0              1.0e+01                 0.0
0.0      0.0   1.0e+01
29       672350         1.87e+006       -30.0
1.0e+01          0.0             0.0
0.0              1.0e+01         0.0
0.0              0.0             1.0e+01
51       673000         1.8685e+006     -33.0
1.0e-02          0.0             0.0
0.0              1.0e-02                 0.0
0.0              0.0             1.0e-02
```

APPENDIX G

MORE TEST RESULTS

This Appendix shows the results of the *Diagonal variance* and *Full variance-covariance matrix* cases for the 25-photographs simulation (see Chapter 5.3.1).
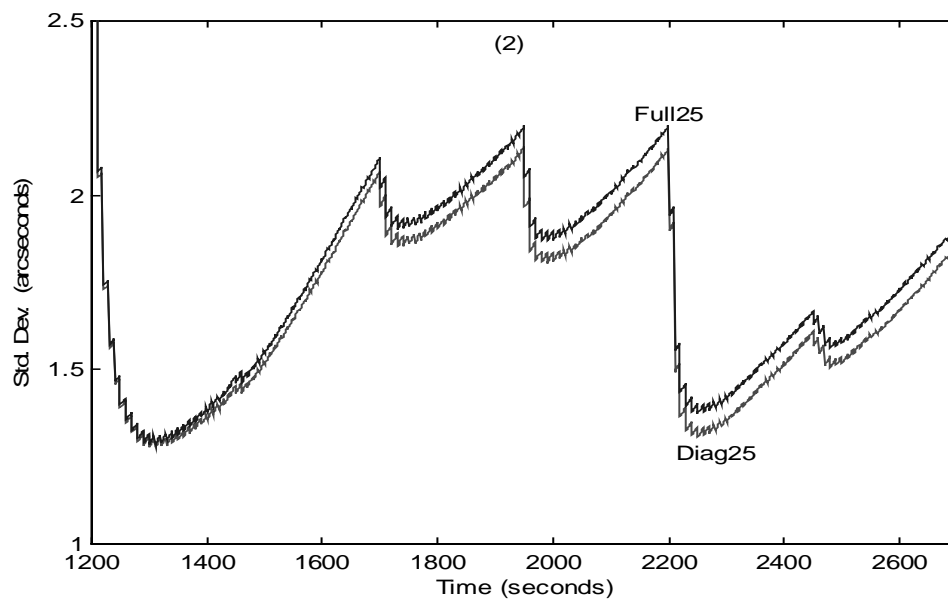

Figure G.1: Standard deviation of the E/W orientation error (arcseconds) from Diag25 and Full25 cases.
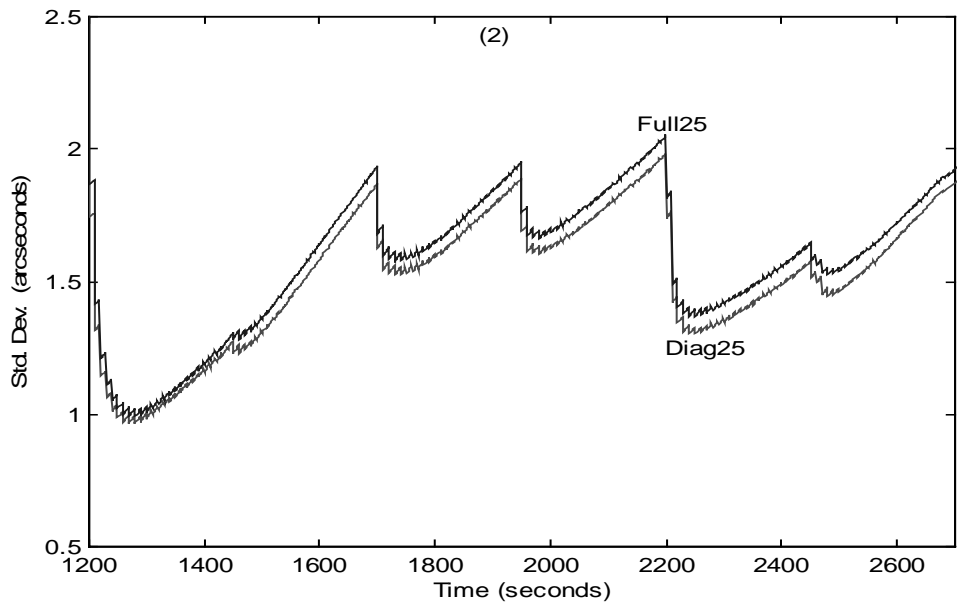
Figure G.2: Standard deviation of the N/S orientation error (arcseconds)
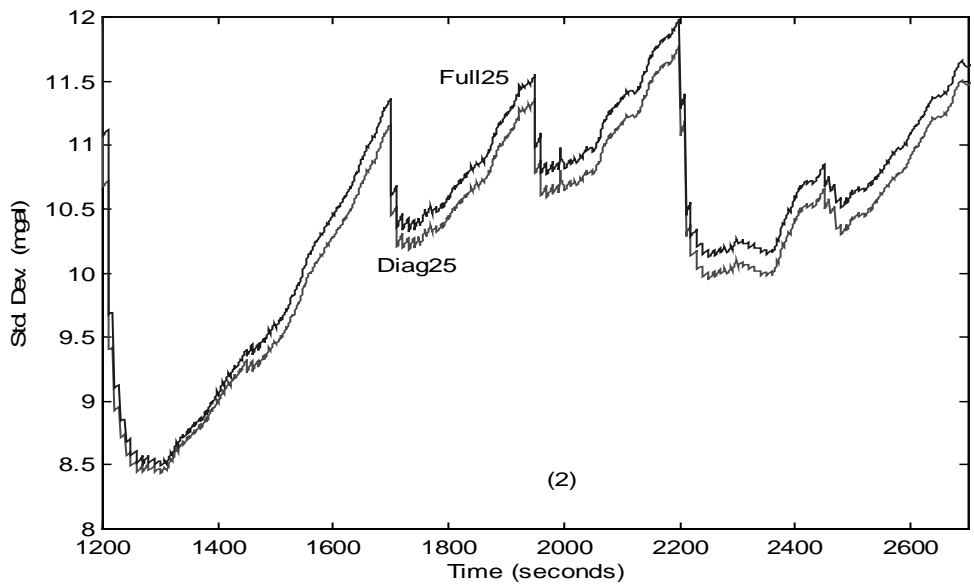from Diag25 and Full25 cases.

Figure G.3: Standard deviation of the N-S component of gravity (mgal) from
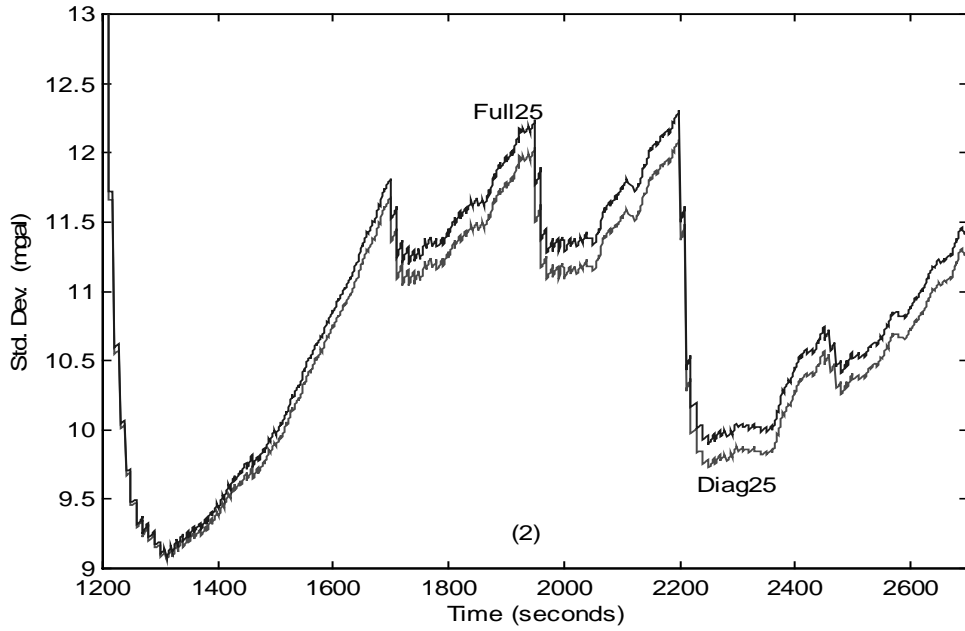Diag25 and Full25 cases.

Figure G.4: Standard deviation of the E-W component of gravity (mgal) from Diag25 and Full25 cases.

BIBLIOGRAPHY

Ackremann, F., (1992): *Kinematic GPS Control for Photogrammetry*, Photogrammetric record 14(80): 261-276.

Arshal, G., (1987): *Error Equations of Inertial Navigation*, Journal of Guidance, control, and Dynamics, Vol. 10, No. 4, PP 351-358.

Ashby, N. (1987): *Relativistic Effects in the GPS*, Proceedings of the International Association of Geodesy (IAG) Symposia of the XIX General Assembly of IUGG, Vancouver, Canada, August 10-22, Vol. 1:41-50.

Bar-Itzhack, I.Y., and Berman, N., (1988): *Control Theoretic Approach to Inertial Navigation Systems*, Journal of Guidance, control, and Dynamics, Vol. 11, No. 3, PP 237-245.

Bletzacker, FR.(1985): *Reduction of Multipath Contamination in a Geodetic GPS Receiver*, Proceedings of the 1st International Symposium on Precise Positioning with the GPS, Rockville, Maryland.

Bossler, J., (1996): *Airborne Integrated Mapping System*, Geomatics Info Magazine, Vol. 10, No. 7, pp. 32-35.

Britting, K.R.(1971): *Inertial Navigation System Analysis*, Wiley-Interscience, New York, USA.

Brozena, J.M., and Peters, M.F., (1988): *An Airborne Gravity Study of Eastern North Carolina*, Geophysics, Vol., 53, No. 2, pp. 245-253.

Brozena, J.M., and Peters, M.F., (1989): *Interferometric Global Positioning System: Three-Dimensional Positioning Source for Airborne Gravimetry*, J. Geophys Res., Vol., 97, No. B6, pp. 12153-12162.

Brozena, J.M., and Peters, M.F., (1994): *State-of-the-Art Airborne Gravimetry*, IAG Symposium No. 113, Springer-Verlag, pp. 187-197.

Bowen, R., et al (1986): *GPS Control System Accuracies*, GPS Papers, Vol. III, Institute of Navigation, Washington, D.C., pp. 241-247.

Brunner, F.K., and W.M., Welsch (1993): Effect of Troposphere on GPS Measurements, GPS World, January, 1993.

Cannon, M.E., (1987): *Kinematic Positioning Using GPS Pseudorange and Carrier Phase Observations*, Report No. 20019, Department of Surveying Engineering, The University of Calgary.

Cox, D.B., (1980): *Integration of GPS with Inertial Navigation Systems*, Papers published by The Institute of Navigation, P.M. Janiczek (ed), Vol. 1, pp. 144-153 Washington, D.C.

Cramer, M., (1995): *An Accuracy Investigation of Airborne Kinematic Attitude Determination with GPS for Sensor Orientation,* High Precision Navigation, Linkwitz, K. and Hangleiter (eds), Proceedings of the 3rd International Workshop on High Precision Navigation, University of Stuttgart, Dummler, Bonn, pp. 117-125.

Cramer, M., H. Schade (1995): *Orientation of Photogrammetric Sensors with an Integrated Multi-Antenna GPS/Low Cost INS System*, ASPRS, Barcelona.

Czompo, J., (1994): *Airborne Scalar Gravimetry System Errors in the Spectral Domain*, Dissertation, Department of Geomatics Engineering, University of Calgary, Alberta, Canada.

Da, R., (1997): *Analysis and Test Results of AIMS GPS/INS System*, Proceedings of ION-97, Kansas City, Missouri, September 16-19.

DMA Technical Report (1987): *Supplement to Department of Defense World Geodetic System 1984 Technical Report,* The Defense Mapping Agency DMA TR 8350.2-A, USA.

Eissfeller, B., (1996): *Upward Continuation of Markov Type Anomalous Gravity Potential Models,* Journal of Geodesy (70), pp.539-545, Springer-Verlag.

Eissfeller, B., (1989): *Analysis of a Geodetical Space-Stabilized Inertial Platform and Integration with GPS,* Report No. 37, Studies in Metrology, University of the Bundeswehr, Munich, Germany.

Eissfeller, B., Spietz, P., (1989): *Shaping Filter Design for the Anomalous Gravity field by Means of Spectral Factorization,* manuscripta geodaetica (14): 183-192, Springer-Verlag.

El-Mowafy, A., (1994): *Kinematic Attitude Determination From GPS, Dissertation*, Department of Geomatics Engineering, The University of Calgary.

El-Mowafy, A., Schwarz, K.P.(1994): *Epoch-by-Epoch Attitude Determination Using a GPS Multi-antenna System in Kinematic Mode*, Proceedings of the International

Symposium on Kinematic Systems in Geodesy, Geomatics, and Navigation, KIS94, pp. 331-340, Banff, Canada.

El-Mowafy, A., Schwarz, K.P.(1995): *Epoch-by-Epoch Ambiguity Resolution for Real-Time Attitude Determination Using a GPS Multi-antenna System*, Navigation: Journal of the institute of navigation, Vol.42, No.2, USA.

Forsberg, R., (1986): *A New Covariance Model for Inertial Gravimetry and Gradiometry*, Journal of Geophysical Research, Vol. 92, No. B2, pp. 1305-1310.

Gleason, D.M. (1992): *Extracting Gravity Vector from the Integration of Global Positioning system and Inertial Navigation System Data*, J. Geophys Res. 97(B6):8853-8864.

Goad C., L. Goodmann (1974): *A Modified Hopfield Tropospheric Refraction Correction Model*, paper presented at the AGU, Annual Fall meeting, San Francisco, California, December 12-17.

Greenspan R.L., (1994): *GPS and Inertial Integration*, in GPS, Theory and Application, Parkinson, Spilker, Axelrad, and Enge (eds.), pp 187-219

Grejner-Brzezinska D., (1998): *Personal Communications*, Center for Mapping, Ohio State University.

Grejner-Brzezinska D., and J. Wang (1998): *Gravity Modeling for High-Accuracy GPS/INS Integration*, Proceedings of ION-98, Denver, Colorado, June 1-3.

Groten, E., W. Hausch, and D. Keller (1987): *Some Special Considerations on Gravity Induced Effects in Inertial Geodesy*, manuscripta geodaetica (12): 16-27, Springer-Verlag.

Goshen-Meskin, D., and I.Y. Bar-Itzhack (1992): *Unified Approach to Inertial Navigation System Error Modeling*, Journal of Guidance, control, and Dynamics, Vol. 15, No. 3, PP 648-653.

Habib A., (1998): *Personal Communications*, Civil and Environmental Engineering and Geodetic Science, Ohio State University.

Hagstrom, T., M. Miller, D. Atkinson, and R. Davis (1997): *High Accuracy Gravity Disturbance Surveys Using an Astro-Inertial Navigation System With Differential GPS*, Proceedings of the International Symposium on Kinematic Systems in Geodesy, Geomatics, and Navigation, Banff, Canada, June 3-6.

Hammada, Y., (1996): *A Comparison of Filtering Techniques for Airborne Gravimetry*, Thesis, Department of Geomatics Engineering, University of Calgary, Alberta, Canada.

Hein, G.W., (1995): *Progress in Airborne Gravimetry: Solved, Open, and Critical Problems,* Proceedings of the IAG Symposium on Airborne Gravity Field Determination, Boulder, Colorado, July 2-14.

Hein, G.W., G. Baustert, B. Eissfeller, and H. Landau (1989): *High-Precision Kinematic GPS Differential Positioning and Integration of GPS with a Ring Lazer Strapdown Inertial System*, Journal of the Institute of Navigation, Vol. 36, No. 1, pp. 153-174.

Heiskanen, W.A. and H. Moritz (1967): *Physical Geodesy*, W.H. Freeman, San Franciso, Reprint 1979 by Institute of Physical Geodesy, Technical University, Graz, Austria.

Hofmann, B., H. Lichtenegger, and J. Collins (1992): *Global Positioning System, Theory and Practice*, Springer-Verlag Wein New York.

Huddle, J.R., (1978): *Theory and Performance for Position and Gravity Survey with an Inertial system*, Journal of Guidance and Control, Vol. 1, No. 3, pp. 183-188.

Huddle, J.R., (1988): *The Rapid Geodetic Survey System*, Proceedings Chapman Conference on Progress in the Determination of the Earth's Gravity Field, Fort Lauderdale, September 13-16.

Humphrey, I., T. Kawakami (1996): *User Friendly Bus Controller, GPS/INS Integration Software Documentation*, USAF Philips Laboratory Geophysics Directorate, Contract # F19628-91-C-0127.

Jekeli, C., (1991): *GPS/INS Gravity Measurements in Space and on a Balloo,* International Association of Geodesy Symposia 110, pp. 311-321, Vienna, Austria, Springer-Verlag, New York- Berlin-Heidelberg.

Jekeli, C., (1992): *Does a Gravimeter Sense Gravitation?,* Manuscripta Geodaetica, Springer-Verlag, No. 17, pp. 365-372.

Jekeli, C., (1994): *Airborne Vector Gravimetry Using Precise Position-Aided Inertial Measurement Units*, Bulletin Geodesique, 69:1-11.

Jekeli, C., (1995): *A Review of Using an Inertial Navigation System to Aid GPS in Accurate Positioning of an Aerial Photogrammetric Platform*, Report Prepared for the Ohio Department of Transportation, Department of Geodetic Science and Surveying, The Ohio state University, Columbus, Ohio, USA.

Jekeli, C., (1996): *An Introduction to Inertial Navigation Systems*, Lecture notes, Department of Civil and Environmental Engineering and Geodetic Science, The Ohio State University, Ohio, USA.

Jekeli, C., (1997): *The Effect of Earth's Gravity on Precise, short-Term, 3-D, Free-Inertial Navigation*, Journal of Navigation 44(3), 347-357.

Jekeli, C., and R. Garcia (1997): *GPS Phase Accelerations for Moving-Base Vector Gravimetry,* Journal of Geodesy 71(10), 630-639.

Jiang, Y.F., and Y.P. Lin (1992): *Error Estimation if INS Ground Alignment Through Observability Analysis*, IEEE Transactions on Aerospace and Electronic Systems, Vol. 28, No. 1, pp. 92-96.

Karatsinides, S.P., (1994): *Enhancing Filter Robustness in Cascaded GPS-INS Integration*, IEEE Transactions on Aerospace and Electronic Systems, Vol. 30, No. 4, pp. 1001-1008.

Kleusberg, A., P.J. Teunissen (eds) (1996): *GPS for Geodesy*, Lecture notes in Earth sciences, Vol. 60, Springer-Verlag. ISBN 3-540-60785-4

Knickmeyer, E.T., (1990): *Vector Gravimetry by Combination of Inertial and GPS Satellite measurements*, Report No. 20035, Department of Surveying Engineering, The University of Calgary.

Knickmeyer, E.T., (1991): *Sensor Mechanizations for Airborne Gravimetry*, High Precision Navigation, Linkwitz, K. and Hangleiter (eds), Proceedings of the 2nd International Workshop on High Precision Navigation, University of Stuttgart, Dummler, Bonn, pp. 521-526.

Kraus, K.(1992): *Photogrammetry*, Volume 1, Fundamentals and Standard Processes, 4th Edition, Ferd Dummler Verlag, Bonn.

Kwon J., (1998): *Personal Communications*, Civil and Environmental Engineering and Geodetic Science, Ohio State University.

Lapine, L.A., (1991): *Analytic Calibration of the Airborne Photogrammetric System Using a Priori Knowledge of the Exposure Station Obtained From Kinematic Global Positioning System Techniques*, Report No. 411, Department of geodetic science and Surveying, Ohio State University, Columbus, Ohio.

Lechner, W. and P. Lohmann (1995): *Airborne Photogrammetry Based on Integrated DGPS/INS Navigation*, High Precision Navigation, Linkwitz, K. and Hangleiter

(eds), Proceedings of the 3rd International Workshop on High Precision Navigation, University of Stuttgart, Dummler, Bonn, pp. 303-317.

Leick, A.(1990): *GPS Satellite Surveying*, John Wiley & Sons, Inc., New York.

Lerman, H., (1983): *Terrestrial Stellar-Inertial Navigation Systems*, Kuritsky, M.M. and M.S. Goldstein (ed.): Inertial Navigation, Proceedings of the IEEE, Vol. 71, No. 10, pp. 1170-1173.

Litton Systems, Inc. (1985): *Performance Accuracy(Truth Model/Error Budget0 Analysis for the LN-93 Inertial Navigation System*, Document No. 469414, Litton Guidance and Control Systems Division, Woodland Hills, California.

Litton Systems, Inc. (1990): *LN-93 Standard Ring Laser Gyro Inertial Navigation Unit, Technical Description*, Document No. 17969EX GC87-6247, Litton Guidance and Control Systems Division, Woodland Hills, California.

Litton Systems, Inc. (1994): *LN-100G EGI Description,* Litton Guidance and Control Systems Division, Woodland Hills, California.

Liu, Z., (1992): *Comparison of Statistical Methods for the Alignment of Strapdown Inertial Systems*, Proceedings of the International Symposium on Kinematic Systems in Geodesy, Geomatics, and Navigation, Banff, Canada, June 3-6.

Liu, Z., M.D. Reed, and D.R. Lapucha (1997): *GPS Gyro Integration for Airborne Attitude Reference*, Report No. 20047, Department of Geomatics Engineering, University of Calgary, Alberta, Canada.

Lu, G., E. Cannon, G. Lachapelle, P. Kielland (1993): *Attitude Determination in a Survey Launch Using Multi-Antenna GPS Technology*, Proceedings of the National Technical Meeting of the Satellite Division of the Institute of Navigation, San Francisco.

Mangold, U., (1995): *Rate Bias Inertial Navigation System Augmented by DGPS: To What Extent is Vector Gravimetry Possible?*, High Precision Navigation, Linkwitz, K. and Hangleiter (eds), Proceedings of the 3rd International Workshop on High Precision Navigation, University of Stuttgart, Dummler, Bonn, pp. 169-179.

Marple, S.L., (1987): *Digital Spectral Analysis with applications*, Prentice-Hall, Inc., Englewood Cliffs, New Jersy, USA.

Milliken, R.J., C.J. Zoller (1980): *Principle of Operation of NAVSTAR and System Characteristics,* Papers published by The Institute of Navigation, Janiczek (ed), Vol. 1, pp. 3-14 Washington, D.C.

Moffitt, F., Mikhail, E.(1980): *Photogrammetry*, 3rd Edition, Harper & Row, Publishers, Inc., New York.

Moritz, H., (1980): Advanced *Physical Geodesy*, 2nd ed., Herbert Wichmann Verlag GmbH, Karlsruhe.

Moritz, H., I. Mueller (1987): *Earth Rotation, Theory and Observation*, Ungar, New York.

Napier, M., (1988): *Data Processing for GPS/INS Integration*, High Precision Navigation, Integration of Navigation and Geodetic Methods, K. Linkwitz and U. Hangleiter (eds), Springer-Verlag, Berlin Heidelberg, New York.

National Research Council(NRC) (1995): *The Global Positioning System, A Shared National Asset*, National Academy Press, Washington, D.C.

Northrop Corporation (1985): *Direct Recovery of the Deflection of the Vertical Using a Position-Aided, Stellar-Inertial Navigation System*, Technical Proposal No. AFGL 86-3, Electronics Division, USA.

Novak, K., (1991), *Bundle with Self Calibration*, User Manual, Version 1.0, Department of Civil and Environmental Engineering and Geodetic Science, The Ohio State University, Ohio, USA.

Rauch, H.E., F. Tung, C.T. Striebel (1965): *Maximum Likelihood Estimates of Linear Dynamic Systems*, AIAA Journal, Vol. 3, No. 8, pp. 1445-1450.

Rose R.C., R.A. Nash (1972): *Direct Recovery of Deflections of the Vertical Using an Inertial Navigator*, IEEE Trans Geoscience Electronics GE-10(2):85-92.

Saab, S.S., K.T. Gunnarsson (1994): *Automatic Alignment and Calibration of an Inertial Navigation System*, IEEE Plans, pp. 845-852

Salychev, O.S., (1995): Inertial Surveying: ITC Ltd. Experience, Bauman MSTU Press, Moscow State Technical University, Moscow.

Scherrer, R.(1985): *The WM GPS Primer,* WM Satellite Survey Company, Wild, Heerburgg, Switzerland.

Schmidt, G.(1978): *Strapdown Inertial Systems-Theory and Applications, Introduction and Overview*, AGARD Lecture Series No. 95.

Schupler BR., TA Clark (1991): *How Different Antennas Affect the GPS Observable*, GPS World, 2(10): 32-36.

Schwarz, K.P., (1986): *The Error Model of Inertial Geodesy*, Mathematical and Numerical Techniques in Physical Geodesy, Lecture Notes in Earth Sciences, Vol. 7, pp. 464-504, Springer-Verlag, Berlin-Heidelberg.

Schwarz, K.P., M.E. Cannon, R.V.C. Wong (1989): *A comparison of GPS Kinematic Models for the Determination of Position and Velocity Along a Trajectory*, manuscripta geodaetica (14): 345-353, Springer-Verlag.

Schwarz, K.P., M. Wei (1994): *Aided Versus Embedded, A Comparison of Two Approaches to GPS/INS Integration*, IEEE position, Location, and Navigation Symposium, Las Vegas, Nevada, April 11-15.

Schwarz, K.P., M. Wei (1995): *Modeling INS/GPS for Attitude and Gravity Applications*, High Precision Navigation, Linkwitz, K. and Hangleiter (eds), Proceedings of the 3rd International Workshop on High Precision Navigation, University of Stuttgart, Dummler, Bonn, pp. 200-218.

Schwarz, K.P., M.A. Chapman, M.E. Cannon, P. Gong, and D. Cosandier (1995): *A Precise positioning/Attitude System in Support of Airborne Remote Sensing*, ISPRS, Commission II, WGII/1, Session 2.

Schwarz, K.P., O. Colombo, G. Hein, and E.T. Knickmeyer (1992): *Requirements for Airborne Vector Gravimetry*, Proceedings of the IAG Symposium, From Mars to Greenland: Charting Gravity with Space and Airborne Instruments, General Assembly of IVCC, Vienna, 1991, Springer-Verlag, pp. 273-283.

Seeber, G., (1993): *Satellite Geodesy, Foundations, Methods, and Applications*, Walter de Gruyter & Co., Berlin; New York.

Shi, J., and M.E. Cannon (1995): *Critical Error Effects and Analysis in Carrier Phase-Based Airborne GPS Positioning over Large Areas*, Bulletin Geodesique, Vol. 69, pp. 261-273.

Skaloud, J., D. Cosandier, K.P. Schwarz, M.A. Chapman (1994): *GPS/INS Orientation Accuracy Derived From A Medium Scale Photogrammetry Test*, Proceedings of the International Symposium on Kinematic Systems in Geodesy, Geomatics, and Navigation, KIS94, pp. 341-348, Banff, Canada.

Slama, C.C., C. Theurer, and S.W. Henriksen (eds) (1994): *Manual of Photogrammetry,* American Society of Photogrammetry, Falls Church, VA, USA.

Sohne, W., O. Heinze, and E. Groten (1994): *Integrated GPS/INS System for High Precision Navigation Applications*, IEEE position, Location, and Navigation Symposium, Las Vegas, Nevada, April 11-15.

Sun, H., (1994): *GPS/INS Integration for Airborne Applications*, Thesis, Department of Geomatics Engineering, University of Calgary, Alberta, Canada.

Teunissen, P.J.G., M.A. Salzmann (1988): *Performance Analysis of Kalman Filters*, Report No. 88.2, Faculty of Geodesy, Delft University of Technology, Delft, The Netherlands.

Trimble Navigation, Ltd. (1992): *4000SSE Geodetic System Surveyor, Operation Manual,* Trimble Navigation Limited, Sunnyvale, California.

Thyer, N.H., J.A.R. Blais and M.A. Chapman (1989*): Integration of an Inertial System with High-Altitude Photogrammetry over Rugged Terrain*, CISM Journal, Vol. 43, No. 1, pp. 9-19.

Vallot, L., S. Snyder, B. Schipper, N. Parker, and C. Spitzer (1991): *Design and Flight Test of a Differential GPS/Inertial Navigation System for Approach/Landing Guidance*, Navigation: Journal of the Institute of Navigation, Vol. 38, No. 2, pp. 321-340.

Vassiliou, A., Schwarz, K.P., (1987): *Study of the High Frequency Spectrum of the Anomalous Gravity Potential*, Journal of Geophysical Research, Vol. 92, No. B1, pp. 609-617.

Wang, J., (1998): *Stochastic Model versus Deterministic Model in INS/GPS Positioning,* ISPRS, Commission III Symposium, Columbus, Ohio.

Wang, J., F. Dwaik, and C. Jekeli (1997): *INS, GPS, Photogrammetry Integration for Vector Gravimetry,* Proceedings of the International Symposium on Kinematic Systems in Geodesy, Geomatics, and Navigation, Banff, Canada, June 6-9.

Wei, M., K.P. Schwarz (1994): *An Error Analysis of Airborne Vector Gravimetry,* Proceedings of the International Symposium on Kinematic Systems in Geodesy, Geomatics, and Navigation, Banff, Canada, August 30-September 2, pp. 509-520.

Wei, M., K.P. Schwarz (1995): *Analysis of GPS-Derived Acceleration From Airborne Tests,* Proceedings of the IAG Symposium on Airborne Gravity Field Determination, Boulder, Colorado, July 2-14.

Wei, M., K.P. Schwarz (1998): *Flight Results From a Strapdown Airborne Gravity Systems,* Journal of Geodesy, 72(6), pp. 323-332.

Wong, R.V.C., (1988): *Development of a RLG Strapdown Inertial Survey System*, Dissertation, Department of Geomatics Engineering, University of Calgary, Alberta, Canada.

Zhang, Q.J., K.P. Schwarz, and O.S. Salychev (1995): *Accuracy of Inertial Platform Stabilization by GPS Velocity*, Proceedings of the IAG Symposium on Airborne Gravity Field Determination, Boulder, Colorado, July 2-14.